ORNL/TM-2015/321

The Spallation Neutron Source Beam Commissioning and Initial Operations

July 2015

Approved for public release.
Distribution is unlimited.

OAK RIDGE NATIONAL LABORATORY
MANAGED BY UT-BATTELLE FOR THE US DEPARTMENT OF ENERGY

DOCUMENT AVAILABILITY

Reports produced after January 1, 1996, are generally available free via US Department of Energy (DOE) SciTech Connect.

Website http://www.osti.gov/scitech/

Reports produced before January 1, 1996, may be purchased by members of the public from the following source:

National Technical Information Service
5285 Port Royal Road
Springfield, VA 22161
Telephone 703-605-6000 (1-800-553-6847)
TDD 703-487-4639
Fax 703-605-6900
E-mail info@ntis.gov
Website http://www.ntis.gov/help/ordermethods.aspx

Reports are available to DOE employees, DOE contractors, Energy Technology Data Exchange representatives, and International Nuclear Information System representatives from the following source:

Office of Scientific and Technical Information
PO Box 62
Oak Ridge, TN 37831
Telephone 865-576-8401
Fax 865-576-5728
E-mail reports@osti.gov
Website http://www.osti.gov/contact.html

This report was prepared as an account of work sponsored by an agency of the United States Government. Neither the United States Government nor any agency thereof, nor any of their employees, makes any warranty, express or implied, or assumes any legal liability or responsibility for the accuracy, completeness, or usefulness of any information, apparatus, product, or process disclosed, or represents that its use would not infringe privately owned rights. Reference herein to any specific commercial product, process, or service by trade name, trademark, manufacturer, or otherwise, does not necessarily constitute or imply its endorsement, recommendation, or favoring by the United States Government or any agency thereof. The views and opinions of authors expressed herein do not necessarily state or reflect those of the United States Government or any agency thereof.

ORNL/TM-2015/321

Research Accelerator Division

Neutron Scattering Directorate

The Spallation Neutron Source Beam Commissioning and Initial Operations

S. Henderson, A. Aleksandrov, C. Allen, S. Assadi, D. Bartoski, W. Blokland, F. Casagrande, I. Campisi, C. Chu, S. Cousineau, M. Crofford, V. Danilov, C. Deibele, G. Dodson, A. Feschenko, J. Galambos, B. Han, T. Hardek, J. Holmes, N. Holtkamp, M. Howell, D. Jeon, Y. Kang, K. Kasemir, S. Kim, L. Kravchuk, C. Long, T. McManamy, T. Pelaia, C. Piller, M. Plum, J. Pogge, D. Purcell, T. Shea, A. Shishlo, C. Sibley, M. Stockli, D. Stout, E. Tanke, R. Welton, Y. Zhang, A. Zhukov

Date Published: July 2015

Prepared by
OAK RIDGE NATIONAL LABORATORY
Oak Ridge, Tennessee 37831-6283
managed by
UT-BATTELLE, LLC
for the
US DEPARTMENT OF ENERGY
under contract DE-AC05-00OR22725

CONTENTS

	Page
Foreward	**iv**
Abstract	**1**
1 Introduction	**1**
2 Front-end Commissioning and Operation	**3**
2.1 Ion Source and LEBT Performance	**3**
2.2 RFQ Performance	**3**
2.3 MEBT Performance	**6**
2.4 Chopper	**9**
3 Linac Commissioning and Operation	**12**
3.1 Warm Linac Commissioning	**12**
3.1.1 Longitudinal Setup	**12**
3.1.2 Transverse Measurements	**17**
3.2 Superconducting Linac (SCL) Commissioning	**18**
3.2.1 Superconducting Cavity and Cryomodule Performance	**18**
3.2.2 RF Setup	**25**
3.2.3 Transverse Beam Matching	**26**
4 Ring Commissioning and Operation	**27**
4.1 Lattice	**28**
4.1.1 Closed Orbit	**28**
4.1.2 Lattice Beta Functions	**28**
4.1.3 Tune	**29**
4.1.4 Transverse Coupling	**30**
4.2 Injection Systems	**33**
4.3 Stripper Foils	**34**
4.4 Extraction Systems	**35**
4.5 RF System	**38**
4.6 Collimation System	**39**
4.7 High Intensity Instability and Collective Effects	**42**
4.7.1 Coasting Beam Case	**43**
4.7.2 Chopped Case	**43**
5 Transport Lines	**46**
5.1 High Energy Beam Transport (HEBT)	**46**
5.2 Ring Target Beam Transport (RTBT)	**46**
6 Target Interface	**47**
6.1 Requirements	**47**
6.2 Beam Diagnostics	**47**
6.3 Beam on Target	**49**
6.3.1 Centering	**49**
6.3.2 Beam Size and Peak Power Density	**49**
7 SNS Complex Operations and Performance	**50**
7.1 Performance Parameters	**50**
7.2 Beam Loss and Activation	**51**
7.2.1 Warm Linac Beam Loss	**51**
7.2.2 SCL Beam Loss	**52**
7.2.3 Ring Beam Loss	**53**
7.2.4 Transport Line Beam Loss	**55**
8 Future Plans	**55**
References	**57**

FOREWARD

This manuscript was prepared during 2009- 2010, and covers the period of beam commissioning and initial power ramp-up of the Spallation Neutron Source accelerator from late 2006 through 2009. The manuscript was originally intended for publication, but was never submitted. At this point in time (2015) the material has generally been presented and published elsewhere, and is dated enough that it is no longer appropriate to submit it for journal publication. None-the-less, it serves as a useful comprehensive reference for the SNS accelerator commissioning, and as such has been formatted for an ORNL-TM. It should be emphasized that the material in this report has not been updated in this most recent formatting process. This report serves as a snapshot of the progress of the SNS accelerator commissioning and ramp-up as of 2009.

John Galambos

ABSTRACT

The Spallation Neutron Source (SNS) accelerator delivers a one mega-Watt beam to a mercury target to produce neutrons used for neutron scattering materials research. It delivers ~ 1 GeV protons in short (< 1 *m*s) pulses at 60 Hz. At an average power of ~ one mega-Watt, it is the highest-powered pulsed proton accelerator. The accelerator includes the first use of superconducting RF acceleration for a pulsed protons at this energy. The storage ring used to create the short time structure has record peak particle per pulse intensity. Beam commissioning took place in a staged manner during the construction phase of SNS. After the construction, neutron production operations began within a few months, and one mega-Watt operation was achieved within three years. The methods used to commission the beam and the experiences during initial operation are discussed.

1. INTRODUCTION

The Spallation Neutron Source (SNS) accelerator is designed to provide a 1.4 MW short-pulsed beam on a mercury target to generate neutrons for material research [1]. The accelerator includes an H^- front-end, a 186 MeV warm linac, and a 1 GeV superconducting RF linac. The ms long linac beam pulses are compressed to 1 μs in a storage ring and fast extracted to a mercury target to provide an intense short pulse neutron source at 60 Hz. Operation of a mega-Watt class short pulse accelerator represents a significant power increase over previous pulsed spallation neutron sources.

SNS was constructed as a collaborative effort, with the front-end provided by Lawrence Berkeley National Laboratory (LBNL), the warm linac provided by Los Alamos National Laboratory (LBNL), the superconducting RF linac provided by Jefferson Laboratory, and the transport lines and storage ring provided by Brookhaven National Laboratory (BNL). All the accelerator components were installed at the SNS facility in Oak Ridge Tennessee, and beam was commissioning in a staged approach from 2002 through 2006, shown schematically in Figure 1-1. Beam commissioning activities were spread over about three and a half years during the SNS project construction.

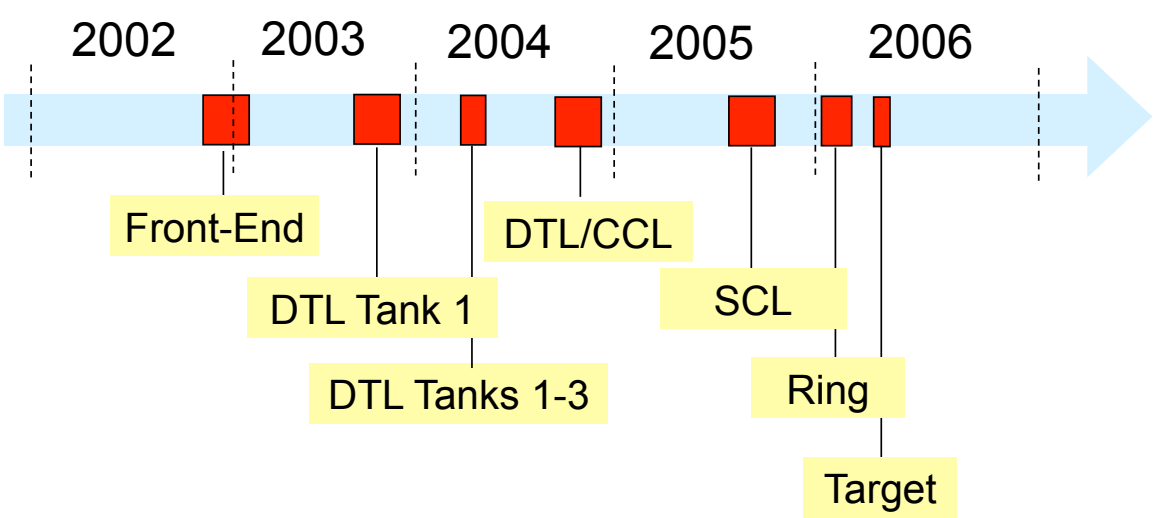

Figure 1-1. Beam commissioning timeline during the SNS construction period.

The effort to start beam commissioning as soon as possible proved useful. Early operation of the front-end at SNS provided an opportunity for integrated tests of most of the basic accelerator systems, e.g. the control system, timing, machine protection, RF, vacuum and high level software. Individual system issues as well as integration issues were identified at an early stage, allowing time for improvements before the majority of the accelerator was commissioned. A general trend in the beam commissioning time-line is that initially considerable time was spent on relatively small sections of beam line. Drawing on the early commissioning experience, large fractions of the accelerator were commissioned in relatively short periods in the latter stages. For example, the transport lines and ring commissioning were performed in 5 weeks.

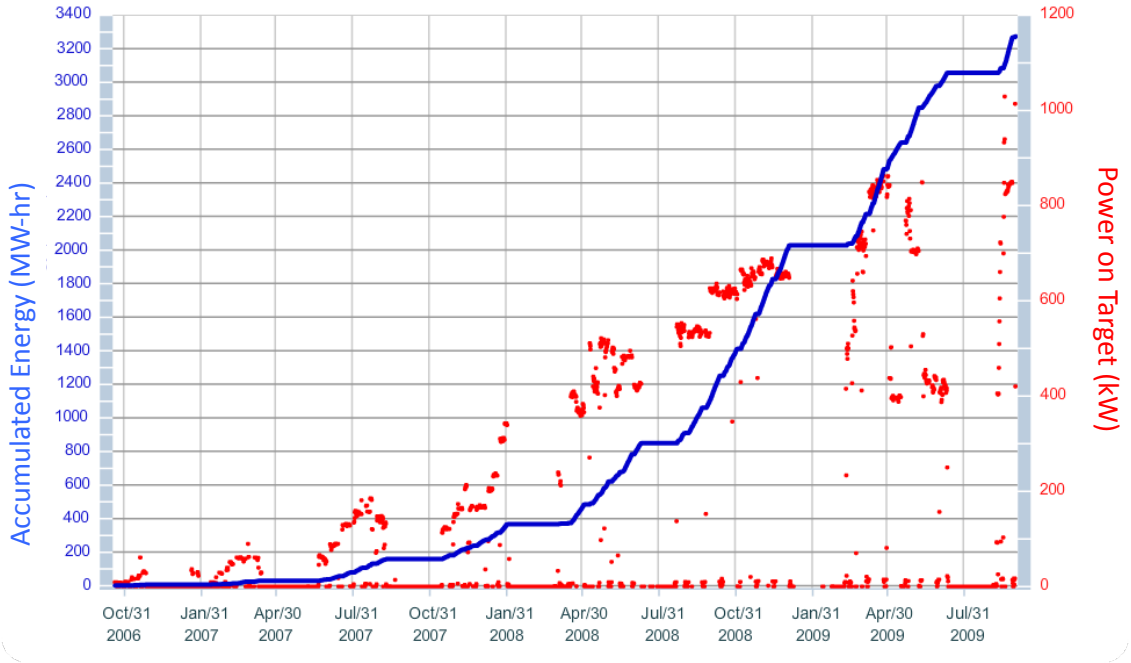

Figure 1-2. The SNS operational beam power on target and accumulated energy on target over the first three years of operation.

The first neutron production run began October 12, 2006 with the beam on target at 5 Hz, and ~4 kW. Less than three years later on Sept 18, 2009 one mega-Watt operation was achieved. The power ramp-up history is shown in Figure 1-2. The power increase from October 2006 through November 2007 was accomplished primarily through increase in the repetition rate, followed by gradual increase in the pulse length and increased beam current. The power ramp up was aggressive, and equipment shortcomings became apparent as the operational duty factor increased, as discussed below. At times, temporary reductions in beam power were needed to accommodate equipment shortcomings. Overall, the early identification of equipment weaknesses proved valuable, as understanding of the root causes and implementation of remedial actions sometimes took considerable time. In the sections below the details of the commissioning and initial power ramp up to one mega-Watt operation are discussed.

2. FRONT-END COMMISSIONING AND OPERATION

The front-end for the SNS accelerator systems is a 2.5 MeV injector consisting of the following major subsystems: an RF driven H^- source, an electrostatic low energy beam transport line (LEBT), a 402.5 MHz RFQ, a medium energy beam transport line (MEBT), a beam chopper system and a suite of diagnostic devices. The front-end is required to produce a 2.5 MeV beam of 38mA peak current at 6% duty factor. The 1 ms long H^- macro-pulses are chopped at the revolution frequency of the accumulator ring (~1 MHz) into mini-pulses of 645 ns duration with 300 ns gaps. The SNS front-end was initially built at LBNL and commissioned with beam in May of 2002 [2,3]. Subsequently it was shipped to the SNS at Oak Ridge and re-commissioned in November-December 2002 [4].

2.1 ION SOURCE AND LEBT PERFORMANCE

Details of the ion source and LEBT design can be found in [5]. The ion source is a multi-cusp, RF-driven, Cs-enhanced, H^- ion source which, for commissioning, delivered pulses typically ~85 ms in length at repetition rates of ~10Hz. Beam was extracted from the ion source and matched to the RFQ accelerator using a 12cm, electrostatic LEBT featuring 2-lenses electrically isolated by Al_2O_3 stand offs. During commissioning periods, a newly refurbished source would typically initially produce 40-50 mA peak beam currents but generally decayed to 10-25 mA after several hours of operation, which was sufficient for most commissioning tasks. Initially the source and LEBT availability was limited to ~85%. Major problem areas included outgassing of ceramic-metal glue joints supporting the LEBT electrodes in the vacuum system and issues related to the RF amplifier and matching network.

The glued LEBT joints were replaced with brazed and mechanically fastened connections and improvements to the RF systems were implemented. Failures to the porcelain-coated internal antennas were problematic especially as the source was operated with higher duty-factors for neutron production runs. These problems are being addressed with R&D efforts and significant improvements were recently made [6]. The beam persistence issues regarding maintaining beam currents of 30-40 mA over run periods of weeks for higher duty factor beam operation have largely been solved with improved cesiation procedures and fine-tuning the ionization surface geometry [7]. These improvements have significantly improved the source availability.

Another major problem during initial operations was electrical breakdowns in the electrostatic LEBT. The arcs damage fast MOSFET switches of the chopper high voltage power supply. This problem caused significant beam downtime and operational difficulties during early operation. In addition to the LEBT improvements discussed above, protective circuitry was introduced in the chopper electronics at the expense of slowing the rise/fall times, and operational procedures to disconnect the chopper when an excessive spark rate is observed were implemented. As a long-term solution we plan to use a magnetic LEBT, which is in the early stages of development [8].

2.2 RFQ PERFORMANCE

The design of the 3.72 m-long 4-vane RFQ with π-mode stabilizers is described in reference [9]. It operates at 402.5 MHz and accelerates the H^- beam from 65 kV to 2.5 MeV. There are no beam current diagnostics in the LEBT due to its very compact design thus it is not possible to measure the beam current

injected into the RFQ. As a result the absolute transmission through the RFQ is unknown. To calibrate the amplitude of the RF field and set it to the nominal value we fit PARMTEQ [10] simulations to the measured dependence of the output beam current vs. the RF field amplitude [3,4]. A typical result of such fit is shown in Figure 2-1.

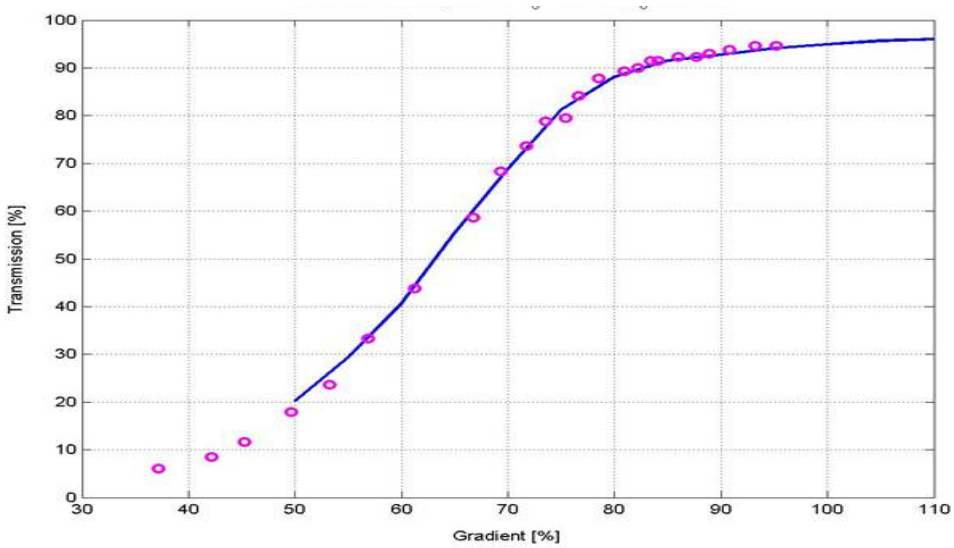

Figure 2-1. RFQ transmission vs. RF power. Measurements (red) and model fit (blue). The 100% gradient corresponds to 690 kW, and full current is 23.6 mA.

The RFQ output energy was measured by a time-of-flight technique in the MEBT and found to be 2.45±0.01 MeV, compared with the 2.5 MeV nominal design energy. There is no direct way to correct the beam energy in the RFQ itself but it can be corrected in the MEBT by offsetting rebuncher phases slightly.

The Twiss parameters of the RFQ output beam were measured using a slit/harp type emittance device temporary installed at the RFQ exit during commissioning [3]. As shown in Table 2-1, there was a good agreement between measured and predicted values. After commissioning the emittance device was removed and subsequently wire scanners were used in the MEBT to obtain Twiss parameters indirectly by fitting beam simulations with varying input parameters to best match measured beam RMS sizes at several locations (see Figure 2-2). There is good agreement with the design values in the horizontal plane but the vertical beta-function is smaller than expected by about a factor of 2. The wire scans and the model fit was done for a set of different quadrupole settings in the MEBT, producing a set of the input Twiss parameters, shown in Figure 2-2b by squares. There is a spread of calculated values due to the measurement errors and model imperfections but the observed discrepancy in the vertical plane (blue circle) is significantly larger than the spread and the possible cause is still unknown.

Table 2-1. Twiss parameters measured at the RFQ output

Peak current [mA]	Emittance [π– mm-mrad]	α	β [m]	Remark
22	.27	-13	6.5	Horizontal, measured
32	.28	-13	6.4	Horizontal, measured
20	.30	-11	5.3	Horizontal, simulated
22	.29	-6.9	2.6	Vertical, measured
30	.30	-6.0	2.3	Vertical, measured
20	.25	-8.2	3.2	Vertical, simulated

a)

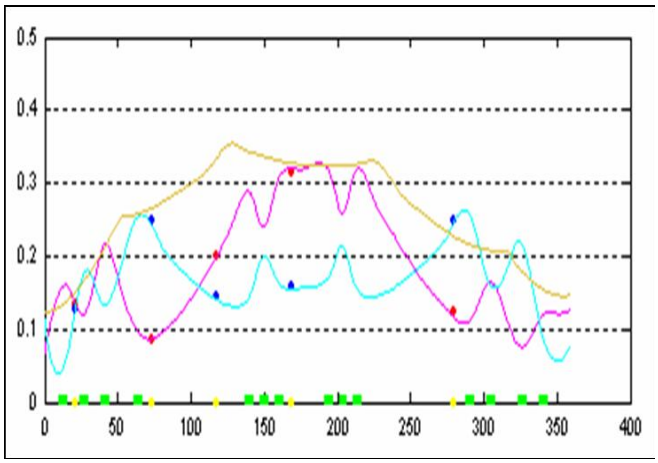

b)

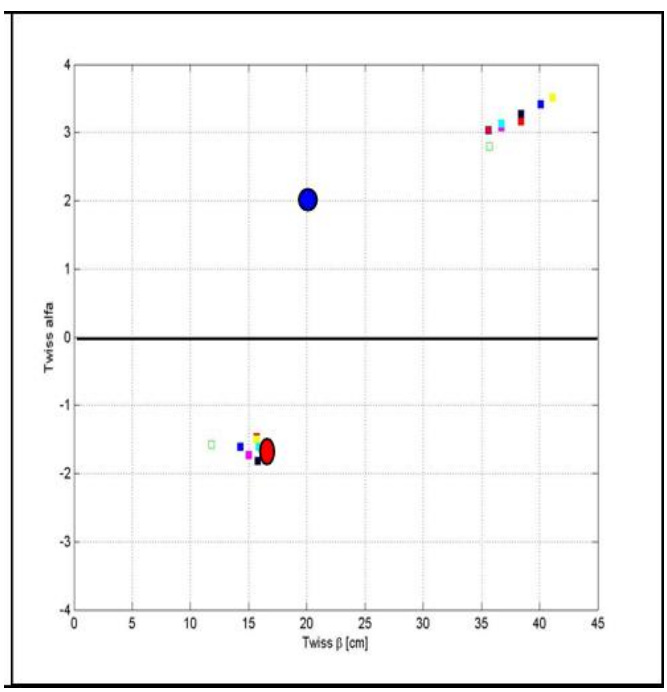

Figure 2-2. a) RMS Beam size(cm) vs. distance in the MEBT (cm). The points show measured horizontal and vertical beam profiles and curves show the predicted horizontal (red), vertical (blue) and longitudinal (brown) profiles. b) RFQ output Twiss parameters: design (large circles) and measured (squares).

2.3 MEBT PERFORMANCE

The MEBT is a complex beam transport line [11]. It matches the beam from the RFQ through the MEBT chopper system and into the drift-tube linac. Fourteen quadrupole magnets and four bunching cavities provide transverse and longitudinal focusing.

The MEBT is equipped with a suite of non-interceptive beam diagnostics including two beam current monitors (BCMs), six beam position and phase monitors (BPMs) and an experimental longitudinal profile measurement system utilizing a mode-locked laser. Interceptive beam diagnostics include five dual- plane wire scanners (WSs), and a dual plane emittance device of slit/harp type. A set of two horizontal scrapers was temporarily installed in the middle of the MEBT for halo mitigation study during commissioning.

The beam pulse length is limited to 50μs when using the interceptive diagnostics. During commissioning all beam measurements were taken at the start of the pulse. Variation of beam parameters along the pulse due to transient processes in the source plasma, are not observable with the existing interceptive diagnostics. All data from the interceptive devices, reported in this paper, are for short time slices and may not accurately represent the effective size or emittance of the entire pulse.

The beam trajectory can be easily corrected to less than 1 mm offset in the BPMs using 6 vertical and 6 horizontal steerers in the MEBT. Quadrupole strengths are set to design values and do not require additional adjustments. Comparison of the design beam size with the wire scanner measurements in Figure 2-2a shows good agreement when the MEBT input Twiss parameters in the model are adjusted to best fit the measurements. After proper tuning beam losses in the MEBT are below the measurement accuracy of the BCMs as illustrated by Figure 2-3. In this picture the beam current pulse at the MEBT exit (BCM11) is shown on top of the beam pulse at the MEBT entrance (BCM02).

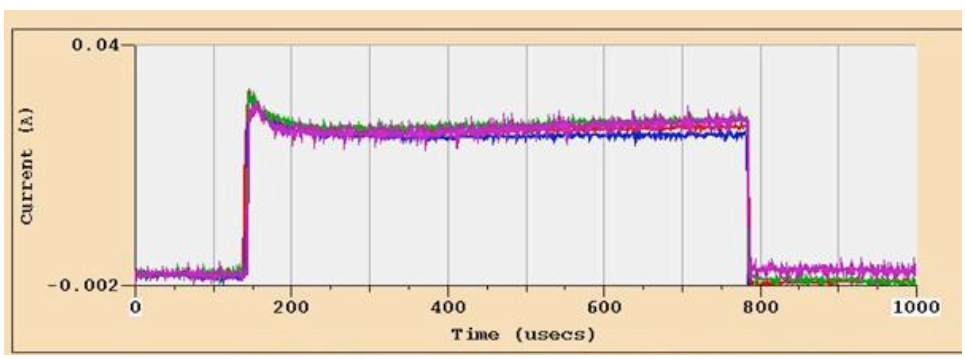

Figure 2-3. Beam pulse waveforms through the MEBT and DTL1. Red = start of MEBT, blue = end of MEBT, green = end of DTL1 and Purple = dump after end of DTL1.

To find correct RF phase set points for the rebuncher cavities the RF phase of the cavity is scanned for several RF field levels and the downstream beam phase response is recorded. The BPM phase (beam arrival time) response curves corresponding to the different field levels intersect at the bunching phase. Slope of those lines, linearly proportional to the voltage across the cavity gap, are used for the amplitude calibration. A typical scan result is shown in Figure 2-4.

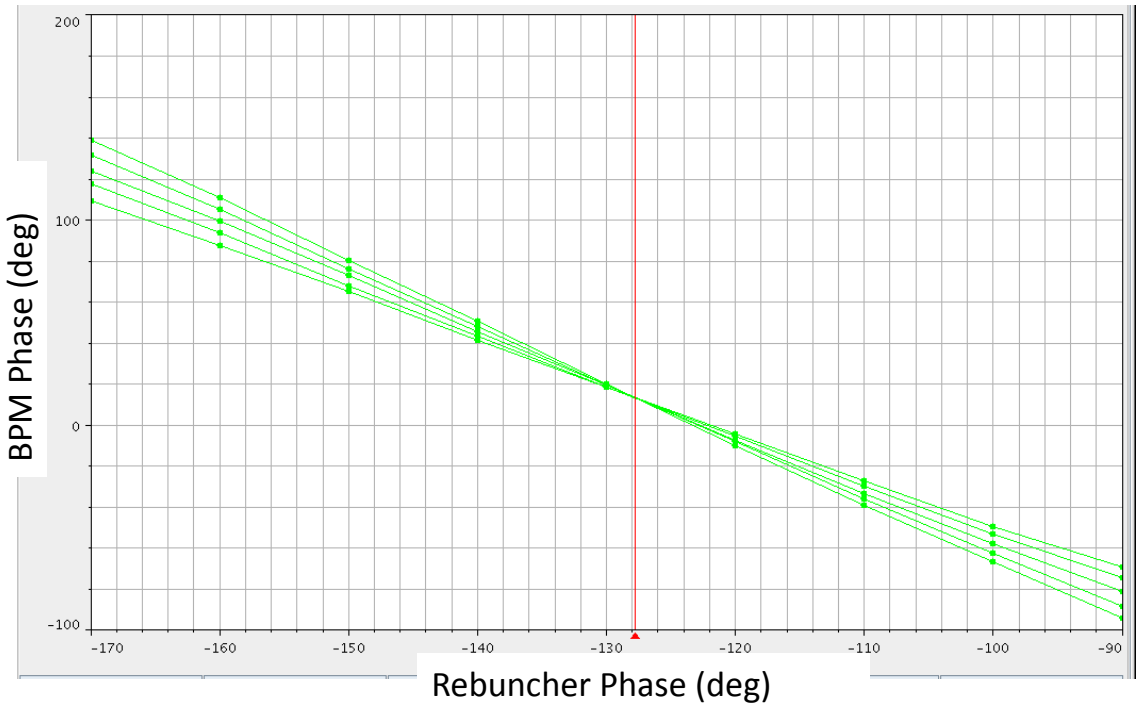

Figure 2-4. Downstream BPM (phase) response vs. bunching cavity phase for various cavity amplitude settings. Bunching occurs at the indicated intersection.

The transverse phase space measured 2/3 of the way through MEBT length is shown in Figure 2-5. The emittance values are within the design requirements. The effect of scraping can be clearly seen in Figure 2-5. The left picture shows significant halo, which is removed by a pair of scrapers at a single location. This measurement confirms the correct choice of the scraper location [12]. A set of water-cooled scrapers, suitable for use with production beam power, was subsequently implemented.

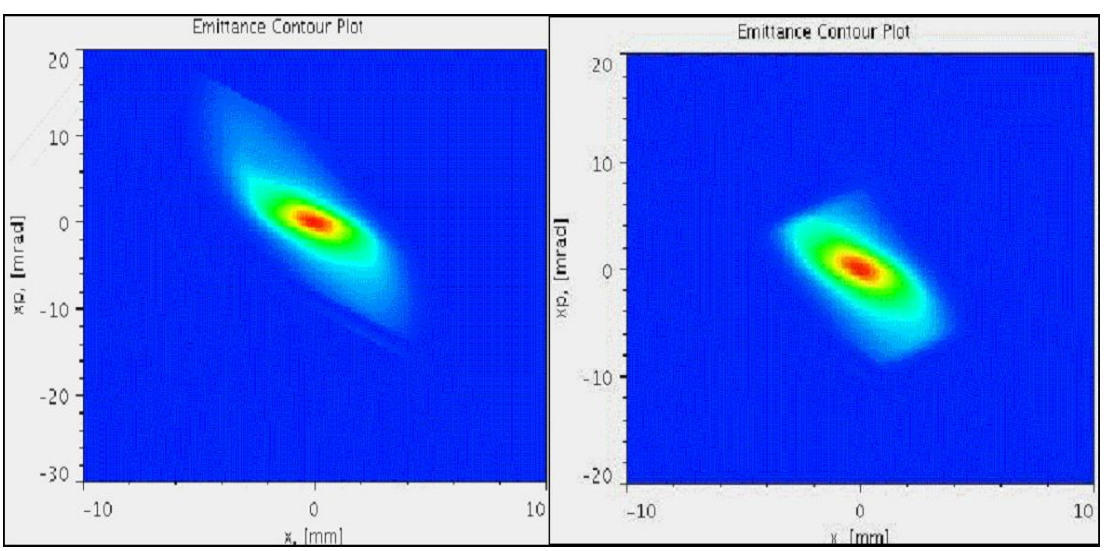

Figure 2-5. Beam horizontal phase space in the MEBT with scraper out (left) and in (right).

The horizontal emittance scan in Figure 2-5 clearly shows an S-shaped distortion caused by non-linear space charge forces, which can be affected by scraping in the MEBT. Even in the presence of the emittance growth due to non-linearity, the rms emittance satisfies the design requirement over a wide range of beam currents as illustrated in Figure 2-6, where the output rms emittance is plotted vs. beam current. Measurements shown in blue were taken after optimization of the beam optics to minimize emittance for the particular beam current; measurements shown in red were obtained by simply increasing beam current without adjusting the optics accordingly.

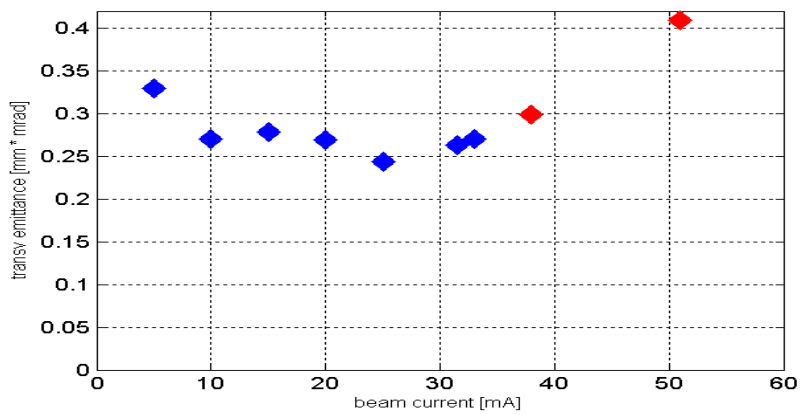

Figure 2-6 Transverse normalized rms emittance at the MEBT exit vs. peak beam current.

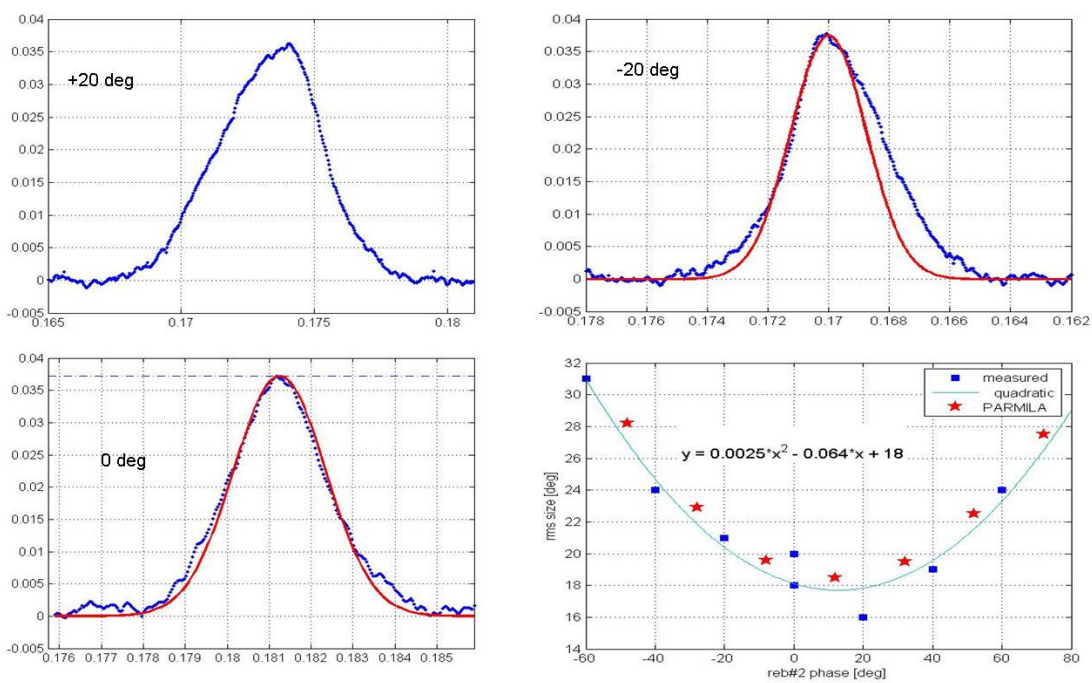

Figure 2-7. Longitudinal bunch profile measured with mode-locked laser in the MEBT (blue dots) and Gaussian fit (red line) at various MEBT RF phase settings. Bottom right: rms bunch length vs. the rebuncher phase (measurements – squares, simulation – stars, solid line – quadratic fit).

The longitudinal bunch profiles measured with a mode-locked laser system are shown in Figure 2-7. The bunch has a symmetric Gaussian-like profile when the upstream rebuncher phase is set correctly (bottom left). When the rebuncher phase is not set to 90 degrees, a head to tail asymmetry appears (top left and right) in good agreement with the simulation. The rms bunch length vs. the rebuncher phase is shown at bottom right. The measured values (squares) are in good agreement with PARMILA [13] prediction (stars). This measurement confirms that longitudinal bunch parameters are close to the design.

2.4 CHOPPER SYSTEMS

The 1-ms long H^- macro-pulses have to be chopped at the revolution frequency of the accumulator ring into mini-pulses of 645 ns duration and 300 ns gaps. Beam chopping is performed by two separate chopper systems located in the LEBT and MEBT. The last lens in the LEBT is split into four quadrants to allow electrostatic chopping using the RFQ entrance flange as a chopper target. The LEBT chopper removes most of the beam charge during the mini-pulse gaps, and the traveling-wave MEBT chopper further cleans the gap to a level of 10^{-4} and reduces the rise and fall time of the mini-pulse to 10 ns. A chopper controller provides different patterns of chopped beam: “regular chopping”, “single mini-pulse”, “every n-th mini-pulse”, “blanking-off”, and current ramp up.

Chopped patterns produced by the LEBT and MEBT choppers in the beam are observed by measuring the envelope of the 805MHz harmonics induced by the beam in the MEBT BPMs through a system called Chopper Machine Protection System (ChoMPS) [14]. This system uses the signal from the first BPM in the MEBT (upstream of the MEBT chopper) for MEBT chopper target protection by shutting off the beam if excessive current in the gap appears due to the LEBT chopper failure. The signal from the last BPM in the MEBT (downstream of the MEBT chopper) is used for synchronizing the MEBT chopper timing relative to the LEBT chopper and for observing the effectiveness of the MEBT chopper on the beam. The ChoMPS system resolution allows measuring the on/off ratio to a level of about 10^{-3}.

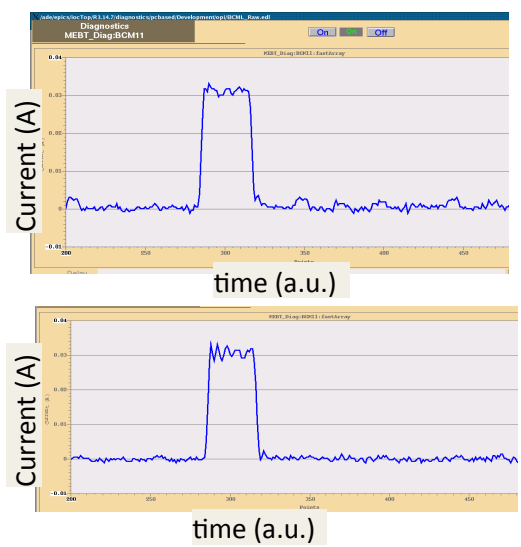

Figure 2-8. Single 650 ns mini-pulse. Top: produced by the LEBT chopper alone, some leakage current is observed before and after the pulse. Bottom: MEBT chopper is also on, and the leakage current is suppressed.

The chopper systems demonstrated design parameters during commissioning at low average beam power. Figure 2-8 shows an example of a single 650 ns mini-pulse produced by the LEBT chopper alone (top plot) and by both the LEBT and MEBT choppers together (bottom plot), demonstrating shortening of

the beam rise time and cleaning of the leakage current outside of the mini-pulse. The high-resolution measurement of the raw signal from the BPM shown in Figure 2-9 demonstrates the design rise time for the LEBT chopper (top) and the MEBT chopper (bottom).

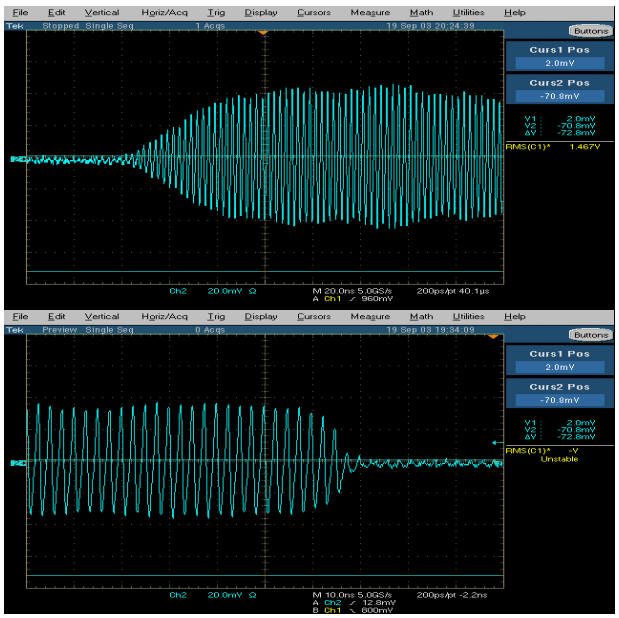

Figure 2-9. Fast measurements of the LEBT chopper rise time (upper trace) and MEBT chopper fall time (lower trace) measured at the MEBT exit. The structure in the images is the 402.5 MHz beam bunching.

When the average beam power increased we discovered problems with both the LEBT and the MEBT choppers. First the LEBT chopper high voltage switches failed quite often, due to electrical breakdown in the electrostatic LEBT, to the point where the LEBT chopper operation became impossible. Various improvements have been implemented to mitigate the formation and effect of electrical discharge in the LEBT including installing protective resistors between the power supplies and the chopper electrodes. As a result the LEBT chopper rise time increased from less than 40ns to more than 100ns as shown in Figure 2-10. The slow chopper rise time results in effective transverse beam size increase, as illustrated in Figure 2-11, which can lead to increase beam loss throughout the accelerator.

The increase in partially deflected beam should have been mitigated by use of the MEBT chopper, but the MEBT chopper kicker failed in the same period. Upon disassembly the structure had damage apparently caused by overheating of the copper meander lines concentrated along the beam path, indicating uncontrolled beam loss was the main source of the heat. The spare deflecting structure failed in a similar fashion so the meander-line structure was replaced with a simpler but more robust solid copper strip-line structure of the same length and aperture. The new MEBT chopper structure has been developed, manufactured and successfully commissioned with beam. The MEBT chopping typically has minimal effect on reducing beam loss in the linac in our present mode of operation, but does reduce extraction losses in the Ring at times. The MEBT chopper evolution is described in Ref. [15].

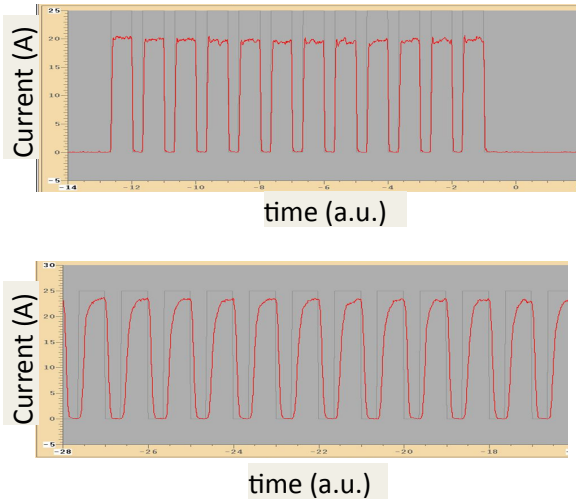

Figure 2-10. Chopped beam pattern produced by the LEBT chopper without the protection circuitry (top, rise/fall time is ~50 ns) and with the protection circuitry (bottom, rise/fall time is ~150 ns).

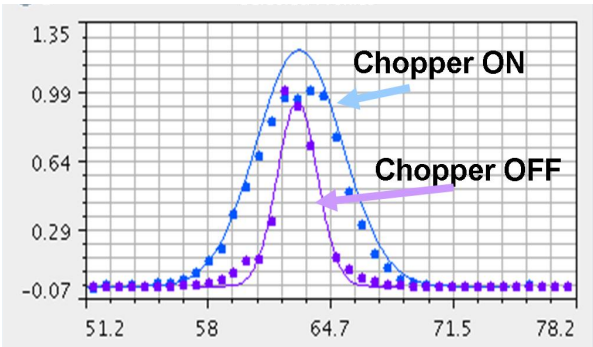

Figure 2-11. Transverse profile measurement indicating the effect of slow chopping on the beam size.

3. LINAC COMMISSIONING AND OPERATION

3.1 WARM LINAC COMMISSIONING

The Drift Tube Linac consists of six accelerating tanks operating at 402.5 MHz with an output energy of 87 MeV. The transverse focusing is arranged in a FFODDO lattice utilizing permanent-magnet quadrupoles. Some of the empty drift tubes contain Beam Position Monitors (BPMs) and dipole correctors. The linac BPMs provide both beam position and bunch arrival time. The inter-tank sections contain Beam Current Monitors (BCMs), wire scanners and energy degrader/faraday cup diagnostics. The DTL structures were commissioned in stages: tank 1 in September – November of 2003, tanks 1-3 in April 2004, and tanks 4-6 in September – December 2004 [16,17]. The Coupled Cavity Linac (CCL) consists of four 12-segment accelerating modules operating at 805 MHz with output energy of 186 MeV. The inter-segment sections contain electromagnet quadrupoles arranged in a FODO focusing lattice, BPMs, wire scanners, and longitudinal Beam Shape Monitors (BSMs). Longitudinal tuning of the linac is routinely done using "phase-scan signature matching" algorithm described below. The first 3 CCL modules were commissioned in September – December 2004, along with the last 3 DTL tanks. The final CCL module was commissioned at the start of the SCL commissioning period in August 2005 [12,18,19].

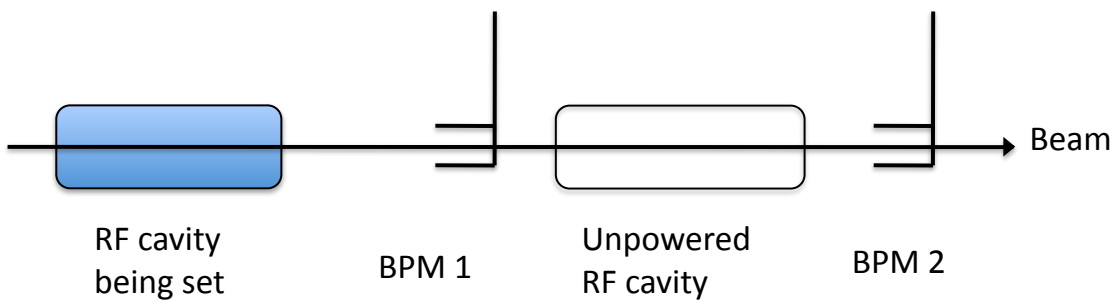

Figure 3-1. Schematic of the device layout used in beam based time of flight measurements for RF setup.

3.1.1 Longitudinal Setup

The SNS warm linac RF structures (referred to as a cavity here) each have a unique operating point for both the RF field amplitude and synchronous phase. Several techniques were used for determination of the correct RF phase and amplitude setup using beam based measurements. The primary methods are based on comparing Time-of-Flight (TOF) measurements between two downstream phase detectors and model expectations, as indicated schematically in Figure 3-1. The RF phase is scanned and the beam arrival time is monitored downstream using two Beam Position Monitors (BPMs - which also detect the bunch arrival time) over a range of cavity phases and for one or more amplitudes. A single particle longitudinal tracking model is used to predict the BPM TOF (or phase) difference for different assumptions on input beam energy, klystron field amplitudes, and klystron phase offset relative to the beam. These three parameters are varied to best match the measured TOF curves. Determining these quantities provides a means to set the RF klystron amplitude and phase, as well as providing a measurement of the input beam energy and prediction of the output beam energy.

A linearized beam response approximation implementation of this approach is referred to as the Delta-T method [20]and has been used at SNS [21].This technique works well if the initially scanned RF phase is within about 5-10 degrees of the targeted synchronous phase and the amplitude is within 10 percent of the desired setting. A more general phase scan technique is the signature matching method [22,23]. This method does not use linear approximations and is useful over a wider RF phase range. Phase scan ranges of 20-60 degrees are typical for the warm linac structures. At energies below 10 MeV, de-

bunching becomes an issue for phase settings far from the design values, and TOF pickup is problematic. An example result from this technique is shown in Figure 3-2. Each cavity has a unique phase scan signature, which is quite sensitive to the fitting parameters. Additionally as each cavity setting provides an independent energy measurement, one can also check for consistency in the predicted output energy of an upstream cavity with the measured input energy of the downstream cavity. As seen in Table 3-1, it is generally it is possible to achieve relative energy output/input errors $< 10^{-2}$ between adjacent cavities. For any TOF technique to be viable, careful attention must be given to the BPM calibration so that relative BPM TOF change measurements of ~1 degree (in units of the RF frequency) can be attained [24].

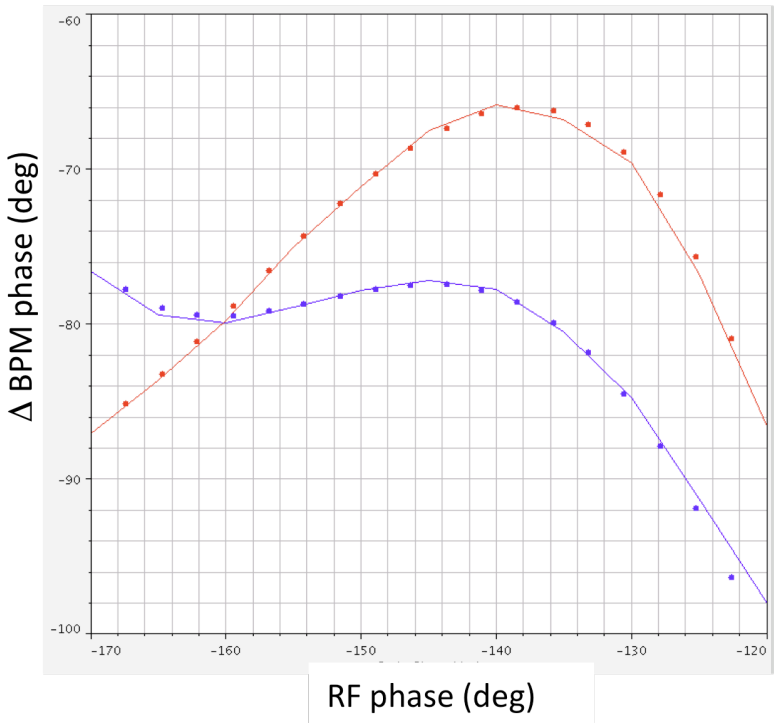

Fig. 3-2. Example phase scan signature match for DTL tank 4. The solid curves are measured downstream BPM phase differences (or TOF response) vs. RF phase for 2 different RF amplitudes (red and blue). The dots are model predictions after matching the input beam energy, cavity voltage and RF phase offset. Each warm linac structure has a unique phase difference "signature".

Table 3-1. Comparison of measured beam input energy using the phase scan application, calculated beam output energy and the design values for the warm cavities of the SNS linac, from RF phase scan signature matching

RF Cavity	Measured Input Energy (MeV)	Measured Output Energy (MeV)	Design Output Energy (MeV)
DTL1	2.48	7.51	7.52
DTL2	7.56	22.83	22.89
DTL3	22.90	39.74	39.77
DTL4	39.82	56.45	56.54
DTL5	56.78	73.30	72.52
DTL6	72.52	87.05	86.83
CCL1	86.91	107.12	107.16
CCL2	107.10	131.25	131.14
CCL3	131.07	157.20	157.21

Finally the DTL RF setup can be done with a set of energy degrader-Faraday Cups at the exit of each DTL. The energy degraders are designed to only transmit beam near the fully accelerated energy the upstream cavity. By comparing the measured charge transmitted through the energy degrader to model predicted values, throughout phase and amplitude variations one can also find the correct RF phase and amplitude settings [25,26]. The energy degrader technique tends to provide phase and amplitude settings similar to the signature matching technique, but requires more time and also insertion of intercepting hardware in the beam-line.

Longitudinal bunch profiles can be measured at four locations in the CCL using the Bunch Shape Monitors (BSM). Examples of measured longitudinal bunch profiles are shown in Figure 3-3 for the cases of the correct setting of the buncher phase in the MEBT and for the MEBT phase shifted by 180 degrees. In the second case the buncher defocused particles longitudinally filling the whole longitudinal acceptance of the linac. Equivalent Twiss parameters of the longitudinal distribution can be calculated if longitudinal beam size is measured at three locations and transport matrix between these locations is known. The nominal longitudinal emittance design value at 38 mA is 0.25 π·MeV-deg. Typically we observe measured emittance variation from 1.2 to 2.0 times the nominal value from one run to another. The exact correlation of its value with different linac parameters remains to be established.

Longitudinal bunch size measurements show good agreement with PARMILA [13] beam dynamics simulation as demonstrated in Figure 3-4, where comparison of the measured and simulated longitudinal bunch RMS size dependence on CCL RF phase is shown.

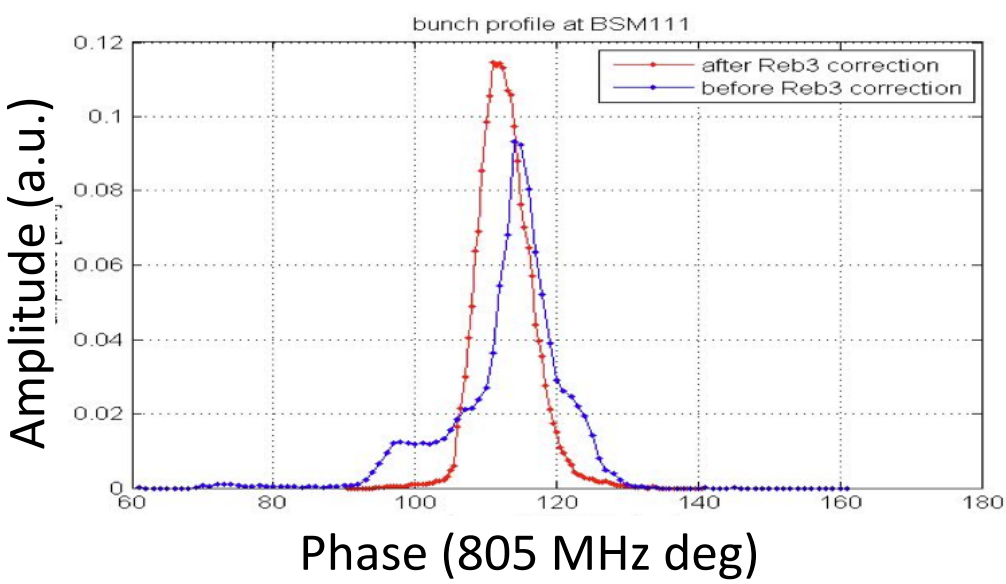

Figure 3-3. Longitudinal bunch profiles in the CCL for the cases of the nominal MEBT buncher phase (red) and shifted by 180° (blue).

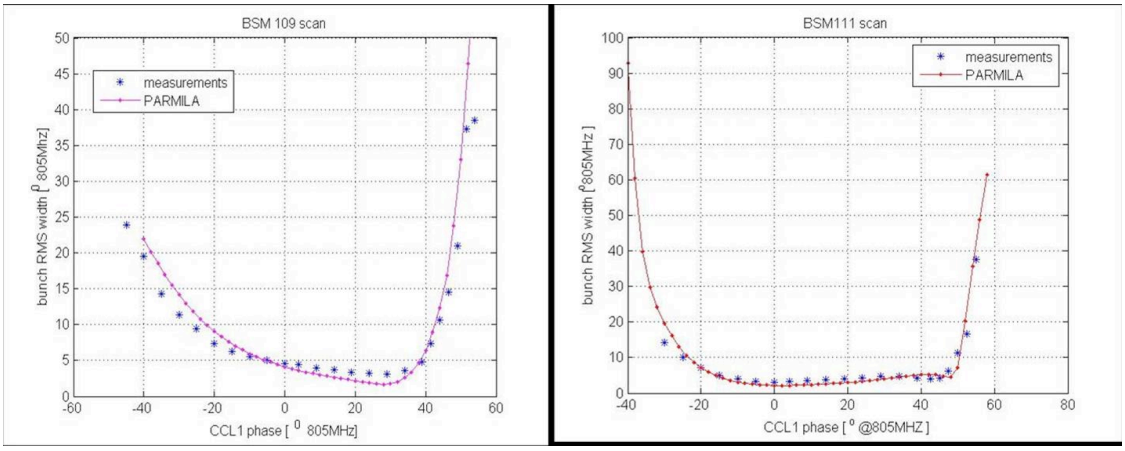

Figure 3-4. Comparison of the measured dependence of the longitudinal RMS bunch size on CCL1 RF phase with PARMILA simulations at two locations.

Time-of-flight energy measurements after the DTL-6 and CCL 1-3 were performed using several pairs of BPMs located in the CCL. Results are shown in Table 3-2. The measured beam energy is in good agreement with the design values. An estimate of the energy jitter and long-term drift was done by averaging BPM phase data taken during a 30-minute periods. Typical rms output energy spread is 0.08% and rms phase spread is 0.6 degrees of 402.5MHz.

Table 3-2. Beam energy measurements from direct time-of-flight measurements (taken at a different time than the data in Table 3-1)

Output Cavity	Design (MeV)	Measured (MeV)	Deviation (%)
DTL6	86.83	87.48 ±0.03	0.75
CCL1	107.16	107.36 ±0.12	0.19
CCL2	131.14	131.53 ±0.14	0.40
CCL3	157.21	158.08 ±0.40	0.55

After tuning the warm linac at low current (~15 mA), difficulties were encountered during the initial higher current operation due to the RF beam loading effect. As seen on the low-level-RF (LLRF) system screen snapshot in Figure 3-5, there is a significant cavity field and phase droop during the beam pulse transient. The LLRF bandwidth is not wide enough to compensate for the beam loading during the beam turn on transient. The detrimental effect of this on the beam dynamics is shown in Figure 3-6, where the bunch width along the pulse measured by a BSM in the CCL is shown. The uncompensated beam loading leads to significant variation of the average bunch phase within the pulse (left picture). An adaptive feed forward compensation was added to the LLRF system. As a result, the cavity field droop was corrected (right plots in Figure 3-5) and the beam phase became uniform along the bunch throughout the macro-pulse (right picture in Figure 3-6). With the addition of the feed-forward compensation a nominal peak current of 38 mA was readily transported through the warm linac with 100% transmission (within the BCM measurement uncertainty). The ability to measure a low level tail and halo in the longitudinal distribution could be very important for minimizing particles loss in the linac. Use of a secondary electron multiplier in the BSM design provides the possibility of varying detector gain over a wide range.

Performing measurements of the same distribution with different gains and stitching the pieces together allows obtaining a bunch profile with up to 5 decades of dynamic range as illustrated in Figure 3-7.

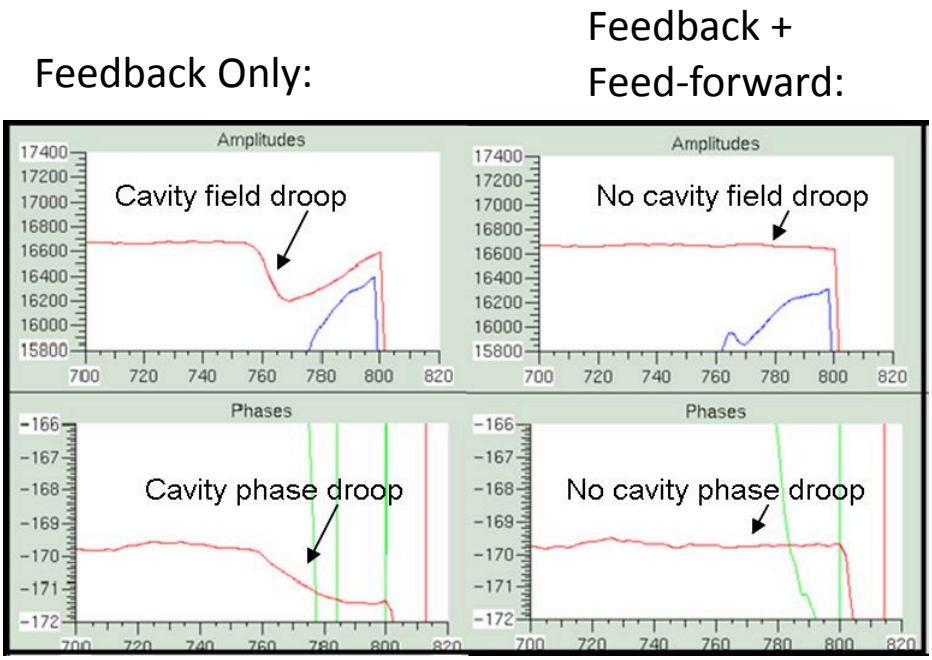

Figure 3-5. Cavity field and phase time waveforms indicating droop when the beam loading starts, with feedback alone (left). The feedback + feed-forward case (right) compensates for the beam loading. Beam is present from roughly 760 to 800 turns on the horizontal axis.

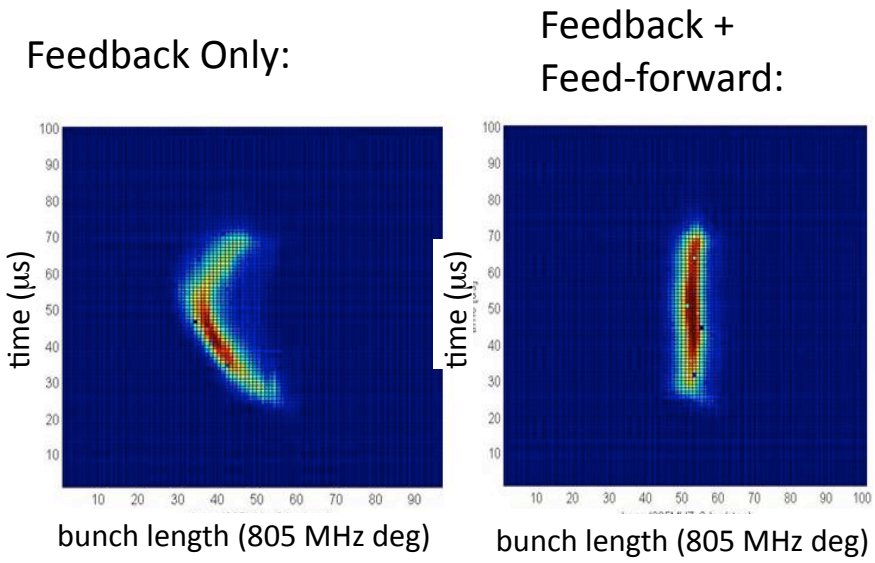

Figure 3-6 Phase width of the bunch (horizontal axis) along the macro-pulse (vertical axis) with feedback alone (left) and with both feedback + feed-forward (right) beam loading compensation.

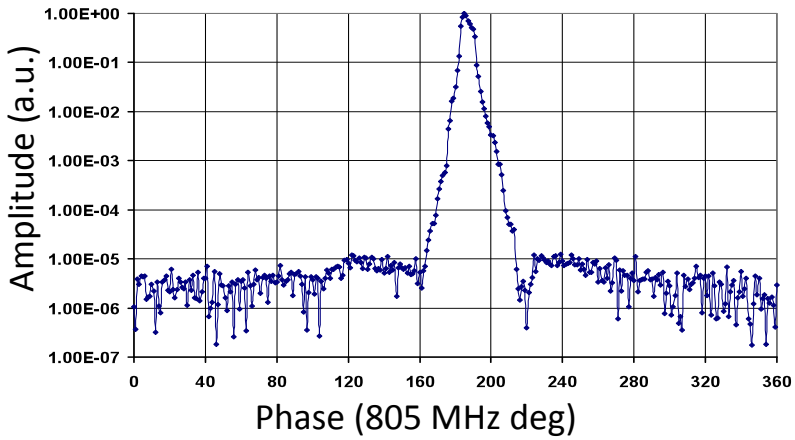

Figure 3-7. Large dynamic range longitudinal bunch profile measurement combined from several measurements with gain ranging from 1 to 3500.

3.1.2 Transverse measurements

Another initially puzzling observation was that after correcting the trajectory in the CCL using our standard model based algorithm, the beam was centered in the BPMs but losses were high. By manually adjusting dipole correctors, the losses could be significantly lowered, but the trajectory was then not necessarily centered in the BPMs. The problem was that there are fewer than two BPMs per betatron oscillation period in the CCL. In this case the correction algorithm can produce a trajectory with zero displacement at the BPMs but a significant deviation in between. To solve this problem we developed a beam based alignment technique [27]. An example of the trajectory corrected using the beam-based method is shown in Figure 3-8.

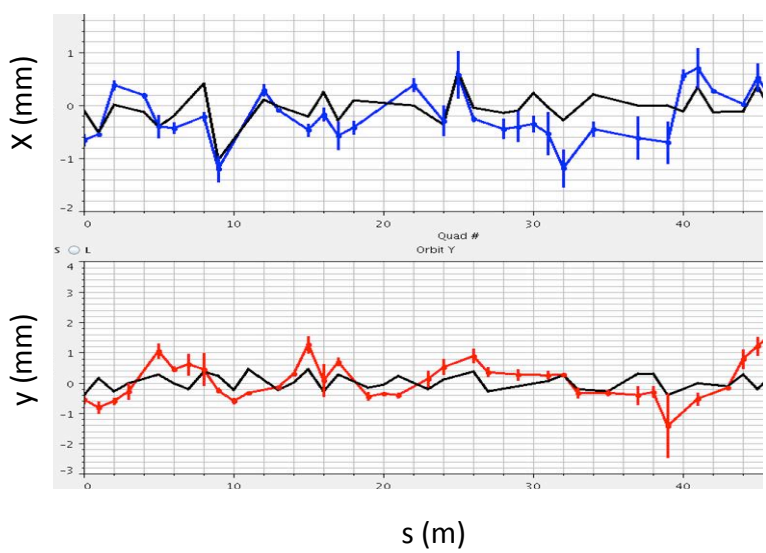

Figure 3-8. CCL beam based alignment application screenshot. Top blue graph: measured horizontal beam position in the CCL quads before correction; top black graph: after correction. Bottom red graph: measured vertical beam position in the CCL quads before correction; bottom black graph – after correction.

Transverse matching between the DTL and CCL is achieved by adjusting strengths of the four quadrupoles in the beginning of the CCL. We found that only minor adjustments were required to achieve a good match as judged by beam profile shapes in the CCL. The optimal transverse matching between the MEBT and the DTL is achieved by adjusting strengths of the four last quadrupoles in the MEBT (permanent magnet quadrupoles are used in the DTL). We found that a Gaussian profile is a good approximation for the best matched beam in simulations therefore the figure of merit in our matching experiment was a closeness of the measured profiles to a Gaussian. Figure 3-9 shows the effect of the matching quads adjustment on the beam profile. The measured beam profile follows a Gaussian profile down to ~4 rms when optimum matching is achieved. Deviation from the optimum results in developing well-pronounced tails [28].

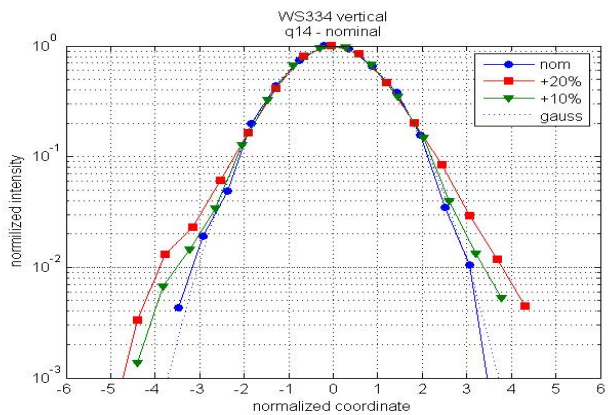

Figure 3-9. Effect of the MEBT matching quad change on the beam profile measured in the DTL. Blue circles – "best match"; green triangles – +10% from the nominal; red squares - +20% from the nominal, dash – Gaussian fit.

3.2 SUPERCONDUCTING LINAC (SCL) COMMISSIONING

By July 2005 all the installation and testing of the superconducting radio-frequency (SRF) cavities, cryomodules, warm sections, RF systems and diagnostics components was completed. The SCL equipment was ready for the beam commissioning [29,30], with the exception of the final cryomodule. Figure 3-10 shows the SCL cryomodules installed in the SNS linac tunnel. The SCL beam commissioning took place from July 15 through September 18 in 2005, with successful transport and acceleration of beam at 7.5 kW and 910 MeV [31]. The last cryomodule was installed following the SCL beam commissioning.

3.2.1 Superconducting Cavity and Cryomodule Performance

The SNS superconducting linac (SCL) is the first large-scale high-energy superconducting proton linac that provides high beam power utilizing H^- beams. The use of superconducting elliptical cavities for particles whose velocity is less than speed of light (β<1), makes this accelerator a very important milestone for learning operating conditions of this cavity type. Another important aspect of the superconducting linac is that it is operated under pulsed conditions, for which only the Tesla Test Facility at DESY has extensive experience for electron acceleration. The superconducting cavities in the SNS linac have the characteristic of being powered in a pulse mode (1.3-msec pulses at 60 Hz), which is unique among superconducting accelerators now in routine operation. The major specifications of the SNS SCL are summarized in Table 3-3.

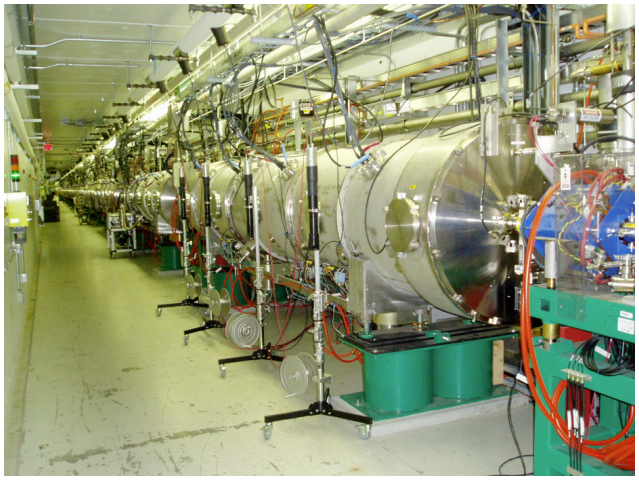

Figure 3-10. SNS SCL cryomodules installed in the linac tunnel.

Table 3-3 Major design parameters of the SNS superconducting cavities and cryomodules

Cryomodule Parameter	Medium Beta Section	High Beta Section
Output energy (MeV)	379	1000
No. of cryomodules	11	12
No. of cavities per cryomodule	3	4
Cavity Parameter	Medium Beta Cavity	High Beta Cavity
Geometric beta	0.61	0.81
E_oT (MV/m)	10.1 at β=0.61	15.8 at β=0.81
E_{peak} (MV/m)	27.5	35.0
H_{peak} (kA/m)	46.2 (580 Oe)	59.7 (750 Oe)
Q*Rs (Ω)	176	228
r/Q at design beta	279	483
Equivalent cavity length (cm)	68.2	90.6

Understanding the safe operational limits and limiting conditions are the most important factors to provide reliable cryomodule operation. At the initial low beam power required for SNS commissioning, the RF repetition rate was limited to 10 pulses per second (pps) and limiting gradients for all the SRF cavities were initially established at 10 pps and 4.4 K.

Since April 2006 the SNS SCL has provided beam acceleration for neutron production at output energies ranging from about 850 MeV to 1 GeV. At low repetition rate (20 Hz or less), the average limiting gradients of medium- and high-beta cavities are 16.7 MV/m and 17.5 MV/m respectively, which exceed the design gradients. The individual limiting gradients (powering one cavity in a cryomodule at a time) are about same as collective limits (powering all cavities in a cryomodule at the same time) at this low repetition rate. The overall phenomena are complex and the final operational cavity gradients must be determined individually for each cavity based on the equilibrium between electromagnetic, electron emission and thermal phenomena, each affecting the overall stability of the system on a pulse by pulse basis. Confidence in cavity performance has been slowly established, culminating in a demonstration of accelerating beam to the design 1-GeV energy at 15 Hz in February 2007. The operating gradients were set to about 85 % of the individual limiting gradients and 78 cavities out of 81 cavities were in service for this 1-GeV demonstration.

During the initial neutron production and beam studies, several extensive performance qualifications at various operating temperatures and RF repetition rates were conducted to better understand the SRF cavities/cryomodules. 60-Hz tests with all cavities powered in a cryomodule were first done in late 2007. Some unexpected features were observed at 60 Hz operation, including collective effects between cavities, HOM coupler issues, end-group stability, cavity-coupler interactions, and vacuum/gas physics. As the repetition rate increases the collective behavior (discussed below) becomes more evident and clearer thermal effects on operational stability are observed mainly due to field emission [32,33,34].

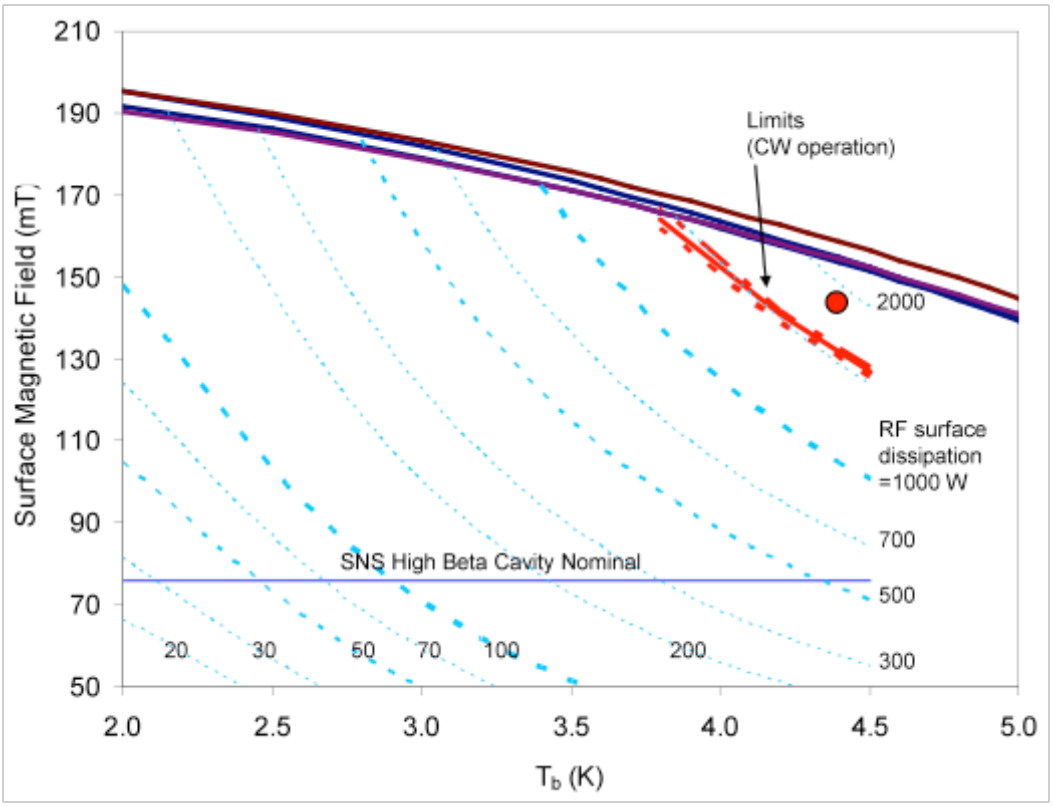

Figure 3-11. The critical field of niobium and dynamic loss of the SNS high beta cavities as a function of temperature. The dot represents the surface magnetic field of the best-installed cavity, which is higher than the CW limitation. The dashed lines are equi-surface RF dissipation calculated with surface resistances. The critical magnetic fields as a function of temperatures are taken from other experimental data and show some variation. The CW operation limits in the figure corresponds the heat flux transition from the nucleate boiling regime to the film-boiling regime.

The design operating temperature of the system is 2.1 K, just below the helium superfluid transition at 2.17 K. The initial superconducting cavity testing was done at 4.4 K, and it became apparent that the achievable gradients at 4.4 K not only met the original SNS design values, but also exceeded them in a significant number of cavities. Once the sub-atmospheric (2.1 K) part of the cryogenic plant became operational, additional tests of the maximum achievable gradients clearly indicated that the limiting factors in the cavities are not related to the operating temperature. The SNS SRF cavity parameters and their interplay were reevaluated, to calculate the possible range of operating parameters that can be achieved in pulsed conditions. The transient nature of pulsed operation allows large variation of temperatures within the niobium surface. During the pulse the surface resistance of the material can increase substantially, and then recover between pulses. At the SNS duty factor and pulse length there are

no BCS limitations up to the critical field when the helium temperature is less than 4.5 K. This is primarily due to the pulsed operation and the relatively low operating frequency as shown in Figure 3-11, which was verified with cryomodule tests at 60 Hz, both at 2 K and 4.4 K. However, in routine operation at 30 Hz or higher the SNS SRF cavities must run at 2.1 K since the existing cryo-plant is not designed to provide the required mass flow needed at 4.2 K.

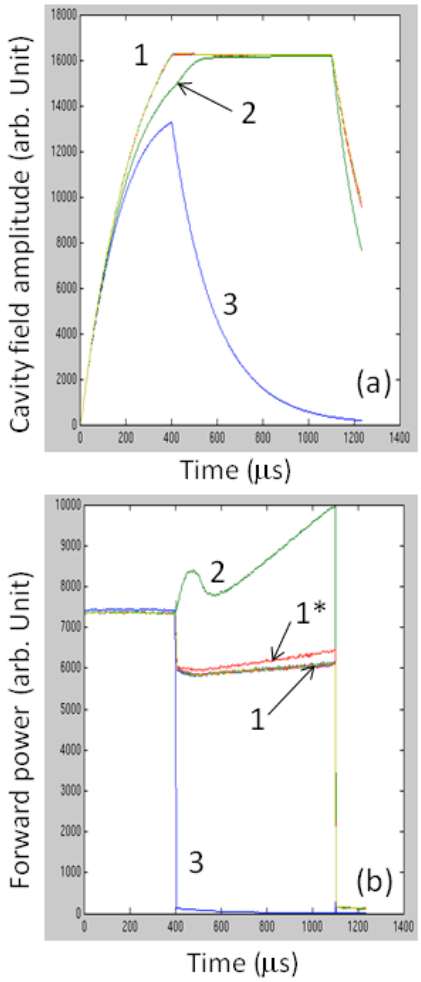

Figure 3-12. Measured waveforms at a partial quench. (a) cavity field and (b) forward power in voltage scale. Constant RF power in open loop is used for cavity filling and feedback control starts after cavity filling at 400 μs. 1: normal operating condition. 1*: slightly higher RF power is needed to keep the cavity field, which is a precursor of partial quench. 2: cavity field does not reach the set-point during the cavity filling time at the same power used in the previous pulses. Much higher RF power is needed to reach the set-point. The decay slope of the cavity field, after RF is turned off, indicates that the full quench is not developed. 3: cavity field build-up is less than the previous pulse (2) and feedback control truncates RF. The quench develops more than the pulse (2), but it does not reach a full quench.

The measured gradients of field emission onset are about 10 MV/m ±3MV/m. During low repetition rate operation, operating gradients were somewhere between the field emission onset and 90% of the individual limiting gradients. A major limiting factor is field emission manifested primarily by the thermal instability at the end group, which leads a partial quench and/or gas burst. The end group of the SNS SRF cavities has reasonably good thermal stability against material defects because of the low surface magnetic field. This region is, however, vulnerable to thermal deposition from field emission,

since it was made of low residual resistivity ratio (RRR) niobium and is cooled only through indirect conduction. When the end group reaches a thermal run away condition, an intermediate or partially quenched state can be temporarily sustained, which is characteristic of low field thermal run away. Figure 3-12 shows typical waveforms of cavity field and forward power for a partially quenched state. The cavity cell region has opposite thermal stability characteristics, having higher thermal stability against a field emission heat loads than the end group but having fast thermal runaway with localized heating from material defects or heavy multipacting. The cell region limits only a few cavities.

In addition to individual cavity radiation limits, collective radiation effects have been observed. By collective we mean that electron heating from a cavity affects neighboring cavities. Increased heating by these collective effects is clearly observed when the repetition rate is 30 Hz or higher. Heating of cavity elements is driven not only by the amplitude, but also by the relative phase of neighboring cavities. This collective effect is observed in many cryomodules, most clearly at higher repetition rates. The electron-impact location depends on not only the field strength but also relative phases and amplitudes between neighboring cavities as shown in Figure 3-13. Also when electrons hit any intermediate temperature region (<20 K) in the cavity string, bursts of gas are observed, which cause vacuum trips and can redistribute gas, resulting in changes in cavity and/or coupler conditions.

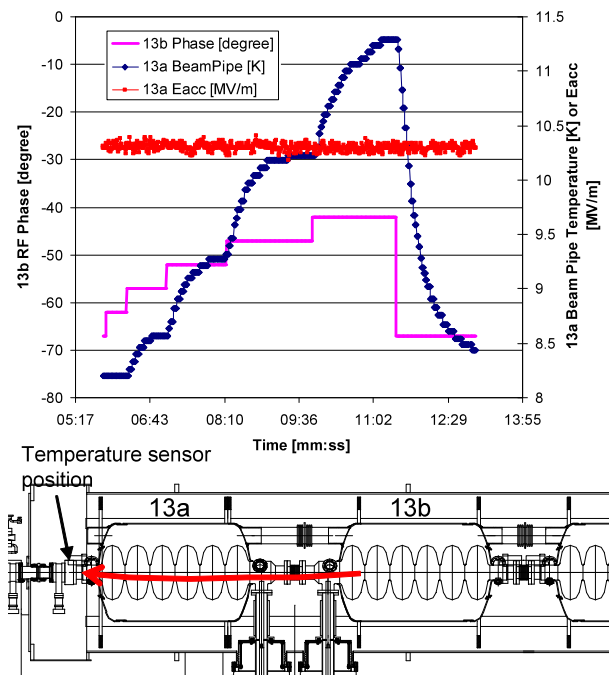

Figure 3-13. Example of cavity 13a beam pipe temperature excursion caused by changing the phase of cavity 13b (top). The bottom figure indicates the relative geometry of the cavities within the cryomodule.

Figure 3-14 compares the average gradients at different conditions. At low repetition rate, individual limits are about same as collective limits. All data in Figure 3-14 were taken in closed loop operations with a 1200-μs RF pulse width including the cavity filling time, except '10 Hz individual limits in open loop', where constant RF power was applied at 10 Hz and a 1200-μs RF pulse width. The difference between limits in open and closed loops results from RF field regulations and the much longer duration at the highest field in closed loop. There are larger limiting gradient reductions in high beta cavities between the 10-Hz individual limits and the 60-Hz collective limits, since there is a stronger collective effect in high beta cavities where electron acceleration is more efficient. The safe and reliable operating setpoints cannot be determined with single cavity tests. This requires a careful evaluation of collective behaviors by simultaneously powering all cavities in a cryomodule.

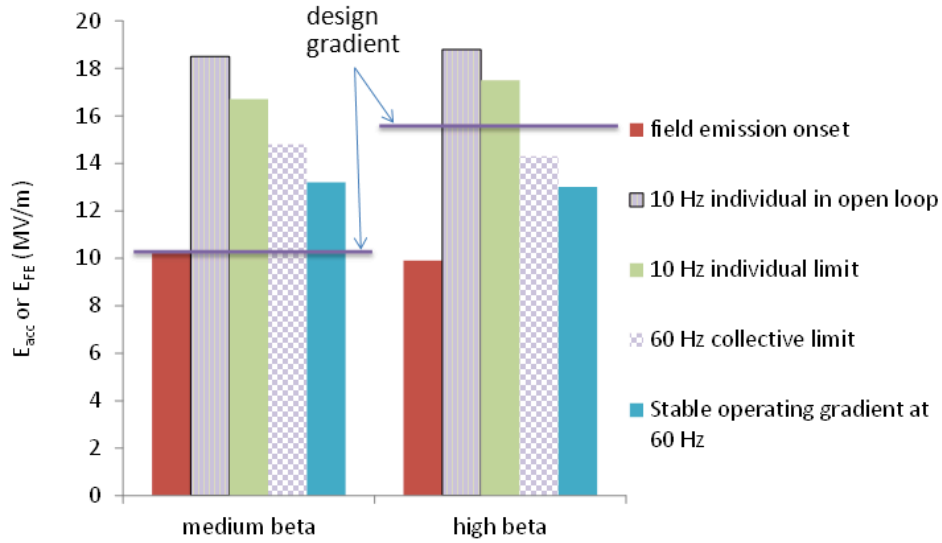

Figure 3-14. Cavity performance statistics for different operational conditions.

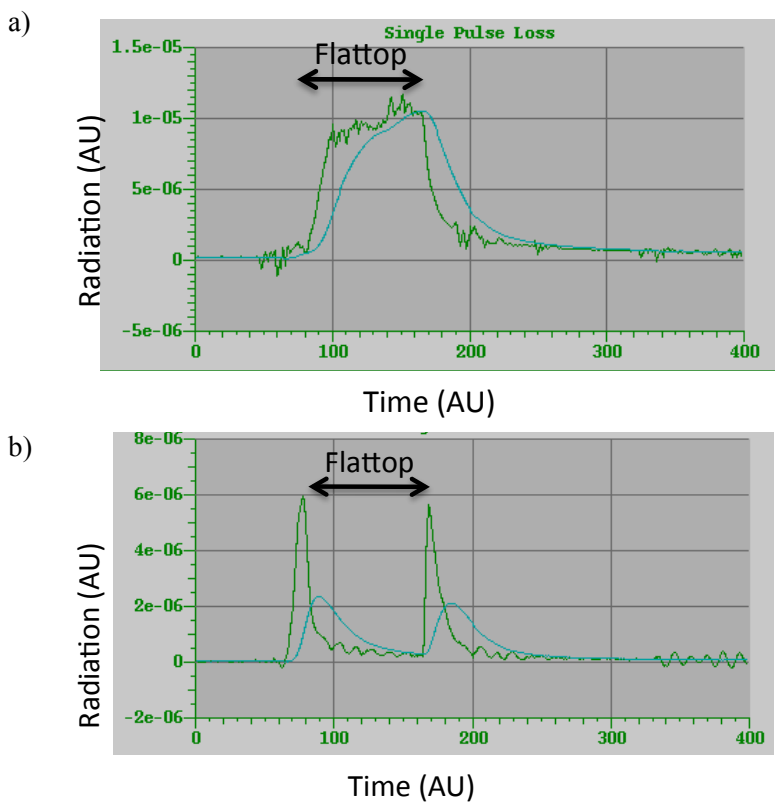

Figure 3-15. (a) Normal radiation waveform from field emission, which follows the cavity field shape. (b) Abnormal radiation waveform with double spikes corresponding to the field rise and fall.

One interesting observation is that radiation waveforms from some cavities do not follow the typical field emission pattern, shown in Figure 3-15 (a). Some cavities show radiation waveforms with spikes at the end of RF pulses and/or during the cavity filling as shown in Figure 3-15(b). This radiation waveform can be caused by acceleration of non-resonant electrons from multipacting, and is thus observed mainly in

high beta cavities. The origin of this multipacting in the SNS cavities seems to be around end groups rather than the fundamental coupler side (FPC) and on the surface of cells, since it depends on the cavity field. A partial quench sometimes accompanies this electron activity. Mostly multipacting can be processed out but very careful attention is needed, especially during the initial conditioning period since a weak component could be damaged by the initial violent electron activity. Only a few cavities are limited by this phenomenon.

Multipacting at the FPCs is observed, occurring primarily near the full travelling wave condition during filling time and field decay after the RF is turned off and/or field flattop at high beam loading. The aggressive multipacting band starts at about 300 kW or higher in some FPCs. Positive DC biasing at less than 1 kV on the inner conductor efficiently suppresses the multipacting at FPCs. Figure 3-16 shows the electron probe signal placed at the vacuum side of a FPC window without a bias.

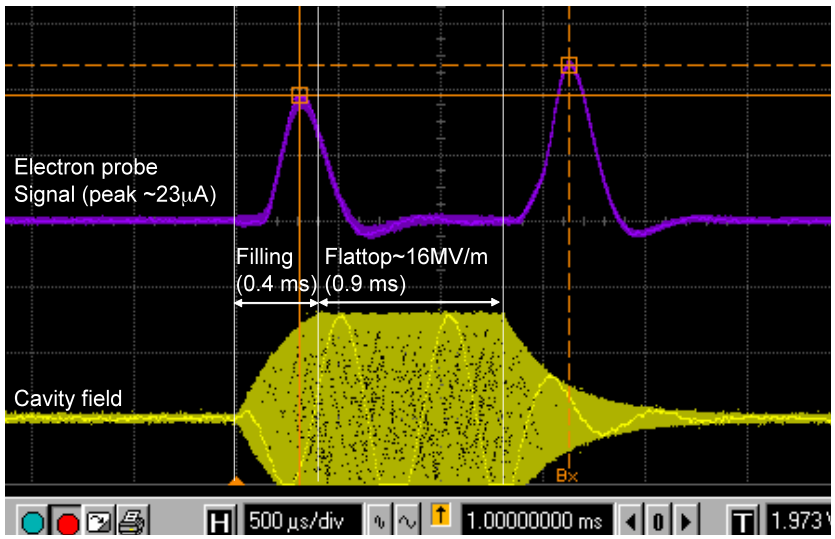

Figure 3-16. Typical electron probe signal, indicating spikes during the cavity fill, and end of pulse.

The Higher Order Mode (HOM) Filters designed to damp longitudinal modes at the bunch harmonics have shown behavior that may lead to failure of their RF feed-throughs. About 15 % of installed cavities in the SNS SCL show abnormal signals through HOM feed-throughs. Observations and physical conditions around HOM couplers imply that HOM coupler failures and/or deteriorations seem to be a result of electron activities originated by a combination of multiple causes such as electromagnetic field at the HOM coupler, multipacting, field emission, and even a gas discharge. This prevents the full utilization of the associated cavities' gradients due to concern of catastrophic failure. The SNS HOM coupler is a notch filter type where high electromagnetic fields exist in the form of a standing wave that can be easily deformed by external perturbations such as any electron activity around the coupler. This concern has led us to either decrease gradients or turn off cavities (temporarily or permanently) showing this sort of anomalous behavior.

The observed dynamic detuning agrees with expectations in most cavities. The detuning coefficients are about 3-4 Hz/(MV/m)^2 and 1-2 Hz/(MV/m)^2 in medium and high beta cavities respectively. A few cavities show higher detuning coefficients at higher repetition rates, implying that dynamic resonance conditions are statistically established in these cavities. Piezo tuners are installed to compensate dynamic detuning; however there has not been a need to utilize them.

SNS requires a high reliability/availability for operation as a user facility. Cryomodules consist of many components and devices that must function properly, as the ultimate cavity performance is limited by the weakest link in the entire chain of cavity and support equipment. As we better understanding the

underlying physics and engineering aspects of SCL operation, including all sub-systems and supporting systems as a whole, the SNS SCL is providing more stable and reliable operations.

3.2.2 Superconducting RF Setup

The primary commissioning task in the SCL was setting the RF phase for the 81 cavities in the SCL, each of which is powered by an individual klystron. Each cavity is run at its maximum safe operating gradient, but the setting of the phase requires a measurement relative to the beam. The SCL cavities have only 6 cells and the effect of acceleration on the beam is much like an ideal RF gap (*b* changes only slightly in each cavity). As a result, the phase scan technique described in the section 3.1.1 and shown schematically in Figure 3-1 can be employed throughout a 360 degree range [35]. The measurement data is easily matched to model predictions to determine the input beam energy, cavity amplitude and klystron phase offset from the synchronous phase [36]. Figure 3-17 shows a typical scan for an SCL cavity. The measured beam response is much like the sinusoidal result expected from an ideal RF-gap, and all cavities show a similar behavior. Solving for the beam energy, RF amplitude and phase offset is straightforward. However it is important to ensure RF is not affecting the beam in between the cavity being scanned and the two BPMs used to measure the Time-of-Flight response. For the SNS arraignment of cavities and diagnostics there can be up to 7 intervening cavities, and in order to proceed through the 81 cavities quickly we have implemented a LLRF feature to allow "blanking" of the RF whenever beam pulses are triggered for these measurements. This allows the entire SCL RF system to be turned on and left on at a typical 60 Hz rate, with beam pulses intermittently applied at 1 Hz for the phase setting studies. The entire SCL linac RF setup can be completed in a few hours with this method.

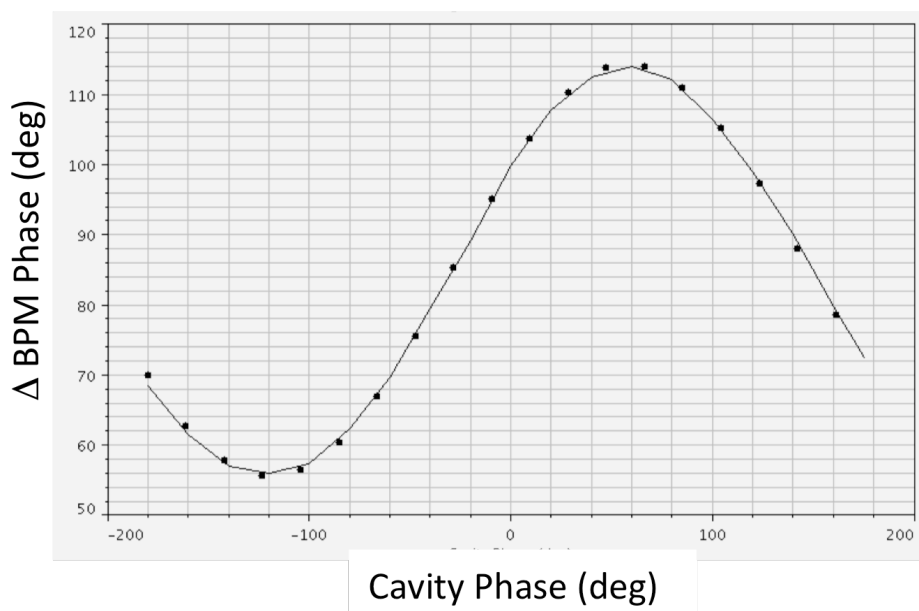

Figure 3-17. Example downstream BPM phase response vs. an SCL RF phase scan. The solid line is a measurement and the dots are model predictions after matching the input beam energy, cavity voltage and RF phase offset. All SRF cavities exhibit a similar sinusoidal response.

To avoid repeating beam-based measurements to correct the SCL cavity phase settings whenever an upstream cavity phase or voltage changes, a model-based technique has been developed to calculate the changes in beam arrival time in downstream cavities when a cavity fails, and to automatically adjust the downstream cavity phase settings [37,38]. Turning off an upstream cavity can result in changes in the arrival time at the downstream end of the linac equivalent to over 1000 degrees. Checks show that the

recovery technique is accurate to within a few degrees. This technique has been used often to compensate for changes in SCL cavity operating levels and for beam studies.

Another technique that can be used to measure the cavity phase setpoint relative to the beam and the cavity amplitude is the drifting beam technique [39]. This technique involves drifting the beam through an unpowered cavity. The beam readily excites the cavity and by comparing the measured cavity excitation time response with model based predictions it is possible to determine the proper cavity phase setpoint and the cavity amplitude. This technique requires accurate knowledge of the beam energy and beam current.

3.2.3 Transverse Beam Matching

Understanding and controlling the transverse beam size is an important tool in beam loss minimization. At SNS there are wire profile measurements throughout the warm linac and the transport section from the linac to the Ring. Also laser profiles are available in the superconducting linac section [40]. At SNS the primary transverse matching locations are at the end of the MEBT, at the entrance to the CCL and at the SCL-HEBT transition. The matching process involves three steps: 1) obtaining beam profiles at least three locations in the matching region, 2) solving for the beam Twiss parameters (*a,b* and emittance) upstream of the profile measurements that best matches the measured beam sizes, and 3) adjusting strengths of quadrupoles located downstream of the Twiss solution point in step 2, to produce a desired set of downstream Twiss parameters. The beam model used here is a beam envelope method, which accounts for space charge [41]. This method works for the minimal phase advance in the matching regions, and requires accurate knowledge of the RF setup in accelerating regions.

An example of beam matching is shown in Figure 3-18, applied at the start of the HEBT transport line. Figure 3-18 a) shows the measured beam sizes (dots) and envelope model simulations (lines) using the solved upstream Twiss parameters to best match the measurements (step 2 above). Blue curves represent the vertical beam size and red represents horizontal beam size. The lattice in the start of the HEBT (first 25 m in figure 3-18) is designed to be a FODO channel. After adjusting the last few quadrupoles upstream of the HEBT to provide the design Twiss at the start of the HEBT channel (step 3 above), the beam is better matched exhibiting the expected well-behaved FODO structure (similar horizontal and vertical beam sizes along the channel). Additional matching examples using a similar method are described in references [42,43].

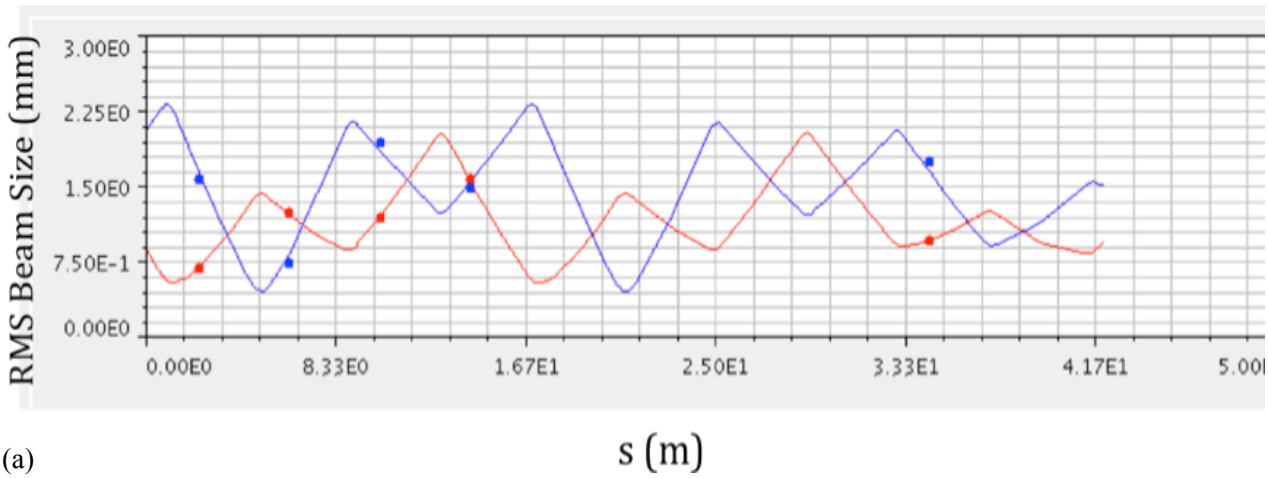

(a)

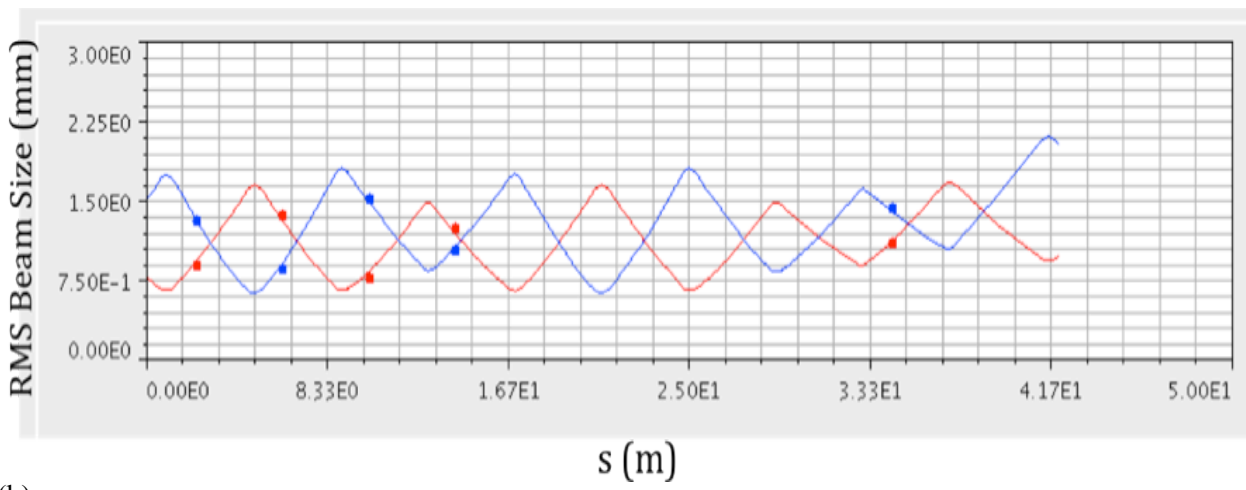

(b)

Figure 3-18. Measured beam size (dots) compared to expected RMS beam envelope size (lines) at the start of the HEBT. Red is horizontal, blue is vertical. a) before matching and b) after matching.

4. RING COMMISSIONING AND OPERATION

The initial stage of the ring commissioning progressed very quickly. On January 12, 2006 final approval from the US Department of Energy was given to deliver beam to the ring. On January 13 beam was commissioned through the 162-m long HEBT beam transport line from the linac to the ring (to a dump at the ring injection). On January 14 short ~ single turn (~1 μs) pulses (mini-pulses) were injected into the ring, and by January 15 more than 1000 turns of beam storage was achieved. On January 16 beam was extracted from the ring and directed to the ring extraction dump 75 m downstream of the ring, and accumulation of seven mini-pulses demonstrated. By January 26 the beam intensity was increased to $1.3\text{x}10^{13}$ protons per pulse (ppp) to meet the commissioning goal of $>1\text{x}10^{13}$ ppp. By the end of the commissioning period on February 13 accumulation of $1\text{x}10^{14}$ ppp (unbunched) was demonstrated and some preliminary measurements of beam instability thresholds were made.

The second ring-commissioning period was April 8 to May 31, 2006. On April 28 1.6×10^{13} ppp was delivered to through the RTBT transport line to the spallation target, successfully marking the end of the construction and initial commissioning of the SNS facility.

During the July and August 2006 running period, the accelerator provided routine beam delivery for neutron production. On November 30, 2006 accumulation and storage of 9.6×10^{13} ppp was demonstrated, setting a new record for the highest number of protons per bunch of any proton ring. Also in November 2006, when the beam parameters were 30 kW at 5 Hz, SNS became the world's highest peak neutron flux spallation neutron source. To date the range of beam energies accumulated in the Ring is 839 to 931 MeV. On Aug. 11, 2007 the beam power surpassed 180 kW, and SNS became the highest power pulsed neutron spallation source. The highest number of protons in a single bunch achieved to date is 1.55×10^{14}, to be compared with the design value of 1.5×10^{14} ppp.

Much of the ring commissioning was performed using single mini-pulse injection, where the beam from the ion source is chopped to allow just a single turn (~690 ns bunch length) of beam to be accelerated. For such a beam pulse the power is low enough (~12 W) that beam loss is of little concern, and because beam is injected into the ring with an offset relative to the closed orbit it is possible to measure the betatron tune, closed orbit, injection position and angle, magnet polarities and strengths, etc.

4.1 LATTICE

4.1.1 Closed Orbit

An orbit correction application [44] is used to measure and flatten closed orbit distortions in the ring. While it may be used to correct the orbit to any custom orbit, we typically use it to flatten the orbit to the centers of the beam position monitors (BPMs) located outside of the injection bump region. The BPMs provide the horizontal and vertical beam position signals averaged over several turns effectively yielding the orbit distortion. A model of the ring is synchronized with the live accelerator, and a linear orbit response map is generated over all BPM-corrector pairs to be used. The corrector fields and limits are fetched from the live accelerator and fed to an optimizer which searches for the best solution satisfying the limits while minimizing the orbit distortion predicted from the orbit response map. As solutions are found, the application displays them to the user who may stop the optimizer when satisfied, then view and apply the correction. Typically the procedure is iterated a few times to achieve the smallest orbit distortion. This same application is also used to steer the beam in the HEBT and RTBT beam lines.

A typical closed orbit measurement result is shown in Figure 4-1. The first BPM in the plot is just after the stripper foil, and the last is just before the foil. The large "ears" at the beginning and end of the plot show the beam displacement due to the injection kickers, which are at their maximum values at the beginning of injection, when the closed orbit measurement is typically performed. The orbit is typically corrected to within ±2 mm according to the BPM system [45].

4.1.2 Lattice Beta Functions

The horizontal and vertical Twiss functions in the ring were measured using a Model Independent Analysis of turn-by-turn BPM data [46]. This method is robust against random measurement noise, and does not require alteration of any magnet currents. However, with this method, the Twiss functions can be determined only up to a scale factor. Figure 4-2 is a plot of the measured horizontal and vertical beta functions determined using the MIA method, compared with an online model prediction. A difference between the model and the measurement of up to 12% is observed in both planes. Since the beta function

discrepancy is not four-fold symmetric, it cannot be explained by errors in the symmetric quadrupole family set points. Investigations are underway to locate the source(s) of the discrepancies.

4.1.3 Tune

The tune measurement is usually accomplished by fitting a decaying sine wave to the turn-by-turn position data for single mini-pulse injection. To date we typically operate the ring at normal chromaticity, so the oscillations of the injected mini-pulse die out after about 50 turns. With such a limited number of turns, fitting the data with a sine wave gives a tune measurement that is more accurate than a simple FFT. An application to calculate the FFT is also available but it is used less often. The design betatron tune of the Ring is (6.23, 6.20), but in practice these values can vary somewhat and give an equally low beam loss, or even slightly better, result. Nominal values tend to be approximately (6.21, 6.18).

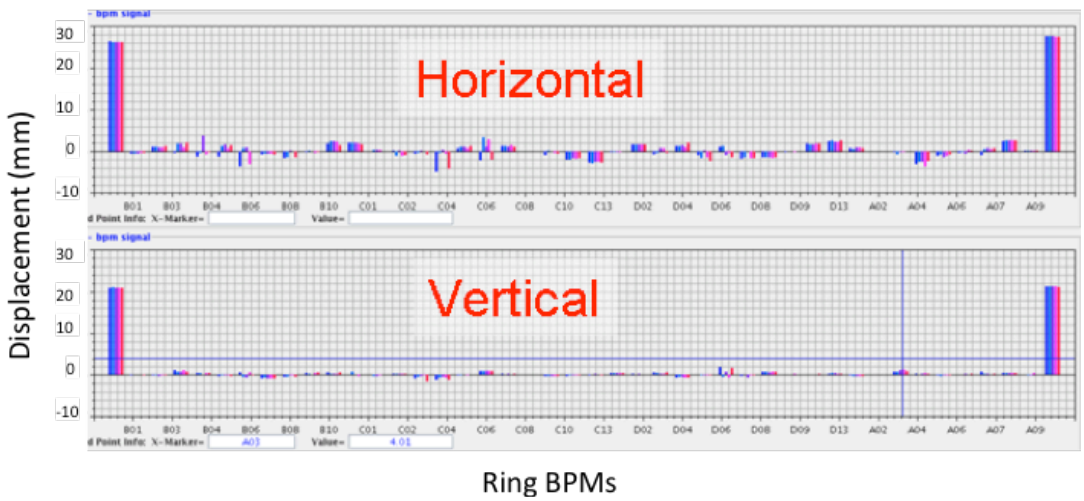

Figure 4-1. A screen shot of the closed orbit over the circumference of the Ring. Figure reproduced from Ref. [45].

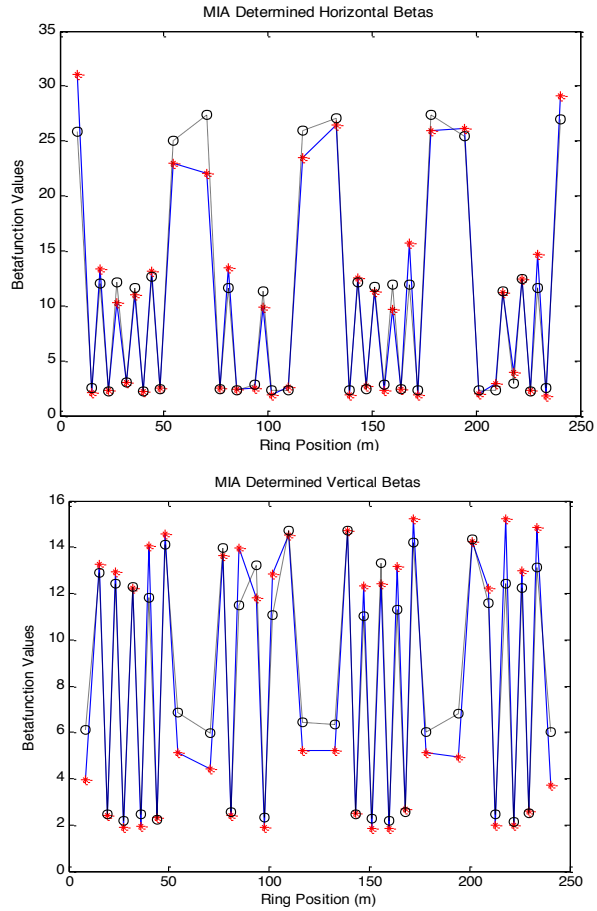

Fig. 4-2. Comparison of horizontal (top) and vertical (bottom) beta functions determined using the MIA method (red +) with the design values (black circles). The stripper foil is located at position 0 m on the horizontal axis.

4.1.4 Transverse Coupling

The usual method of measuring transverse coupling in the ring by measuring the response to a kick to the beam is not possible due to lack of a kicker. Instead, the coupling was measured by injecting single mini-pulses at a large offset relative to the closed orbit in the vertical plane, and very close to the closed orbit in the horizontal plane. Under these conditions a perfect ring with no coupling would exhibit large oscillations in the vertical plane and very small oscillations in the horizontal plane. However, our observations showed significant horizontal oscillations with an envelope that depends upon the difference between the horizontal and vertical betatron tunes, as shown in Figure 4-3 [47].

To analyze the data we adopted the formalism from Sagan et al. [48]:

$$\begin{pmatrix} x \\ y \end{pmatrix} = \begin{pmatrix} A_x\sqrt{\beta_x}\cos\psi_x + A_y\sqrt{\beta_x}(C_{11}\cos\psi_y - C_{12}\sin\psi_y) \\ -A_x\sqrt{\beta_y}(C_{22}\cos\psi_x + C_{12}\sin\psi_x) + A_y\sqrt{\beta_y}\cos\psi_y \end{pmatrix}$$

where x and y are the horizontal and vertical turn-by-turn beam positions, β_x and β_y are the betatron functions at the BPM, A_x and A_y are amplitude factors to be determined, C_{ij} are the coupling coefficients

to be determined, and $\psi = n\omega + \phi$, where n is the turn number, ω is the normal mode frequency, and ϕ is an arbitrary offset which varies from one BPM to the next. The C_{ij} coefficients are a measure of the coupling with $C_{ij} \sim 1$ corresponding to full coupling. C_{11} is the normalized amplitude of the horizontal component of the motion that is in phase with the vertical motion, C_{12} is the out of phase component, and C_{22} is the vertical component in phase with the horizontal motion.

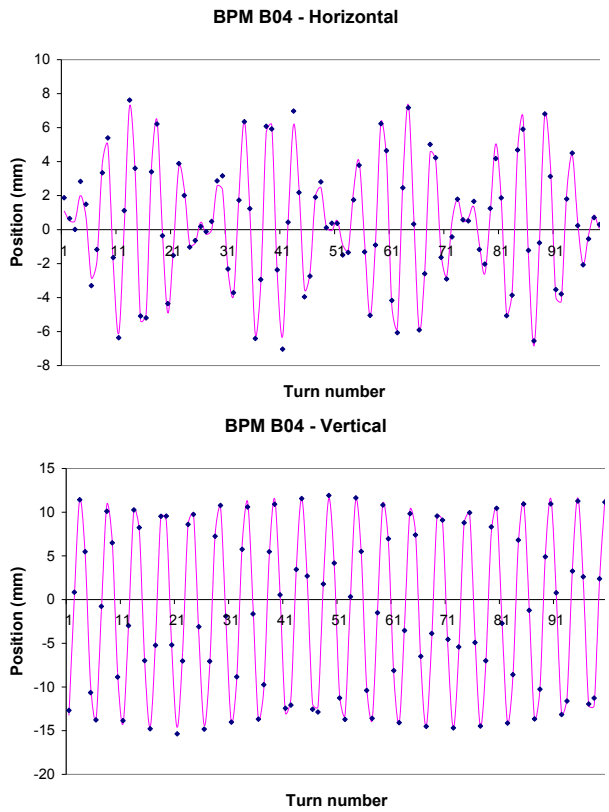

Fig. 4-3. Turn-by-turn beam position oscillations of a single mini-pulses injected into the ring, measured by a BPM in the ring. Top: horizontal oscillations. Bottom: vertical oscillations. Measured positions are shown as dots and the lines show the fits. Reproduced from Ref. [47].

An example fit to the data for one of the 44 BPMs is shown in Figure. 4-3, and the resulting coupling coefficients at all 44 BPMs (excluding the non-functional ones) are shown in the top of Figure 4-4. After energizing skew quadrupole corrector magnets the coupling coefficients were reduced to those shown in the bottom of Figure 4-4. Although the skew quadrupole corrector magnets are distributed at many points around the ring they all have similar effects on the coupling correction, and there is no strong preference at this time of which ones to use. A likely source of the coupling is the ring injection section, where we have strong multipole components from the chicane magnets. For this reason we chose to energize six vertical skew quadrupole corrector magnets in the vicinity of the injection section to about half their maximum strength to empirically minimize the coupling. The residual coupling does not appear to adversely affect the performance of the ring at this time.

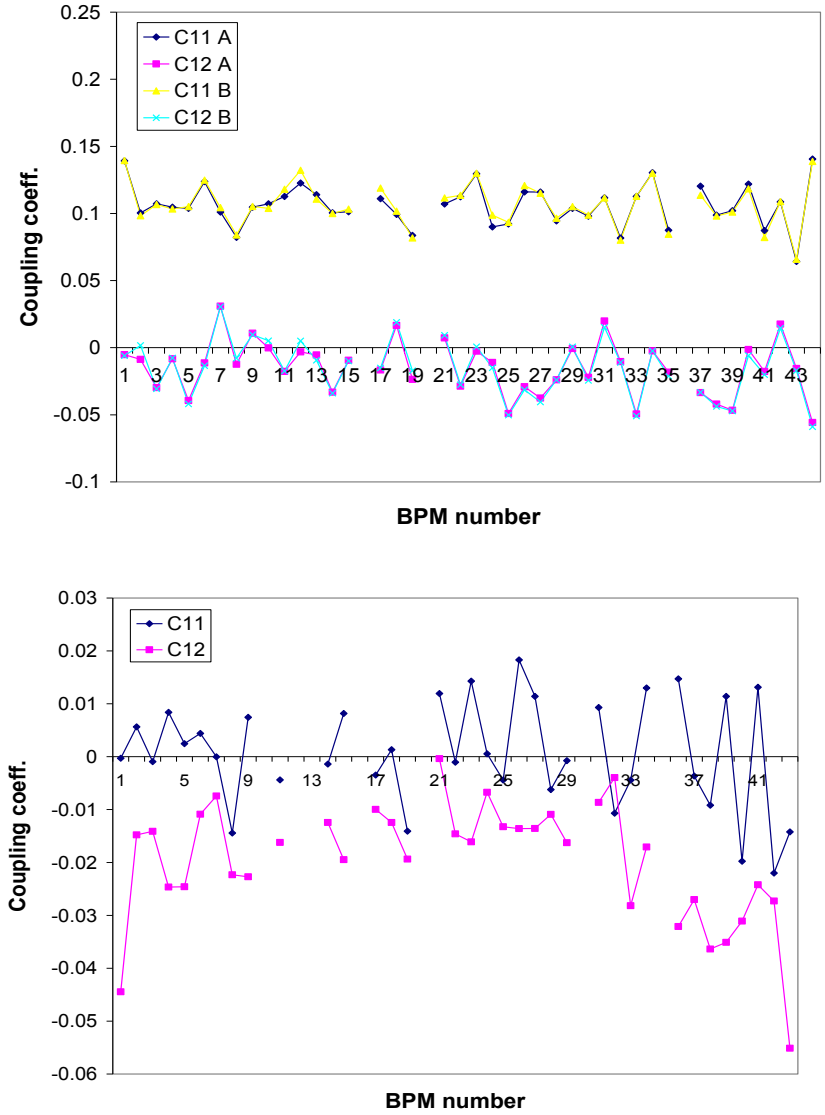

Fig. 4-4. The coupling coefficients C_{11} and C_{12}, before (top) and after (bottom) correction. The top plot shows two different measurements to demonstrate the reproducibility. Reproduced from Ref. [47].

4.2 INJECTION SYSTEM

The ring injection section includes four chicane magnets that merge the incoming H^- beam with the circulating proton beam at the charge-exchange stripper foil. These same magnets also direct the H^- beam that misses the foil, and the H^0 beam partially stripped by the foil, to the injection dump beam line.

An important step in tuning the accumulator ring is the measurement and control of the injected linac beam position and angle at the injection stripper foil with respect to the circulating closed orbit in the ring. These parameters have a significant impact on the final distribution of the beam in the ring. Additionally, it is important to align the angle of the incoming linac beam with the closed orbit at injection in order to provide good beam circulation in the ring and to prevent unwanted emittance growth.

An application was developed for measurement and control of the linac injected beam position and angle at the foil. The measurement portion relies on single mini-pulse turn-by-turn BPM data. The data from multiple BPMs in the ring is fit to a damped sine function in order to provide the initial position and phase of the beam at the location of each BPM. Then a model initialized with live machine optics (referred to as the online model) is used to back-propagate this position to the ring injection point. A source of error in this method is the difference between the machine optics and the online model optics. To minimize this error, the results of several BPM predictions can be averaged, and we typically use the first four or five BPMs closest to the stripper foil.

In the control portion of the application, the user provides a desired change in the position and angle of the injected beam, and chooses correctors in the upstream HEBT transport line to make the change. The application uses the live optics in the HEBT to determine the change in the corrector strengths to produce the desired change in the beam position and angle at the foil.

Early in the ring commissioning period it was discovered that the nominal chicane magnet set points cause a large (~14 mm) closed orbit distortion and poor beam injection into the ring. This was traced to a design change made in 2000 that had the unintended consequences of the closed orbit offset and large beam losses in the ring injection dump beam line. With new injection chicane magnet settings good injection into the ring and a good closed orbit were attained, but not simultaneous good transmission of the H0 and H− waste beams in the injection dump beam line. A short-term solution, put into place in November 2006, was to use a primary stripper foil 5 mm wider, 5 mm taller, and about 50% thicker. This foil fully intercepts the incoming H− beam so there is little, if any, H− beam entering the injection dump beam line, allowing the beam line to be optimized for just a single waste beam and reducing beam loss in the injection dump beam line. However, this was not a long-term solution because of the increased beam loss in the ring caused by increased foil scattering.

The mid term solution involved shifting the fourth chicane magnet 8 cm beam left to place the H0 and H− beams in the good field region of the this magnet; enlarging the gap of the injection dump septum magnet; adding a C-magnet just downstream of the septum magnet to allow individual control over the H0 and H− beam trajectories; and adding a wire scanner profile monitor, a beam position monitor, and a high-sensitivity beam current monitor to the diagnostics suite. These modifications, illustrated in Figure 4-5, were put into place between April 2007 and March 2008 [49].

Future modifications will include enlarging the beam aperture for a few meters of beam line downstream of the quadrupole magnet to relieve an aperture restriction, and adding a beam imaging system nearby the vacuum window to measure the beam position and distribution on the injection dump.

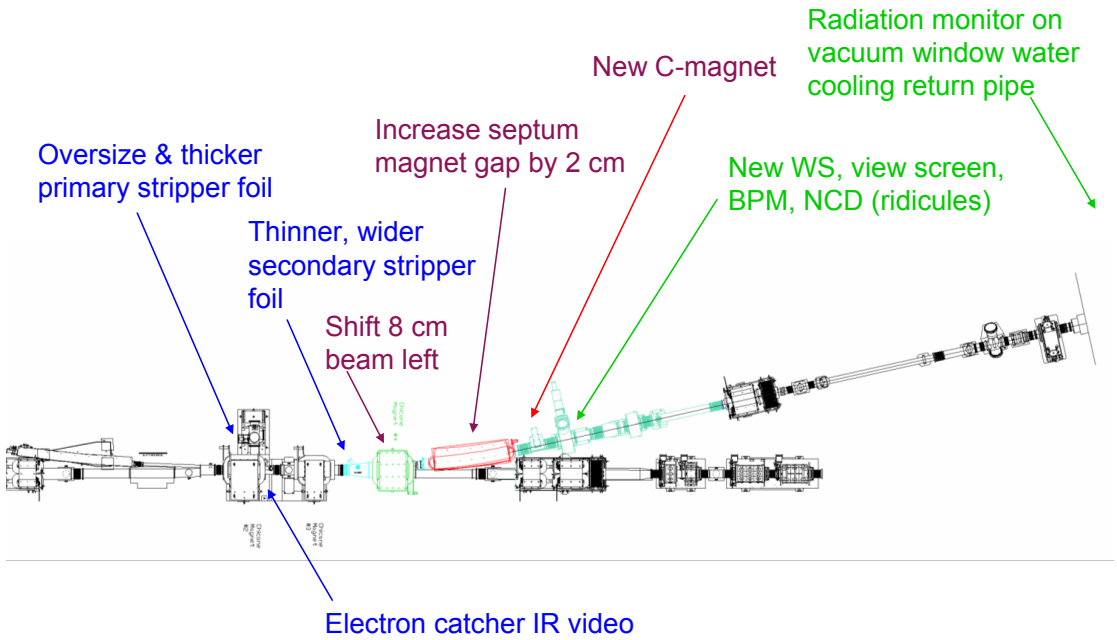

Fig. 4-5. Schematic diagram of ring injection area and the first part of the injection dump beam line, showing the various modifications that have been made since the start of commissioning. Reproduced from Ref. [49].

4.3 STRIPPER FOILS

Nanocrystalline diamond stripper foils [50] have been in use from the beginning of formal operations in 2006. These foils were successfully used with no failures until May 3, 2009, when a rash of foil and foil holder failures began to occur, resulting in a reduction of the operational beam power. The foil system failures were traced [51] to three primary causes: 1) convoy electrons stripped from the incoming H^- beam circle around the magnetic field lines and after one half of a revolution hit the foil bracket, causing it to melt; 2) cathode-spot in-vacuum breakdown, due to the foil charging up from secondary and thermionic electron emission, and the subsequent arcs that damage the foil bracket; and 3) convoy electrons that reflect back up into the vacuum chamber and hit and the foil bracket, causing damage to the bracket.

Foil bracket modifications include material changes (aluminum was replaced with titanium); machining to a flatness specification; and polishing to prevent sharp points that can lead to vacuum breakdown, and also to maximize the electrical contact between the stripper foil and the bracket. The foils were also moved 1 cm further out on the bracket arm to prevent the convoy electrons from hitting the bracket during their path down to the electron catcher at the bottom of the vacuum chamber. Additionally, excess material was removed on the arm and leg of the bracket to minimize the probability that reflected convoy electrons would strike the bracket (the original intent of the long arm and leg was to allow for fiber-supported foils, but the diamond foils do not require fiber support). The original and the new foil brackets are shown in Figure 4-6.

a)

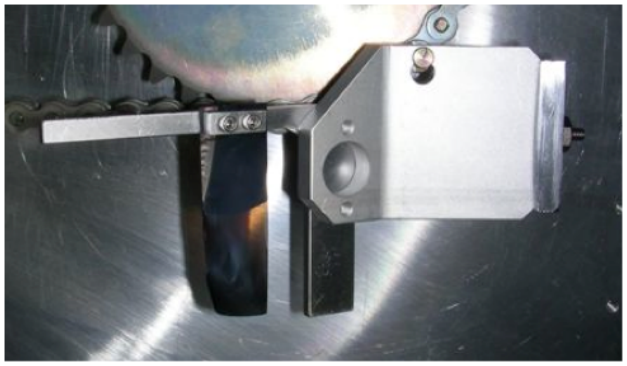

b)

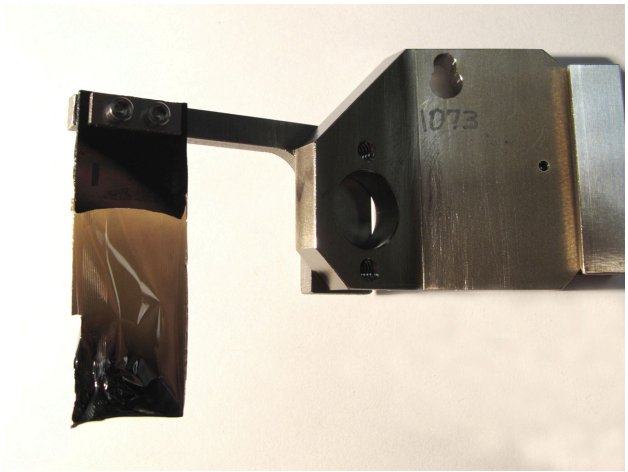

Figure. 4-6. a) A first generation foil bracket mounted on the foil-changer mechanism. The long arm and leg of the L-shaped bracket are designed to stretch carbon fibers across the span to support foils if needed (not used in this case). b) Used foil and bracket that lasted the entire Sept. – Dec. 2009 run cycle at high beam power (reproduced from Ref. [51])

4.4 EXTRACTION SYSTEM

Extraction from the SNS ring is initiated by simultaneously firing a bank of 14 magnetic extraction kickers. In practice, one of the kickers is kept off to use it as a ready spare for when one of the other kickers fails. The beam is deflected down into a Lambertson septum magnet, reaching a displacement of 169 mm and angle of 13.1 mrad at the entrance to the magnet. The septum magnet primarily deflects the beam to the left, but since it is rolled 0.0451 mrad, it also changes the incoming downward angle to a slight upward angle of 0.58 mrad. The first quadrupole magnet in the RTBT extraction line is vertically offset to cancel this upward angle and bring the extracted beam onto the elevation of the extraction beam line (182.6 mm below the elevation of the circulating beam). In February 2009, based on beam measurements, the elevation of this quadrupole magnet was adjusted from its original design specification of 1.9 mm below the beam line elevation to 3.4 mm below the beam line, to improve the launch of the extracted beam into the RTBT.

The first BPM in the RTBT is 27 m downstream of the septum magnet, so it is difficult to empirically determine the optimum setpoints for the 14 extraction kickers. To date kicker magnets are set manually,

but the resultant trajectory still shows several mm of displacement at the BPMs. However, the beam loss is low and the dipole correctors are capable of correcting the beam trajectory in the RTBT.

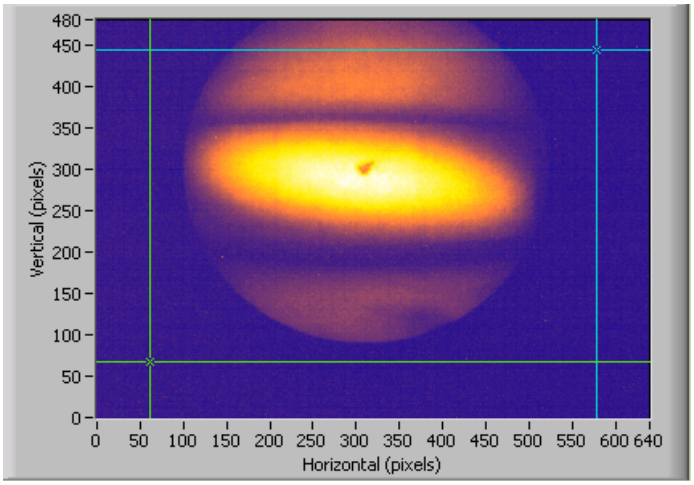

Figure 4-7. An example of a beam image from the temporary view screen that was mounted to the face of the spallation target during the early stages of commissioning. Reproduced from Ref. [47]

During the early stages of ring commissioning, when a temporary view screen was installed on the front face of the mercury spallation target, a clearly tilted beam image was evident on the target as shown in Figure 4-7. More evidence for a tilted beam was observed later, during studies where the injection kickers were varied to paint hollow beams of various sizes. The wire scanner profile monitors in the RTBT extraction line showed unexpected results, such as those shown in Figure 4-8. In this figure the horizontal injection kickers were set to three different amplitudes, which ideally would paint hollow beams with three different horizontal beam sizes, with no change in the vertical beam profiles. The horizontal profiles were close to the expected shapes, but the vertical profiles showed shapes that were sometimes peaked rather than hollow.

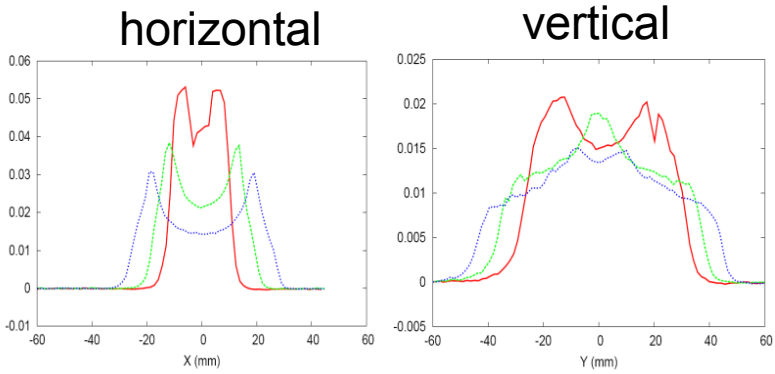

Fig. 4-8. Beam profiles from a wire scanner (WS20) in the RTBT extraction line, for three different horizontal injection kicker settings, indicating coupling to the vertical plane. Reproduced from Ref. [49].

The final and most direct evidence of tilt came after developing a technique [52] to recreate two dimensional real-space beam distributions at any beam position monitor in the extraction line. Single mini-pulses (i.e. one turn injection) are injected into the ring, the extraction time is varied, and the beam

position for each extraction time is recorded. To the extent that an accumulated beam distribution is just a collection of individual beamlets from the individual injected turns (valid for non-decohering beams in the absence of space charge and other collective effects), a fairly accurate measurement of the beam distributions is achievable, such as the one shown in Figure. 4-9a, which clearly indicates a beam tilt.

Based on these observations, the source of the tilted beam was eventually traced to a large skew quad component in the extraction path of the Lambertson septum magnet. Subsequent 3-D magnet modeling simulations [53] showed that the skew component is in fact quite large, and multi-particle tracking simulations incorporating the magnet model skew quad component gave good agreement with observations. The magnet simulations showed that the skew quad component could be greatly reduced by modifying the magnet shims, and this was done in February 2009. Subsequent beam measurements showed that the cross plane coupling has been reduced to below measurable values. An example beam distribution, taken after the shim replacement, is shown in Figure 4-9b.

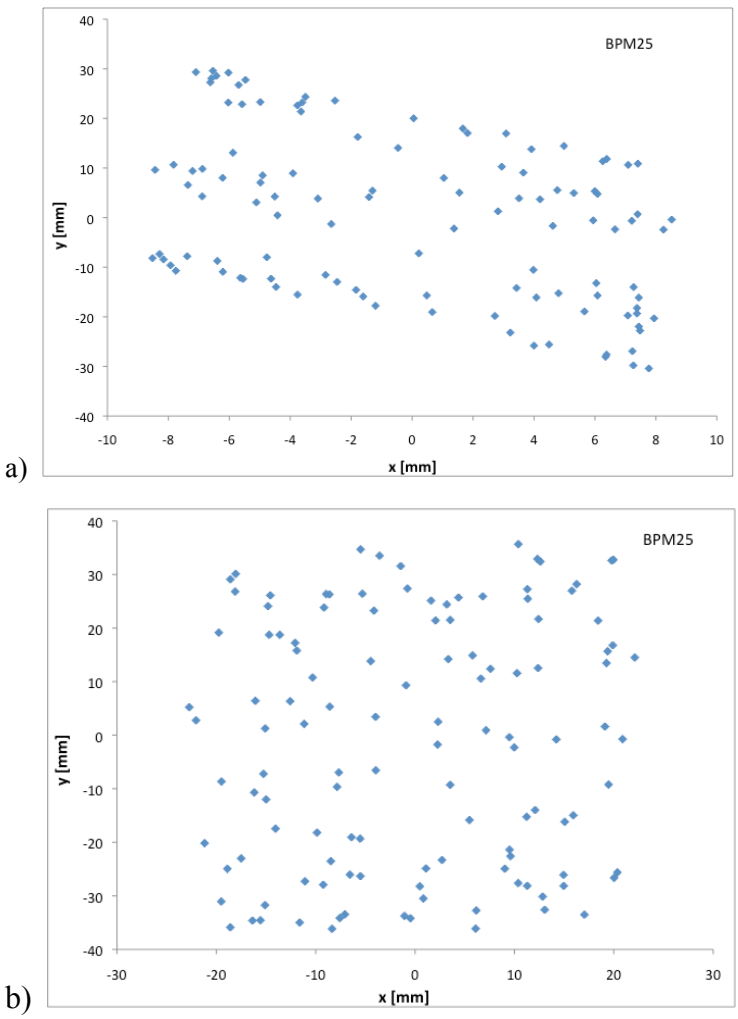

Figure. 4-9. Reconstructed beam distributions at a BPM (BPM25) in the RTBT extraction line a) indicating tilt, before Lambertson septum modifications and b) with no tilt after modifying the extraction septum magnet shims.

4.5 RF SYSTEM PERFORMANCE

The high power portions of the RF system performed well from first operation [54]. The gap voltage calibrations were verified and bunching was demonstrated in January 2006. The ring RF system operated with a single cavity for the initial low power operation period. During subsequent machine development the beam intensity was slowly increased and the Low Level RF system (LLRF) was found to be limited in dynamic range to control only about $5x10^{13}$ protons per pulse. Removing some attenuation (10 dB) between the LLRF output and power amplifier provided the necessary dynamic range to allow operation at the present maximum intensity of $1.55x10^{14}$ protons per pulse. Figure 4-10 shows a display of the cavity voltage and phase with respect to the beam for $9.6x10^{13}$ protons per pulse. While a small beam-loading effect is visible in the amplitude trace, at about 500 volts, it should be noted that no particular effort went into adjusting the LLRF system to minimize this effect. The transient occurring at the extraction time in this trace (near turn 3700) can be controlled by removing the RF drive at extraction.

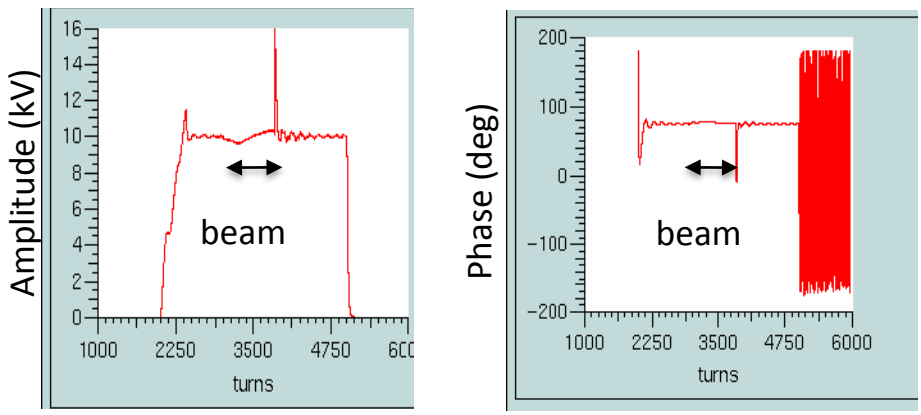

Figure 4-10: Amplitude and Phase waveform for a ~ 1 msec beam pulse with $9.6x10^{13}$ protons per pulse.

The system design included a cavity dynamic tuning capability to compensate for the significant effect of cavity detuning by the beam current at high intensity. A 180 Hz sinusoidal current, programmable in amplitude and phase, is supplied to the cavity tuning conductors. The roughly linear portion of the sinusoidal current is phased to counteract the linear ramp-up of beam current thus holding the cavity nearly on resonance. This approach reduces the final amplifier drive current, thus easing the requirements on the LLRF dynamic range. The effect of cavity dynamic tuning of the RF field phase with beam is shown in Figure 4-11 for a case with about $1.6x10^{13}$ accumulated protons. The 180 Hz sinusoidal dynamic tuning current has a peak-to-peak amplitude of 90 amperes to compensate for beam loading and is offset by 260 amperes to set the cavity at the nominal operating frequency. The upper trace displays the phase between the final amplifier grid and anode before adjusting the dynamic tuning. One can clearly see the phase shift resulting from beam being injected into the ring (T2 to T3). The lower trace has the dynamic tuning current adjusted to minimize phase shift during the injection period (T2 to T3). Note that the phase is shifting prior to beam injection (T1 to T2) and again during a short store time (T3 to T4). At extraction time (T4) an abrupt phase shift is seen as beam is extracted from the ring.

The LLRF system design also included the ability to compensate for beam loading by sampling the beam current, inverting this signal with respect to the beam current, and feeding it into the amplifier chain to cancel the beam loading effects. However, this was never implemented and there are no plans to do so.

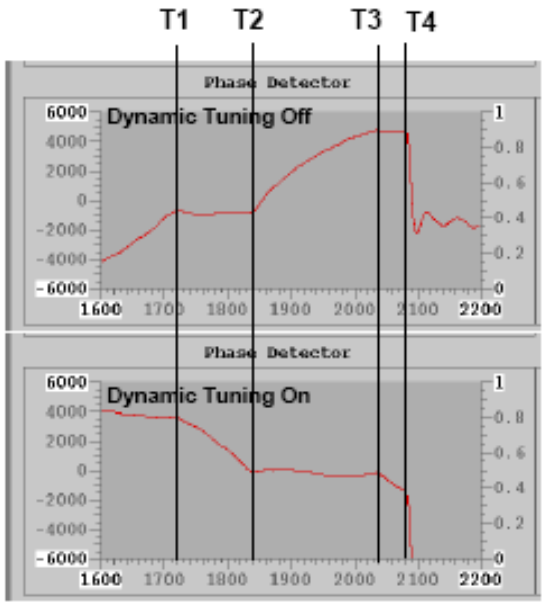

Figure 4-11. Phase between the grid and anode of the final ring RF amplifier stage with and without cavity dynamic tuning. Beam injection is from T2 to T3, and beam storage is T3 to T4. The vertical axis is the phase difference, in arbitrary units.

4.6 COLLIMATION SYSTEM PERFORMANCE

The ring collimation system is a two-stage system composed of a set of adjustable primary scrapers for scattering the beam to high emittance, and an array of three large secondary collimators for absorbing the projected beam.

The three large, fixed aperture collimators are the limiting aperture in the ring and are responsible for intercepting particles that stray outside of the transverse machine acceptance. Even for low intensity or small emittance beams, mechanisms such as foil scattering at injection, or poor extraction into the RTBT, send a portion of the beam outside the transverse acceptance and into the collimation system. Additionally, the collimators become the main loss point when the painted beam size is too large or when there is an equipment failure or beam instability. Thus, although the SNS accumulator ring is not yet routinely operated at its full design intensity, the collimation system has been in use since the first day of commissioning.

During regular beam operations, it has become customary operate the collimation system as a single stage system, with the primary scrapers fully retracted and the high emittance beam intercepted directly by the secondary collimators. Though simulations indicate lower efficiency collimation, operation in this mode has proved adequate for the current beam configuration. There has not yet been sufficient beam loss in other areas of the ring to necessitate inserting the primary scrapers to preemptively remove beam halo.

In anticipation of the need to use the collimation system for removing halo beam in the future high intensity ring operations, a few dedicated collimation experiments have been performed [55]. The main thrust of the experiments was two-fold: 1) To characterize and compare the loss pattern for single-stage and two-stage collimation, and 2) to benchmark experimental data against these simulations.

One method for studying collimation system behavior is through the use of single-mini-pulse beam experiments, whereby a single, 690 ns beam pulse is injected into the ring and sent to the collimation

system in various fashions. With the use of a single mini-pulse of beam, a known amount of beam power is deposited into the collimation system without violating any loss limits.

In one set of experiments the scraper insertion is varied from a position near the beam pipe center to a position just inside of the collimator aperture. Then the injection kickers are adjusted, and thus the corresponding mini-pulse oscillation amplitude, until the scrapers intercept the mini-pulse. This method is analogous to measuring the two-stage collimation loss pattern for a variety of beam emittances. The loss distribution for multiple radial scraper settings on the vertical (90°) scraper is shown in Figure 4 -12. The plot shows that the loss distribution for the two-stage system is insensitive to the emittance of the beam being scraped. Additionally, the peaks of the loss pattern occur at Beam Loss Monitors (BLM)s situated near the collimators. It should be noted that some of the BLMs in this region are detecting higher shielded losses than other BLMs. Because of the variations in BLM locations, as well as the fact that some BLMs detect losses both from shielded and unshielded elements, a true quantitative measurement of collimation efficiency is difficult to attain.

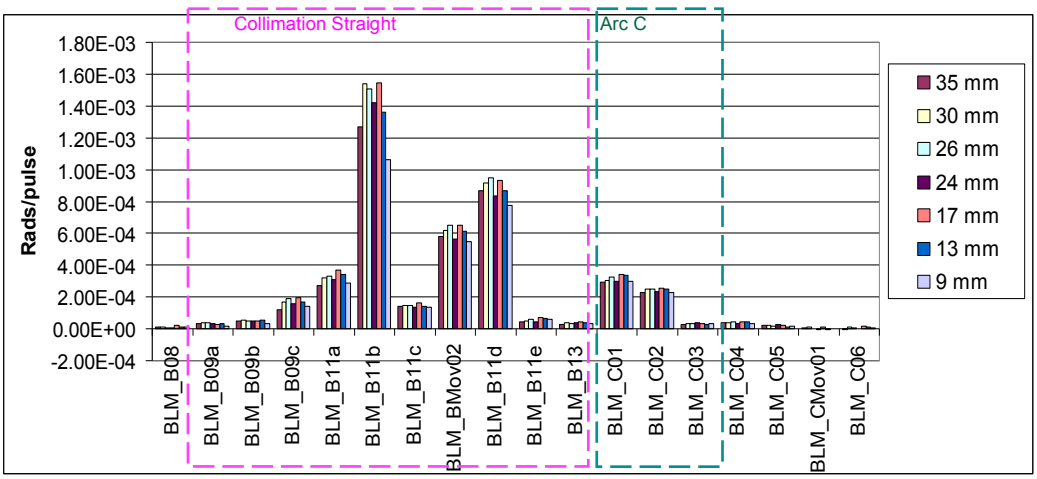

Figure 4-12. Comparison of the beam loss pattern in the collimation straight and downstream arc for a minipulse of beam collimated at different scraper positions. Arc C is directly downstream if the collimators. Reproduced from Ref. [55].

Two areas of beam loss outside of the collimator system that are also high are BLM B11b, which resides near a quadrupole doublet between the primary and secondary collimators, and BLMs C01 and 02, which detect losses after the secondary collimation (in the downstream Arc C). Both of these loss points represent collimation inefficiency.

The remaining portion of the ring outside of the collimation straight and the first portion of the downstream arc is not shown in Figure 4-12 because very little collimation-induced loss is observed there. This illustrates a key feature of the collimation system – its ability to localize the beam loss within one area the machine, such that the remainder of the machine can stay below the 1 W/m limit.

In another experiment performed to test the loss distribution for single-stage collimation, the scrapers were retracted all the way and the single mini-pulse amplitude was adjusted until it intercepted the secondary collimators. Figure 4-13 shows the resulting loss distribution, along with the two-stage loss distribution for comparison. A significant difference between the two loss patterns is evident, with the single-stage system having a higher proportion of losses towards the end of the collimation straight, and in the downstream arc. The two-stage system clearly does a better job of containing the losses to the collimation straight.

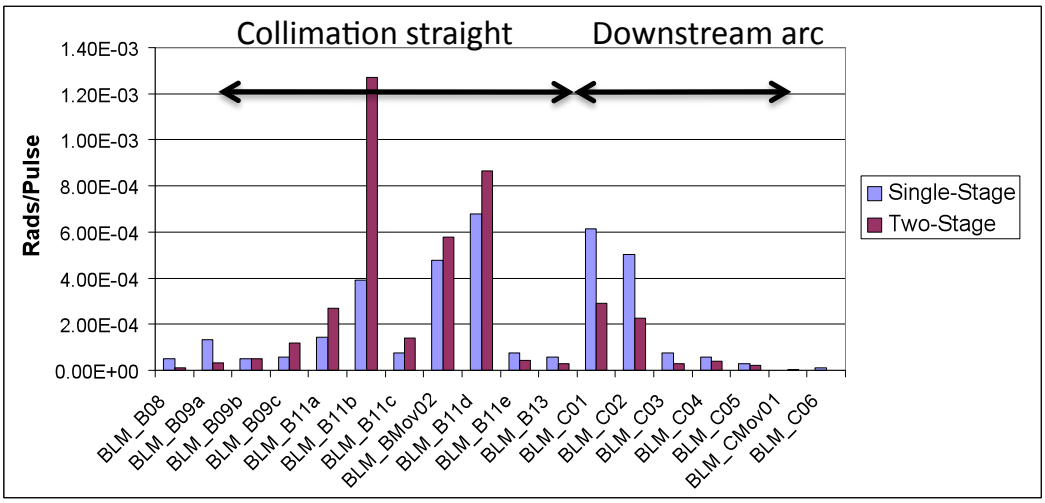

Figure 4-13. Beam loss pattern comparison in the collimation straight and downstream arc for a mini-pulse of beam collimated in a single-stage (blue) versus a two-stage (red) fashion. Reproduced from Ref. [55].

It is worthwhile to note that the since the scrapers enclose only one-half of the beam aperture, first-turn particle loss mechanisms such as foil scattering can lead to single-stage collimation even when the scrapers are inserted. Thus, there will be a certain amount of single stage collimation inefficiency even when the two-stage system is in use. Evidence for this can be seen in collimation experiments where different amounts of a fully-painted beam distribution are collimated with a two-stage system. Figure 4-14 shows one such experiment, where 150 turns of beam were accumulated and the loss distribution was recorded for different scraper settings, i.e., different amounts of beam collimation. Note that the majority of the beam loss in the arc is present before the scrapers are inserted, and that it does not increase in proportion to the rest of the collimation losses when the scrapers are brought in further. Thus, the actual two-stage collimation efficiency is likely higher than what one might assume from experiments such as the one shown in Figure 4-12. Two-stage collimation is most effective when the beam grows slowly on a turn-by-turn basis, which guarantees the beam will intercept the scrapers before the secondary collimators.

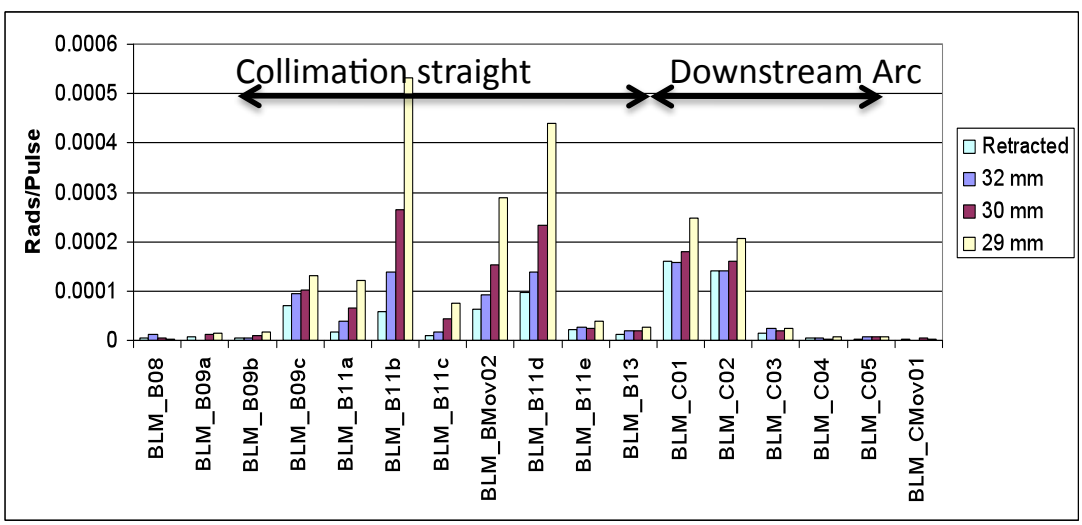

Figure 4-14. Comparison of the beam loss patterns for 150-turn accumulation and various scraper positions.

4.7 HIGH INTENSITY INSTABILITY AND COLLECTIVE EFFECTS

One of the biggest uncertainties in high power operation of the SNS ring is the e-p instability threshold. Initial instability measurements in February and November 2006 did not reveal any instabilities at normal operating conditions up to a bunched beam intensity of 9.6×10^{13} ppp stored for 1100 turns (the nominal full-power intensity is 1.5×10^{14} ppp and the nominal storage time is 2 turns). Subsequent measurements showed no significant instabilities up to 1.2×10^{14} ppp (which corresponds to 1 MW average beam power). Figure 4-15 shows the Ring beam current monitor for one of the 9.6×10^{13} ppp accumulation cycles.

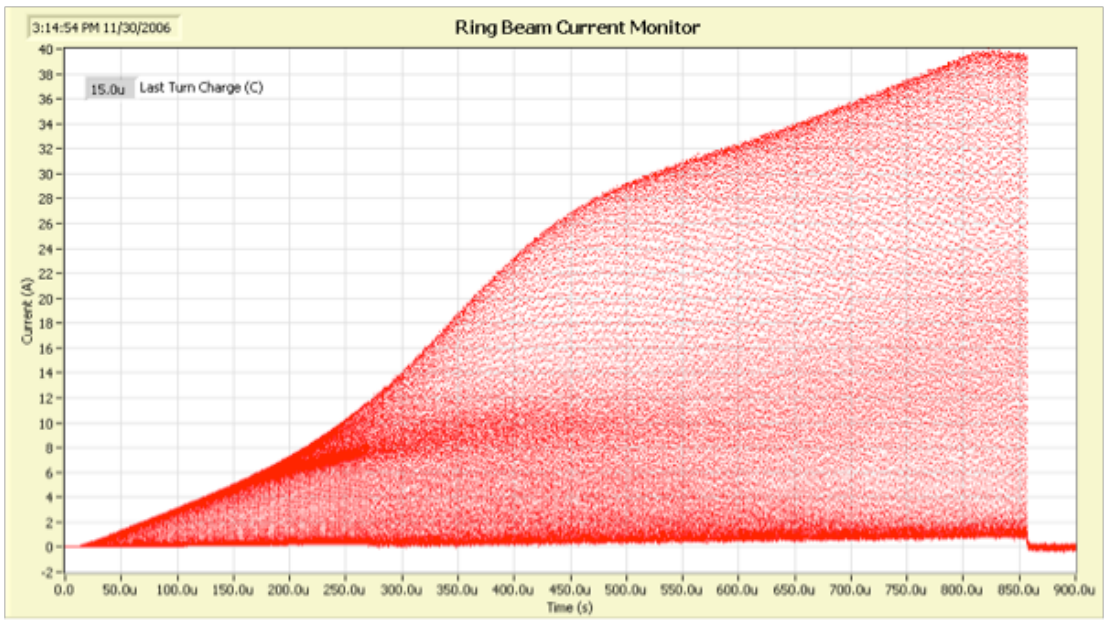

Fig. 4-15. Ring beam current monitor showing accumulation of 9.6×10^{13} ppp. Reproduced from Ref. [47].

However, three different instabilities were observed [56] after turning off the rf bunchers in the ring. The beam energy during the experiments was in the range of 890 – 931 MeV, depending on the state of the linear accelerator during the coincident beam run, and the lattice tune, chopping condition, RF state, chromaticity, and beam intensity were varied.

The first instability, with characteristics consistent with e-p instability, was observed after storing 4, 8, and 16 μC of beam charge for several milliseconds. The instability was present at all three beam charge values. The second instability, an impedance-driven instability due to the extraction kickers, was observed after storing 3, 6, and 12 uC of beam charge for several milliseconds. This instability was also present at all three beam charge values. Both instabilities are sometimes present at the same time, as shown in Figure 4-16. The third instability was observed after lowering the betatron tune to slightly below the integer ($Q_x \approx Q_y \approx 5.8$) to create conditions favorable for the resistive wall instability. The frequency of this instability is about 191 kHz, as expected, with a growth rate (1.2 msec for 6 μC beam charge) consistent with previous estimates of the impedance of the injection kickers together with the vacuum pipes. The first e-p instabilities were seen for the case of a coasting beam configuration with no RF, i.e., the beam was unchopped and filled the entire ring. Most of the e-p instability measurements were made for this configuration. An e-p instability was also noted for the case where the beam was chopped to the nominal 695 ns pulse length, and with the RF turned off (although in this case there was some self-bunching due to beam excitation of the cavities). The characteristics of the instability for the chopped beam scenario are distinguishable from the coasting beam scenario, and as discussed below.

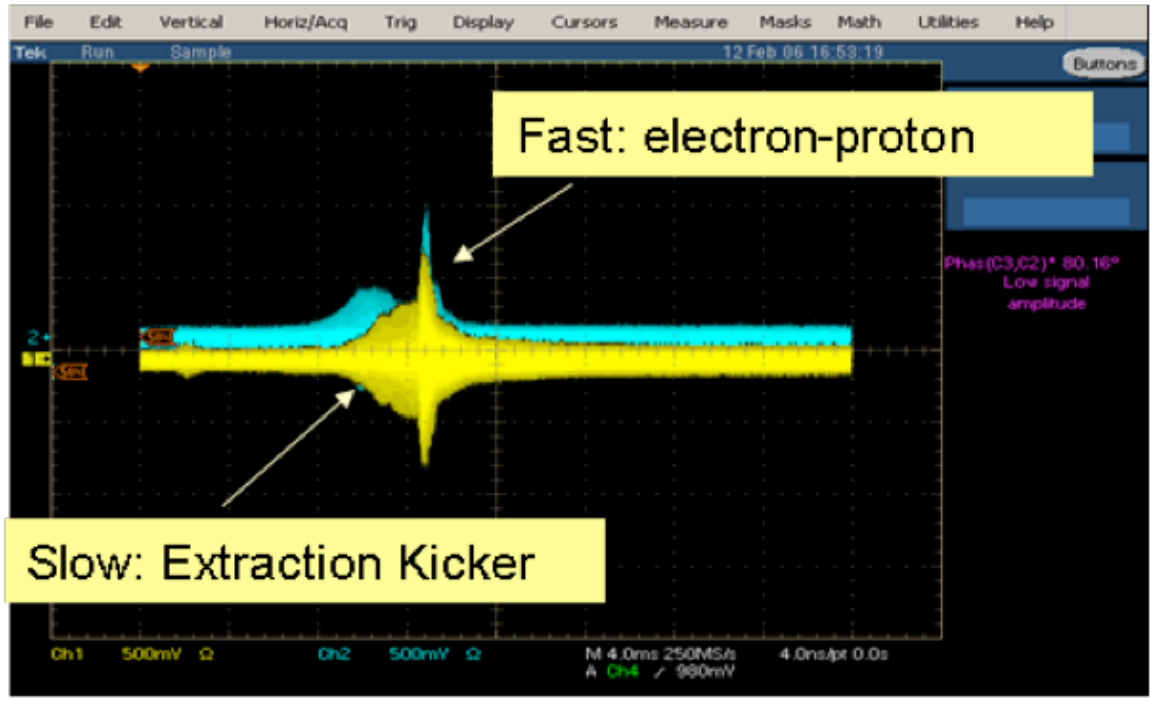

Fig. 4-16. Horizontal (yellow) and vertical (blue) BPM difference signals (arbitrary units) observed after storing the beam for several milliseconds. Two different instabilities are simultaneously present for this shot. Figure reproduced from Ref. [56].

4.7.1 Coasting Beam Case

The analysis of the coasting beam data is presented in detail in references [56,57]. The lowest intensity for which the e-p instability occurred in the coasting beam configuration was 2×10^{13} ppp. All instabilities were observed for the ring lattice set for zero chromaticity, and no instabilities were present for the natural chromaticity lattice. However, the chromaticity was not scanned between zero and natural during the high intensity experiments, so it is unknown to what extent instability would exist in this range.

The instability was marked by an exponential increase in the position oscillations measured by the BPMs, with frequencies in the range of tens of MHz. An intensity scan of the instability over the range of 2×10^{13} – 1.0×10^{14} ppp showed that the rise time of the instability varied between ~1000 turns on the low intensity end, and ~30 turns on the high intensity end, with a frequencies that became progressively more localized around 80 MHz at the higher intensity.

The instability was present in both planes, with the vertical plane being somewhat larger. Analysis of the instability data revealed coupling between the two planes, with the betatron tune for both planes being present in the BPM signal for a given plane. Variation of the lattice tune showed little effect on the instability.

4.7.2 Chopped Beam Case

The chopped beam instability was observed during an RF development beam study, where the beam intensity was 8.2×10^{13} ppp. During this study, the RF was turned off, and the e-p instability was observed. Though the beam was chopped, since the RF was off, the beam gap was at least partially filled before the

onset of the instability. The instability was seen in both planes, but BPM data was only recorded for off-line analysis in the vertical plane.

An example vertical BPM difference signal for the instability is shown in Figure 4-17. The onset of the instability was near the end of the 850-turn accumulation of the 9.5×10^{13} ppp chopped beam. The integration of a single BPM electrode is insightful for understanding the longitudinal location of the instability of the beam. Figure 4-18 shows the integrated electrode signal at three different points in the beam accumulation and storage; this plot is intended only to show the longitudinal location of the instability, and not to provide any quantitative measure of the oscillation. As seen, the longitudinal location of the initial instability was on the flat-top of the beam profile, not far behind the leading edge of the beam. As the instability strengthened, the centroid oscillation began to expand towards the tail of the beam.

The frequency content of the instability is shown as a function of turn number in Figure 4-19. The frequency spectrum is broad and spans a range of roughly 20 to 90 MHz. The onset of the instability begins around 50 MHz, and then becomes broader as the beam is stored. Distinct bands of frequency excitation can be observed in the spectrum, and the bands seem to individually drift downward in frequency as the beam is stored and the instability progresses. For instance, the frequency band beginning at 50 MHz drifts down to approximately 30 MHz in about 250 turns. Simultaneously, other isolated bands of activity develop at higher frequency and drift downward with turns at the same rate. The physical phenomenon responsible for the downward drift is not yet known, but we speculate that one possibility is that the beam density decreases due to transverse and longitudinal beam growth. However, no investigations have yet been conducted to confirm this possibility. The e-p instabilities observed for the coasting beam case showed a peak frequency around 80 MHz.

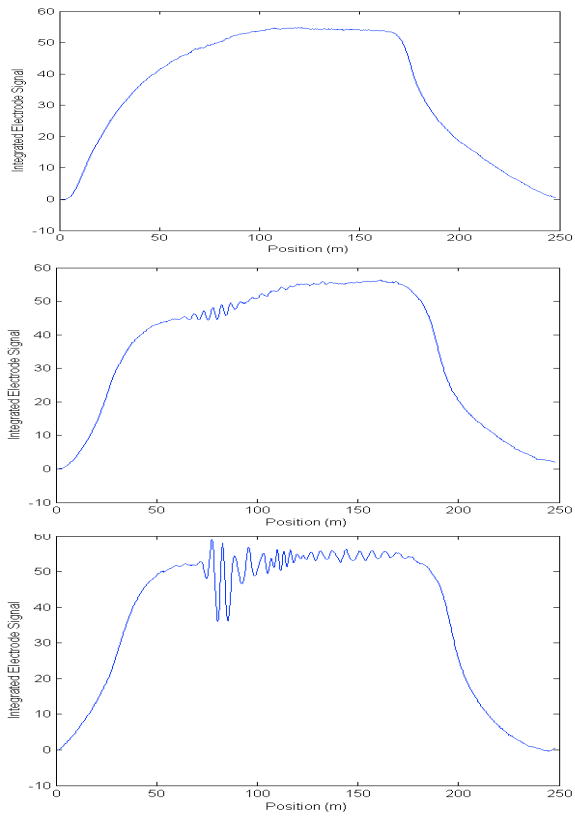

Figure 4-18. The integrated signal for a vertical BPM electrode. The top plot is one turn of beam just before the onset of the instability, the middle is one turn of beam near the onset of the instability, and the last plot is one turn of beam at the first peak of instability (corresponding to about 850 *u*s in Figure 4-17). The head of the beam is on the left side of the plots. Figure reproduced from Ref. [47].

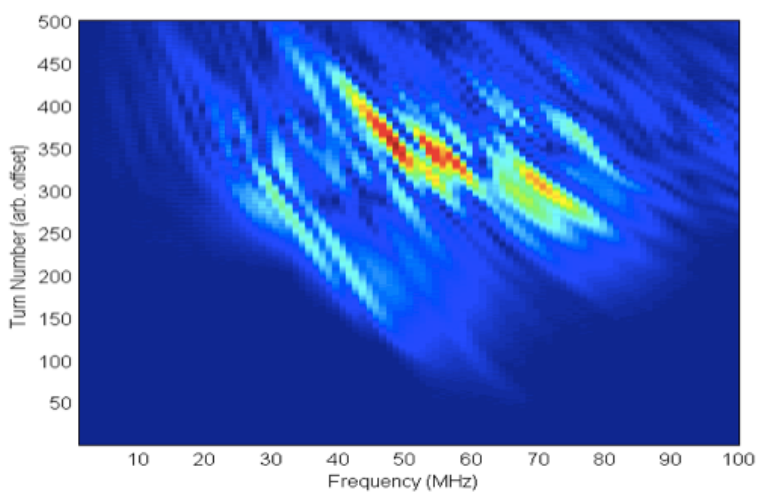

Figure 4-19. Turn-by-turn evolution of the frequency content of a BPM difference signal. Figure reproduced from Ref. [57].

5. TRANSPORT LINES

5.1 HIGH ENERGY BEAM TRANSPORT (HEBT)

The first portion of the HEBT was commissioned as part of the linac commissioning since it was needed to transport the beam to the linac beam dump. During the linac commissioning the beam line performed well and there were no problems. The remainder of the HEBT was commissioned in January 2006. Beam was transported through the HEBT to the ring injection section on the first shot. The arc quadrupole magnets were easily adjusted to achieve a good achromat through the arc, and no adjustment has since been needed.

The collimator systems in the HEBT were initially not used at low beam power, but today, during a typical 1 MW production run, the two transverse collimators are routinely used. They primarily affect the loss in the injection dump beam line, where we are most sensitive to beam halos [58]. Each of the two transverse collimators has a left-right pair and a top-bottom pair of scrapers. The left-right (top-bottom) pair is located near a maximum in the horizontal (vertical) betatron function of the FODO lattice. Due to this arrangement, the collimator system can only be optimized for one plane, and at SNS it is the vertical scrapers that are located closest to the collimators and are the most efficient. The left-right scrapers inefficiency tends to create beam loss in the vicinity of the beginning of the 90-degree arc in the HEBT transport line. However, even though the collimators are each rated for 2 kW of beam power, they typically intercept less than a few hundred watts, and the resultant activation is acceptable.

The momentum collimator system failed in April 2008, when a pump in the momentum dump water cooling system failed, due to a concurrent pressure and temperature excursion. A post- mortem analysis showed that the over pressurization was caused by a combination of excessive beam power and the inability to effectively vent the gases created by radiolysis, and a blockage in the return water-cooling pipe. After discovering the radiolysis gas issue the momentum dump was removed from service since radiolysis is a problem at any beam power. The momentum dump has been re-designed and it is now cooled by re-circulated air. Re-commissioning is scheduled for the fall of 2010.

5.2 RING TARGET BEAM TRANSPORT (RTBT)

The first part of the RTBT, up to the extraction dump, was commissioned in January 2006 during ring commissioning. The latter part of the beam line was commissioned in April 2006 as part of the initial target commissioning. The beam line performed well except for some transverse beam coupling that was introduced by a skew quadrupole component in the ring extraction Lambertson septum magnet (see ring extraction discussion above).

6. TARGET INTERFACE

The beam delivery system upstream of the target consists of four 36-cm aperture quadrupole magnets with rad-hard coils; two dual-plane, rad-hard steering magnets each capable of up to 1.5-mrad beam deflection; and the proton beam vacuum window, which consists of two 2-mm thick, water cooled, semi-cylindrical Inconel sheets. The last quadrupole is 11.59 m upstream of the target face, and the last steering magnet is 1-m downstream of this quadrupole.

As the beam passes through the proton beam window, the resultant multiple scattering adds a large contribution to the beam divergence. However, the window is close enough to the target that the additional angular divergence does not strongly affect the beam size at the target (the rms beam size increases by 2 to 4 mm). Of course some of the scattering interactions result in large deflection angles, which cause 3-4% of the beam to be lost in the beam flight tube between the window and the target.

6.1 REQUIREMENTS

The beam parameters at the Spallation Neutron Source (SNS) target must be maintained within strict limits. At the nominal beam power of 1.44 MW, the beam position must be kept within 4 mm of the vertical target center and 6 mm of the horizontal center, 90% of the beam must be within the nominal 70 mm x 200 mm spot size, and the peak beam current density must be kept below 0.18 A/m^2. At MW beam power levels, intercepting beam diagnostics will not survive very long. An additional complication is that most of the beam diagnostics are more than 9 m upstream of the target due to space constraints.

6.2 BEAM DIAGNOSTICS

The baseline set of beam diagnostics originally included an insertable harp, beam position monitors (BPMs), and wire scanners, as shown in Figure 6-1 and Table 6-1. During the last stages of equipment fabrication additional diagnostics were added to the design: a thermocouple-based halo monitor about 2-m upstream of the target, and an additional BPM just downstream of the harp.

Table 6-1 Beam diagnostic positions in the RTBT line approach to the target

Diagnostic	Distance from target face (m)
Halo monitor	2.14
Last 3 BPMs	9.25, 12.76, 19.27
Harp	9.52
Wire scanners	33 to 56

An emittance station, comprising four wire scanners located between 33 and 56 m upstream of the target, provides a measurement of the rms emittance and Twiss-parameters of the beam entering the final portion of the beam line upstream of the target. The harp is the closest profile monitor to the target. It consists of three signal wire planes (horizontal, vertical, and diagonal), and is designed to also provide a position measurement with an absolute accuracy of ±2 mm. It can also be included in the emittance and Twiss parameter measurements. Due to the intense proton beam, the harp signal wires were not expected

to survive more than a few months at full beam power if they are continuously left in the beam. The harp is therefore designed to be insertable. However, due to issues with the retraction mechanism, it has been left inserted in the beam continuously to date with no problems.

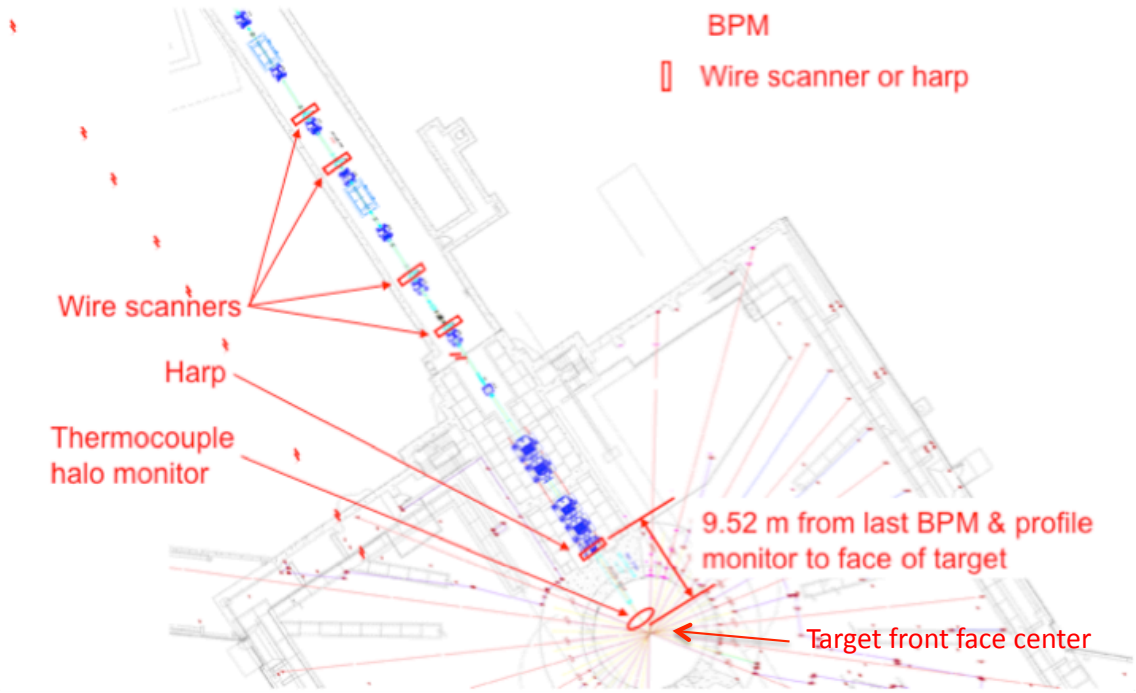

Figure 6-1. Layout of the beam line and beam diagnostics leading up to the target.

The last and most-downstream beam diagnostic is the thermocouple halo monitor. The first generation halo monitor comprised thermocouples inserted into the top, bottom, left, and right edges of the beam; and the second generation added four more locations along the top and bottom edges. At each thermocouple location there are two thermocouples inserted at slightly different depths into the beam for added reliability and to optimize the measurement for a range of beam sizes. The top and bottom thermocouple probes are 4.2 and 3.75 cm from beam center, and the left and right probes are 11.0 and 11.4 cm from beam center. The halo monitor is designed to center the beam with an absolute accuracy of better than ±2 mm.

For initial target commissioning in April 2006, a temporary view screen was mounted immediately upstream of the target to verify our ability to extrapolate and control the beam parameters at the target. The light from the Cr-doped Al_2O_3 screen was collected by a lens on the end of a fiber optic bundle that extended downstream along the length of the target to a camera 9-m away. An example image is shown in Figure. 4-7.

A new view screen system is being commissioned. It employs a chromium-doped Al_2O_3 composition that is sprayed directly onto the surface of the target [59]. Once this system is fully commissioned it will become the primary measurement of beam position, beam size, and beam density on the target.

6.3 BEAM ON TARGET RESULTS

6.3.1 Centering

The thermocouple halo monitor, 2.14-m upstream of the target face, provides the most accurate and most direct measurement of beam position at the target. The final beam position at the target is empirically adjusted to provide symmetric thermocouple temperature measurements. However, the thermocouples do not respond well until the beam power reaches about 100 kW. At low beam power the best method to center the beam on the target is to use the BPM system. Unfortunately the BPM closest to the target is 9.25 m upstream. Beam measurements made when the view screen was installed on the target nose were used to determine offsets and scale factors to apply to the beam position extrapolated from the BPM system, but the accuracy of this method is only about ±10 mm, which is adequate at beam powers less than <100 kW.

6.3.2 Beam Size and Peak Power Density

Five profile monitors (the last four wire scanners in the emittance station plus the harp) provide the beam profile measurements upstream of the target. An online envelope optics model [41] with a fitting routine calculates the beam Twiss parameters and emittance entering the profile measurement section, and forward propagates the beam to determine the rms beam size at the proton beam window and target. To estimate the final size on the target we add 11 mm in quadrature with the beam size from the model to account for scattering from the proton beam window. This method was successfully benchmarked during commissioning using the temporary view screen. An example beam size determination is shown in Figure 6-2. To estimate the peak beam density at the target and proton beam window the peak density measured on the harp is scaled by the model extrapolated rms beam sizes.

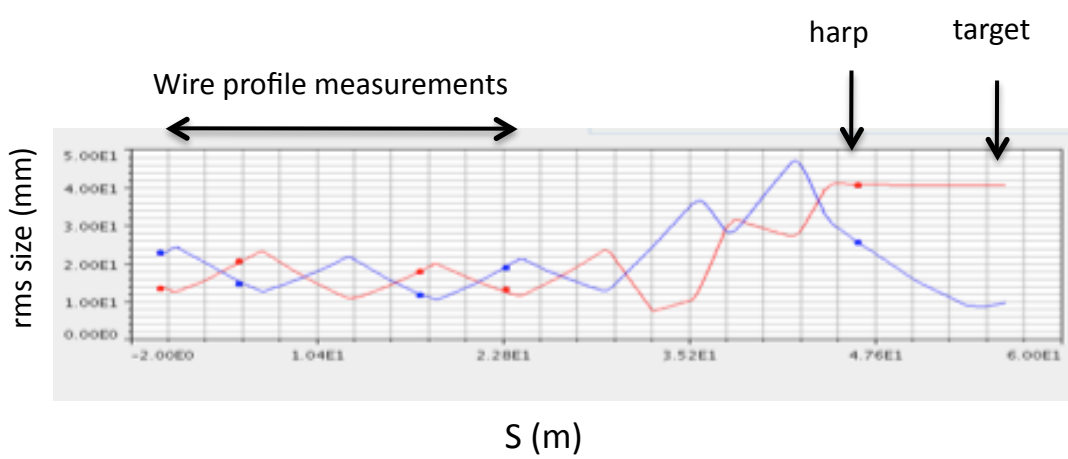

Figure 6.2. Plot of the on-line model fit (lines) to five profile monitors (dots), used to determine the beam size on the target. Blue is the vertical size and red is the horizontal size.

7. SNS COMPLEX OPERATIONS AND PERFORMANCE

7.1 PERFORMANCE PARAMETERS

The SNS accelerator's primary purpose is to provide a steady high intensity neutron source for a neutron scattering facility. In addition to the high power issues discussed above, operating the accelerator at high availability throughout the year is critical for a neutron scattering facility. The long-term operational goals are ~5000 production hours/year at 90% availability (where availability is defined here as the fraction of scheduled neutron production time that the accelerator actually operated). We include the target and cryogenic moderator downtime as part of the availability accounting. This data is shown in Figure 7-1. Over the first four years of operation the total operating hours increased from ~ 3779 to 5310. Initially a significant fraction of the operational time (~45%) was dedicated to accelerator beam studies and startup activities. By the fourth year this fraction dropped to 20%. The increased beam power shown in Section 1 led to a substantial increase in the proton fluence delivered on target over the first four years (more than 20-fold). One of the most challenging areas was the increase in neutron production availability, which rose from 67% to over 85% during the first four years of operation – coincident with the tremendous increase in beam power. Initially there were issues related to the high voltage RF pulsed power supplies, but remediation efforts have significantly alleviated this problem [60]. Also improvements discussed in the Section 2 on the front-end and ion source contributed to the availability increase. The rapid increase in beam power in the initial years allowed for the early identification of technical issues and provided an opportunity for a quick start in reacting to these. Experiences in the initial power ramp up are described in [61,62].

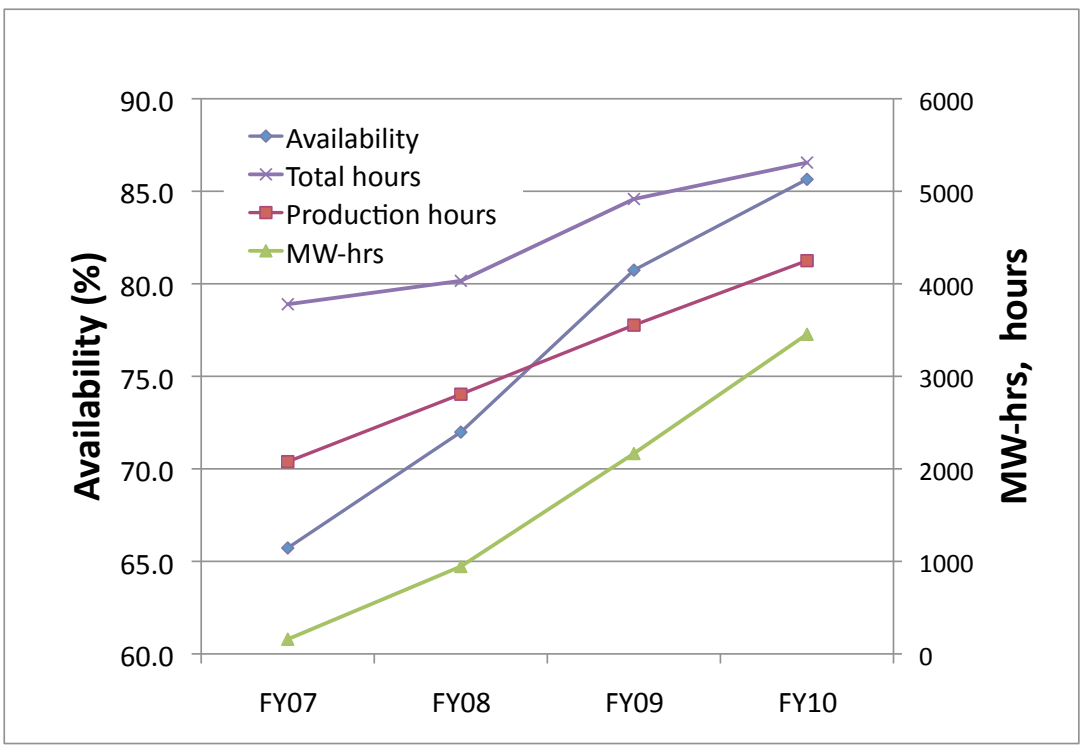

Figure 7-1. Annual performance metrics over the first 4 years of SNS operation: availability during scheduled neutron production, neutron production hours delivered, and MW-hrs of proton beam delivered to the target during production.

7.2 BEAM LOSS AND ACTIVATION

7.2.1 Warm Linac Beam Loss

There is no reduction in beam current along the linac detectable by the beam current monitors. Beam loss monitors (BLMs) based on ionization chambers are used to detect radiation due to beam losses [63]. In addition to protecting against unacceptable residual activation buildup, the BLMs are also used to interrupt beam for machine protection. The machine protection is implemented as a hardware system with~ 20 μs response time, and trip thresholds based on controlled beam spill measurements. The protection against long term residual activation buildup is done with a slower software integration (1 and 10 seconds), and these trip limits are based on empirical comparisons of the measured residual activation after 2-4 week run cycles with the measured beam-loss readings over that period.

Several activation locations found in the warm linac after the first production run came as a surprise because none of the BLMs indicated beam losses. Because BLM chambers were installed at every second quadrupole, and at the CCL energies the radiation pattern is localized within a single quadrupole, BLM sensitivity was insufficient to detect losses at a nearby quadrupoles. The number of ion chambers was doubled to provide full coverage and they were moved closer to the beam line to increase sensitivity. Since implementing these changes there is a good correlation between the BLM response and residual activation measurements taken after production. Figure 7-2 shows the residual activation in the CCL section at various times during the power ramp-up to 1 MW operation. The values are taken at 30 cm, generally 1 day after the end of neutron production. While there is some increase in the activation levels, the increase is not proportional to the power level increase, nor to the increased operational hours during the run cycles as the facility matured.

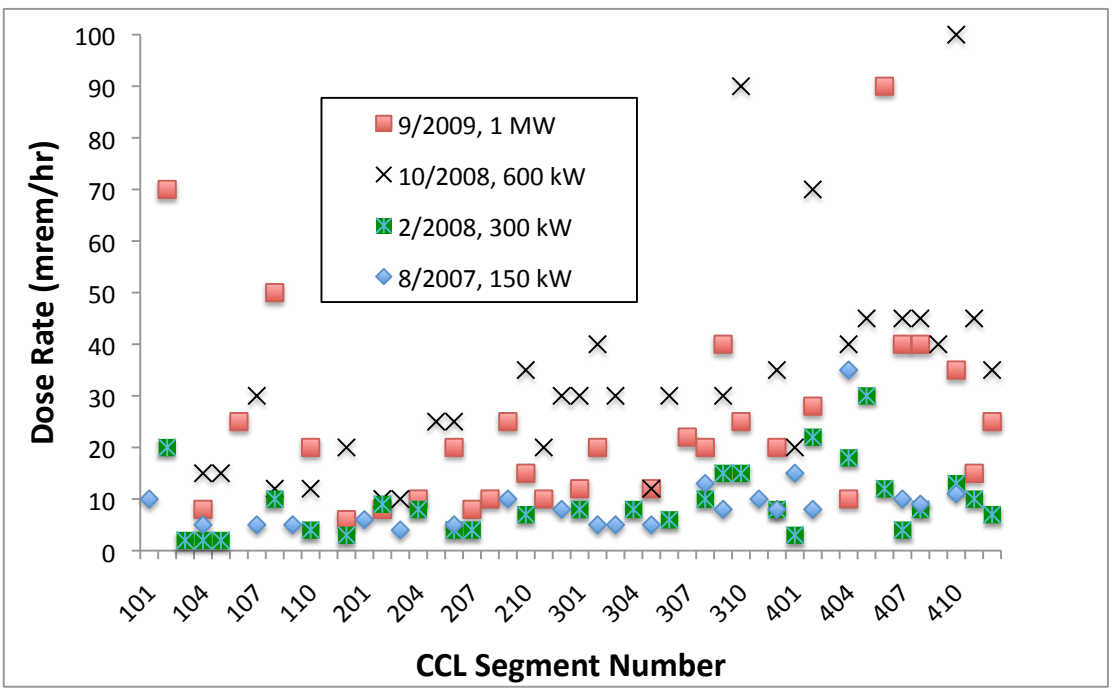

Figure 7-2. Residual activation measurements along the CCL structure taken after ~ at 30 cm, 1 day after neutron production, at various times during the power ramp-up.

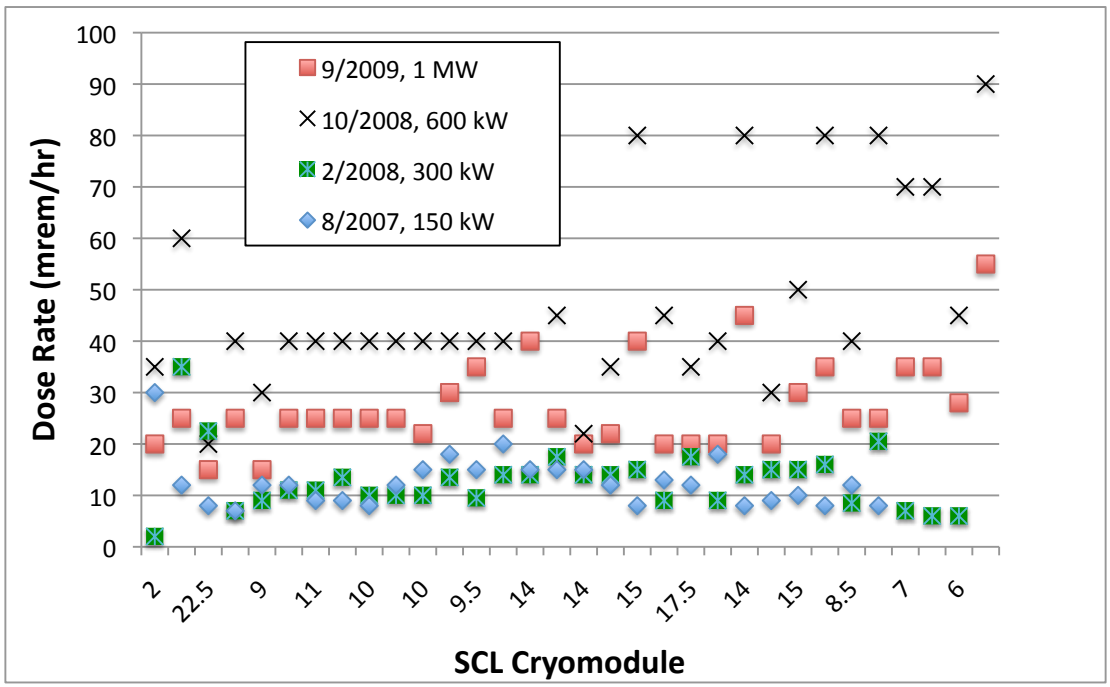

Figure 7-3. Residual activation measurements at 30 cm and ~ 1 day after operations, at various stages during the power ramp-up.

7.2.2 SCL Beam Loss

While beam dynamics simulations predicted no SCL beam loss during the design stage, beam loss is measured between cryomodules, and residual activation is measured following beam operation (beam pipe between the cryomodules is exposed and is the limiting aperture). The absolute ionization chamber BLM response is sensitive to beam energy and the chamber location relative to the beam pipe. However, through experience, it is straightforward to calibrate the measured beam loss and expected residual activation level. Figure 7-3 shows the residual activation levels measured along the SCL (at the warm sections between cryomodules) after operation, during various stages of the power ramp-up. Generally, the activation levels are fairly uniform along the SCL. Initially there was a steady increase in the activation levels with the power ramp-up. In 2008, it was empirically determined that reducing the quadrupole focusing strength resulted in reduced beam loss rates, as shown in Figure 7-4 (we report measured beam loss normalized as Rad/C-transported through the accelerator per pulse). This is reflected in the history of the SCL residual activation buildup throughout the power ramp-up shown in Figure 7-5. Initially the activation levels followed the increased beam charge accelerated through the SCL during each run cycle (also shown in Figure 7-5). The roll-over in the activation buildup in 2008, coincides with the adoption of reduced focusing lattice in the SCL. The reduced focusing lattice includes gradually relaxing quadrupole strengths from nominal at the start of the SCL to about 40% reduced focusing strength at the end of acceleration.

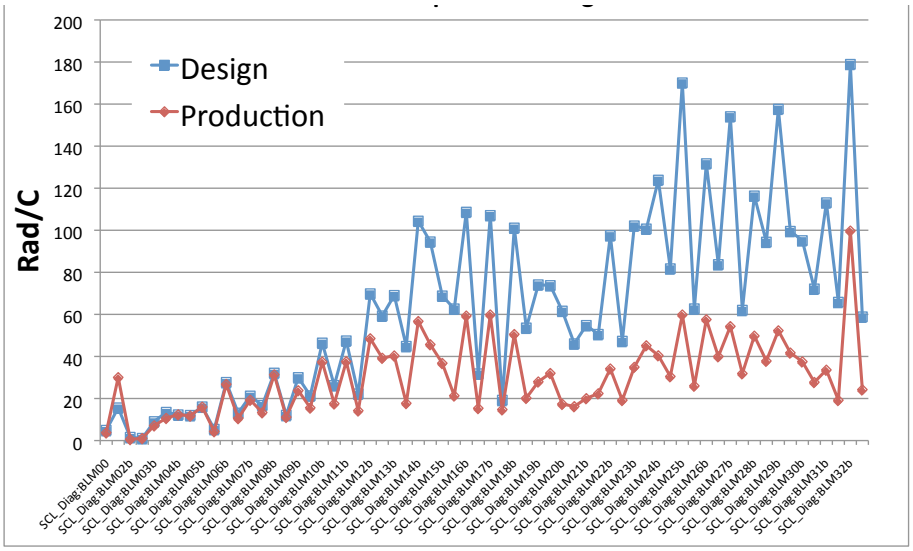

Figure 7-4. Measured beam loss/pulse along the superconducting linac (normalized to the charge/pulse) for the design quadrupole lattice and the reduced focusing lattice used in neutron production.

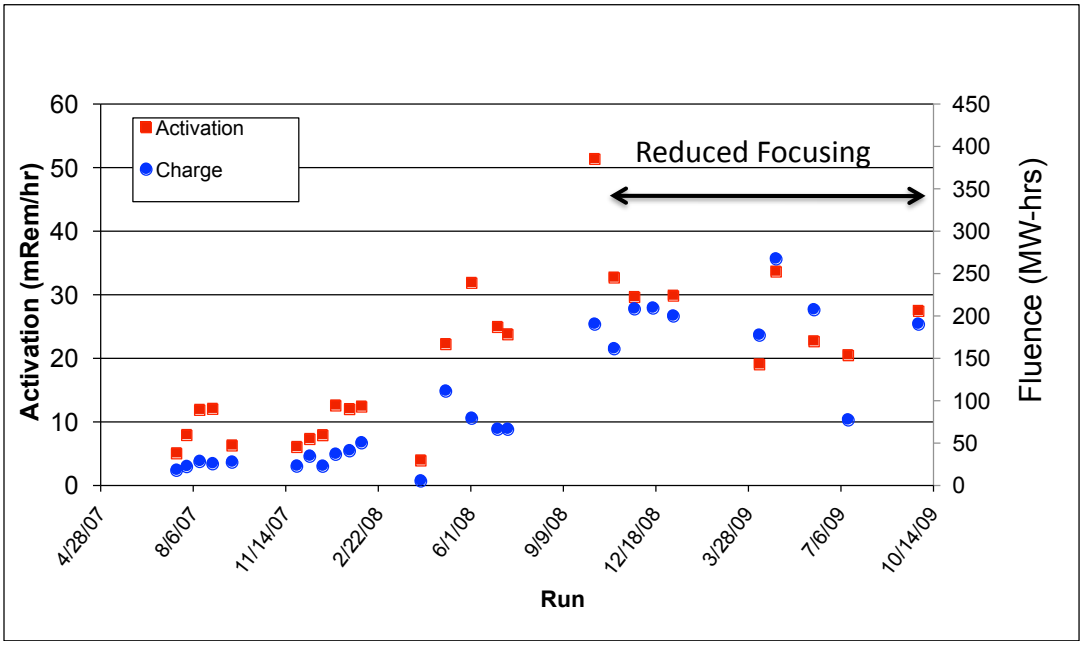

Figure 7-5. History of the average residual activation along the SCL during the power ramp-up (activation levels shown are an average of all SCL inter-cryomodule warm sections)

7.2.3 Ring beam Loss

During the first years of operation the normalized beam loss at the ring injection per Coulomb of beam delivered to the target rapidly decreased as the improvements discussed in Section 4-2 were implemented [64]. Figure 7-6 shows the normalized beam loss around the SNS ring for selected periods

in the power rampup. The high loss points in the ring area are generally in line with our expectations. Beam loss was significantly reduced through improvements in the ring injection, injection dump line and foil areas, as discussed above. The highest beam loss area in the entire accelerator is at the primary stripper foil, due to beam scattering by the foil. The next two highest beam loss points in the ring are just downstream of the secondary stripper foil, and at an aperture reduction in the ring injection straight downstream of the stripper foils (location A13b in Figure 7-7). Other high beam loss points are in the collimation region, as expected, and in the vicinity of the extraction septum magnet. The latter loss is due to beam in the gap, and this loss has been significantly reduced through front-end chopper improvements.

The residual activation in the ring injection area has increased roughly proportional to the charge delivered to the target. Figure 7-7 shows the residual activation history near the stripper foil after production runs (taken at 30 cm, generally 1-2 days following production). The activation levels approaching ~500 mrem/hr are consistent with expectations from the roughly 10-4 fractional beam loss due to foil scattering in the vicinity of the foil. The beam loss and activation levels in the collimation and extraction regions are much lower (typically 20-50 mrem/hr). The rest (majority) of the ring has very small beam loss and residual activation.

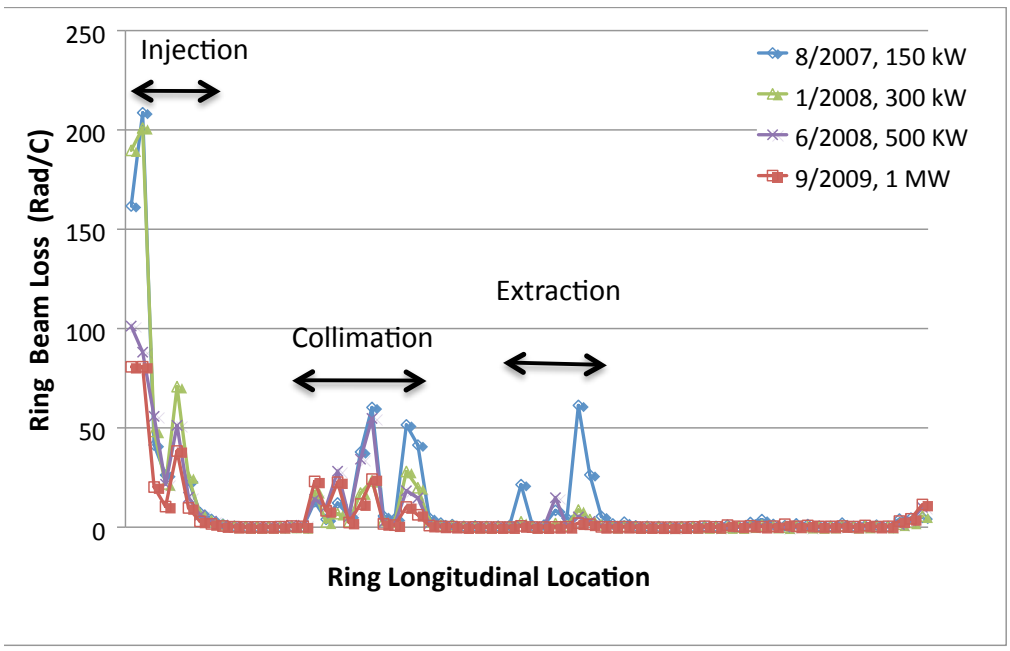

Figure 7-6. Reduction of the normalized beam loss (loss per pulse divided by the charge per pulse), over the power rampup period, around the entire SNS ring.

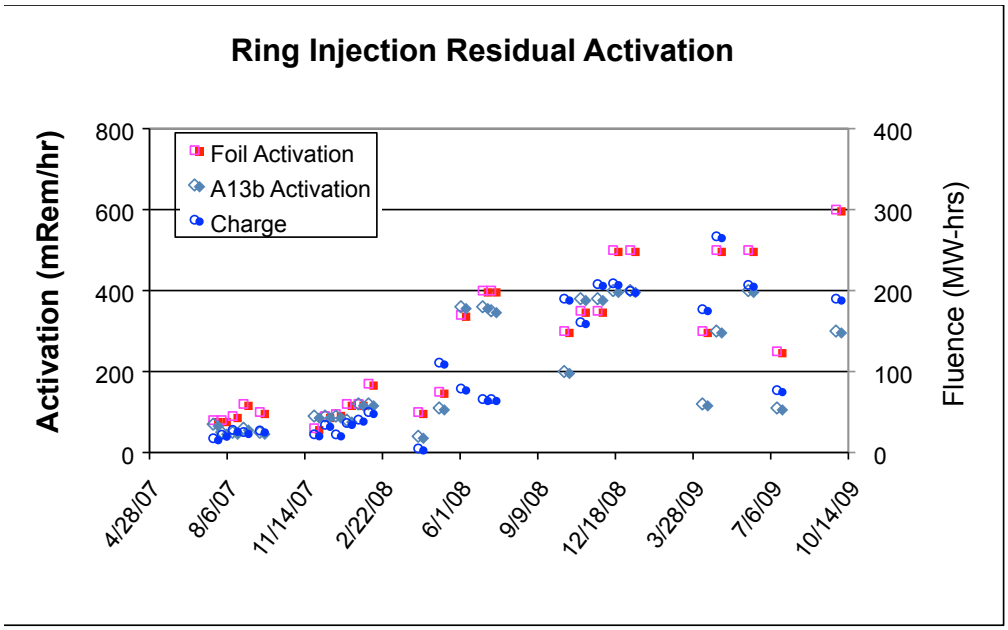

Figure 7-7. Buildup of residual activation levels in the ring injection area over the initial operation (foil and A13b locations). Also shown is the charge delivered to the target during each run preceding the activation measurement.

7.2.4 Transport Line Beam Loss

Beam, loss and activation along the HEBT and RTBT transport lines is minimal. Most of the transport line has residual activation levels < 5 mrem/hr at 30 cm one day after shutdown from extended production runs of ~1 MW beam powers. There are some hot spots of ~ 10-50 mrem/hr at the transition from the SCL doublet to the HEBT FODO lattice and in the vicinity of the HEBT collimation. In the RTBT there is a local hot spot at an aperture limitation entering a bend, arising from beam in the gap which is only partially kicked during extraction. A second location at the very end of the RTBT, exhibits high beam loss due to the expansion of the beam size for the target, and also where the seven wire planes of the harp are continuously in the path of the beam (we plan to install a harp insertion mechanism in the future). None of these beam loss levels approach that of the ring injection area, and do not pose a limitation to the operational beam power.

8. FUTURE PLANS

The SNS accelerator baseline design power was 1.4 MW, and to date routine 1 MW operation has been achieved. The major design and operational parameters are shown in Table 8-1. Raising the operational beam power to the design level of 1.4 MW requires increasing the pulse length to 1 ms, increasing the beam energy to 1.0 GeV and increasing the average current to 26 mA. The present pulse length limitation is due to concerns over the RF high voltage convertor modulator (HVCM) system reliability, and HVCM component improvements have alleviated these issues [60]. The average beam current will be increased with chopper protection system improvements that decrease the rise/fall times (see Section 2.4). Increasing the beam energy to the nominal 1 GeV requires improving some of the SCL high beta cavity operational gradients, for which a plasma processing technique is being developed [65]. Finally, concerns about the mercury target vessel lifetime have limited beam power, but mercury flow

path changes are being implemented to alleviate vessel erosion issues [66,67]. These changes and beam power increase to the design of ~ 1.4 MW are planned for the next ~5 years.

The SNS accelerator was designed to accommodate an increase in beam power above 1.4 MW. For example the SCL tunnel has room for additional cryomodules, much of the present RF system can accommodate increased beam loading, most of the transport line and ring magnets and power supplies can accommodate a beam energy up to 1.3 GeV. Planning for a Power Upgrade Project (PUP) was initiated in 2005 [68]. The power upgrades involve accommodations for increased beam energy to 1.3 GeV and increased beam current by ~50% (see Table 8-1).

Upgrade activities supporting the increased beam energy include installation of 9 new cryomodules at the end of the superconducting linac, supporting RF systems for the new cryomodules, replacing two of the ring injection chicane magnets and one septum magnet in the injection dump line, and adding two additional ring extraction kickers. The beam current increase requires improved ion source capability, and increase linac RF power capability to handle the increased beam loading. The present warm linac RF systems are capable of handling the increased beam loading, however the SCL RF systems will require upgrades. In particular the peak power capability for the klystrons will need to be increased from 550 to 700 kW (to this end the spare klystrons presently being purchased are capable of 700 kW operation). Also the SCL high voltage convertor modulator systems (HVCM) require development to support the increased beam loading. In addition to the increased source current capability, a dual source configuration is planned to offer improved system reliability. A "Y" configuration with two sources and a magnetic LEBT that funnel into the RFQ is planned for this purpose. Only one source would run at a time, the other being a hot spare.

The present neutron-producing target is designed for beam powers up to 2 MW, less than the upgraded beam power of 3 MW beam power discussed above. The additional 1 MW of beam power is envisioned to go to a Second Target Station (STS) [69]. The STS will receive 20 Hz pulses and the original target will receive the remaining 40 Hz. The STS is planned to be a "long pulse " neutron source, which can accept a 1 ms long proton beam – obviating the need to compress the linac beam to 1 ms in the storage ring for these pulses. Both the accelerator upgrades discussed above the additional target station are now being considered as a single project.

Table 8-1 Major device parameters for the design, actual MW operation and the power upgrade plans.

	Design	**1 MW Operation**	**Power Upgrade**
Beam Power (MW)	1.44	1.0	3.0
Beam energy (GeV)	1.0	0.925	1.3
Peak Ion Source Current (mA)	38	38	60
Average macropulse current (mA)	26	24	40
Macropulse length (ms)	1.0	0.79	1.0
Repetition rate (Hz)	60	60	60
Medium beta cavity E_{acc} (MV/m)	10.2	11.9	11.9
High beta cavity E_{acc} (MV/m)	15.6	12.8	13.7
Medium beta cavities	33	32	33
High beta Cavities	48	48	84
Klystron Peak power (kW)	550	550	700

REFERENCES

1. S. Henderson, et al., "The Spallation Neutron Source Accelerator System Design", Nuclear Instruments and Methods-A, 763 (2014) 610-673.
2. R. Keller et. al., "Commissioning of the SNS Front End Systems at Berkeley Lab". *Proceedings of EPAC 2002*, Paris, France, http://accelconf.web.cern.ch/AccelConf/e02/PAPERS/THPLE012.pdf .
3. A. Ratti et. al., "The SNS RFQ Commissioning", *Proceedings of LINAC 2002*, Gyeongju, Korea, http://accelconf.web.cern.ch/AccelConf/l02/PAPERS/TU412.PDF
4. A. Aleksandrov, "Commissioning of the SNS Front End Systems", *Proceedings of the 2003 Particle Accelerator Conference*, p. 65-67, http://accelconf.web.cern.ch/AccelConf/p03/PAPERS/MOPB002.PDF
5. R. Keller, et al., "Design, Operational Experiences and Beam Results Obtained with the SNS H- Ion Source and LEBT at Berkeley Lab" in *Production and Neutralization of Negative Ions and Beams*, edited by M. P. Stockli, *AIP Conference Proceedings CP639*, American Institute of Physics, Melville, N.Y., 2002, pp.47-60.
6. R.F. Welton, et al, "H^- Radio Frequency Source Development at the SNS", Rev. Sci. Instruments, 83, (02A725-1) 2012
7. M. P. Stockli, et. al, "Ramping Up the the SNS Beam Power with the LBNL Baseline H^- Source", *AIP Conference Proceedings 1097*, American Institute of Physics, Melville, N.Y., 2009, pp.223-235.
8. B. Han, D. Newland, W. Hunter, M. Stockli, "Physics Design of a Prototype 2-Solenoid LEBT for the SNS Injector", *Proceedings of the 2011 Particle Accelerator Conference*, New York, NY, p. 1564-1566, http://accelconf.web.cern.ch/AccelConf/PAC2011/papers/wep038.pdf
9. A. Ratti et al., "The design of a high current, high duty fac- tor RFQ for the SNS," *Proc. European Particle Accelerator Conference*, Vienna, Austria, June 2000, 495-497.
10. K. Crandall, T. Wangler, "PARMTEQ: A Beam Dynamics Code for the RFQ", LANL Report LA-UR-88-1546 CONF-8701132-1.
11. J. Staples et., al., "Design of the SNS MEBT", *Proceedings of the 2000 Linac Conference*, Monterey, California, 2000, p. 250-252, http://accelconf.web.cern.ch/AccelConf/l00/papers/MOD18.pdf
12. A. Aleksandrov, et. al., " SNS Warm Linac Commissioning", *Proceedings of EPAC 2006*, Edinburgh, Scotland, p. 342-344, Proceedings of EPAC 2006, Edinburgh, Scotland . p. 342-344, http://accelconf.web.cern.ch/AccelConf/e06/PAPERS/MOPCH127.PDF
13. H. Takeda, J. Billen, "Recent Improvements in the PARMILA Code", *Proceedings of the 2003 Particle Accelerator Conference*, p. 3218-3220, http://epaper.kek.jp/p03/PAPERS/FPAG028.PDF
14. D. Bartoski, et al., "High Dynamic Range Current Measurements in the MEBT at the SNS", Proceedings of LINAC 2006, Knoxville, Tennessee USA, p. 244-246, http://accelconf.web.cern.ch/AccelConf/l06/PAPERS/TUP002.PDF
15. A. Aleksandrov, C. Deibele, "Experimental Study of the SNS MEBT Chopper Performance", *Proceedings of the 2010 International Particle Accelerator Conference*, p. 831-833, http://accelconf.web.cern.ch/AccelConf/IPAC10/papers/mopd063.pdf
16. S. Henderson, et. al., " SNS Beam Commissioning Status", *Proceedings of the 2004 European Particle Accelerator Conference*, Lucerne, Switzerland, http://accelconf.web.cern.ch/AccelConf/e04/PAPERS/TUPLT168.PDF
17. A, Akeksandrov, "Results of the Initial Operation of the SNS Front End and Drift Tube Linac", *Proceedings of LINAC 2004*, Lübeck, Germany, http://accelconf.web.cern.ch/AccelConf/l04/PAPERS/WE201.PDF
18. A. Aleksandrov, "SNS Warm Linac Commissioning Results", *Proceedings of 2005 Particle Accelerator Conference*, Knoxville, Tennessee p. 97-101, http://accelconf.web.cern.ch/AccelConf/p05/PAPERS/ROPC001.PDF

19. A. Aleksandrov, et al, " Performance of the SNS Front End and Warm Linac", *Proceedings of LINAC 2006*, Knoxville, Tennessee, p. 145-147, http://accelconf.web.cern.ch/AccelConf/l06/PAPERS/MOP045.PDF
20. K. R. Crandall, "The Delta-t Tuneup Procedure for the LAMPF 805-MHz Linac",LA-6374-MS (UC-28) (May 1976).
21. A. Feschenko, S. Bragin, Yu. Kiselev, L. Kravchuk, O. Volodkevich, A. Aleksandrov, J. Galambos, S. Henderson, A. Shishlo, "Development and Implementation of a D-T Procedure for the SNS Linac", *Proceedings of 2005 Particle Accelerator Conference*, Knoxville, Tennessee p. 3065-3067.
22. T.L. Owens, M. B. Popovic, E. S. McCrory, C. W. Schmidt, L.J. Allen, "Phase Scan Signature Matching for Linac Tuning", Particle Accelerators, 1994, **98**, p. 169.
23. J. Galambos, A. Aleksandrov, C. Deibele, S. Henderson, Spallation Neutron Source, "PASTA – An RF Phase Scan and Tuning Application", *Proceedings of the 2005 Particle Accelerator Conference*, Knoxville TN, 2005, http://accelconf.web.cern.ch/AccelConf/p05/PAPERS/FPAT016.PDF .
24. J. Power et. al., "SNS Beam Position and Phase Monitoring System", *Proceedings of LINAC 2006*, Knoxville, Tennessee USA, p. 247-249, http://accelconf.web.cern.ch/AccelConf/l06/PAPERS/TUP003.PDF
25. D. Jeon, J. Stovall, K. Crandall, "Longitudinal Tuneup of SNS Normal Conducting Linac", *Proceedings of LINAC 2002*, Gyeongju, Korea, p. 368-370, http://accelconf.web.cern.ch/AccelConf/l02/PAPERS/TU427.PDF
26. D. Jeon *et al*, Acceptance Scan Technique for the Drift Tube Linac of the Spallation Neutron Source, Nucl. Instr. and Meth. A 570 (2007) 187.
27. A. Shishlo, A. Aleksandrov, " Model Based Orbit Correction in a Diagnostic Deficient Region", *Proceedings of EPAC 2008*, Genoa, Italy, p. 3056-3058, http://accelconf.web.cern.ch/AccelConf/e08/papers/thpc036.pdf
28. A. Aleksandrov, et. al., " Beam Dynamics Studies and Beam Quality in the SNS Normal Conducting Linac", *Proceedings of EPAC 2006*, Edinburgh, Scotland , p. 3381-3383, http://accelconf.web.cern.ch/AccelConf/p05/PAPERS/FPAE057.PDF
29. I. E. Campisi, "Testing of the SNS Superconducting cavities and cryomodules," *Proceedings of Particle Accelerator Conference 2005*, pp. 34-38, Knoxville, TN, 16-20, May (2005)
30. D. Stout, et. al, "Installation of the Spallation Neutron Source (SNS) Superconducting Linac," *Proceedings of Particle Accelerator Conference 2005*, pp. 3838-3840, Knoxville, TN, 16-20, May (2005)
31. S. Henderson, " Commissioning and Initial Operating Experience with the SNS 1 GeV Linac", *Proceedings of LINAC 2006*, Knoxville, Tennessee USA, p. 1-5, http://accelconf.web.cern.ch/AccelConf/l06/PAPERS/MO1002.PDF
32. S.Kim and I.E.Campisi, "Thermal stabilities and optimal operating parameters for the Oak Ridge Spallation Neutron Source superconducting linear accelerator," PRST-AB, **10**, 032001, March 2007
33. S. Kim and I.E.Campisi, "Commissioning of the Superconducting Linac at the Spallation Neutron Source (SNS)," *Proceedings of the IEEE Trans. Applied Superconductivity*, Vol. 17, No. 2, pp. 1299-1304, June 2007
34. S. Kim, "SNS Superconducting Linac Operational Experience and Upgrade Path," *Proceedings of 24th International LINAC conference* 2008, pp. 11-15, Victoria, Canada, 29 September-3 October, 2008.
35. S. Henderson, et al, " SNS Superconducting Linac Commissioning Algorithms", *Proceedings of 2005 Particle Accelerator Conference*, Knoxville, Tennessee, p. 3423-3425, http://accelconf.web.cern.ch/AccelConf/p05/PAPERS/FPAE058.PDF
36. J. Galambos, A. Aleksandrov, C.K. Allen, S. Henderson, A. Shishlo, T. Pelaia, Y. Zhang, C. P. Chu, "Software Tools for Commissioning of the SNS Linac", *Proceedings of 2007 Particle Accelerator Conference*, Albuquerque, New Mexico, USA http://accelconf.web.cern.ch/AccelConf/p07/PAPERS/TUOCC01.PDF .

37. J. Galambos et al, " A Fault Recovery System for the SNS Superconducting Cavity Linac", *Proceedings of LINAC 2006 Conference*, Knoxville, Tennessee USA, p. 174-176, http://accelconf.web.cern.ch/AccelConf/l06/PAPERS/MOP057.PDF
38. J. Galambos, S. Henderson, A. Shishlo, Y. Zhang, "Operational Experience of a Superconducting Fault Recovery System at the Spallation Neutron Source", *Proceedings of the Fifth International Workshop on the Utilisation and Reliability of High Power Proton Accelerators*, Mol Belgium, May 2007.
39. Y. Zhang et. al., Nucl. Inst. Meth. A 571 (2007) 574
40. Y. Liu, et al, Nuclear Instruments and Methods in Physics Research A 612 (2010) 241–253
41. C.K. Allen, LANL, Los Alamos, NM 87545, U.S.A. K. Furukawa, M. Ikegami, " Adaptive Three-Dimensional RMS Envelope Simulation in the SAD Accelerator Modeling Environment", *Proceedings of LINAC 2006*, Knoxville, Tennessee USA, p. 397-399, http://accelconf.web.cern.ch/AccelConf/l06/PAPERS/TUP064.PDF
42. Jeon and P. Chu, *Proc. of 2007 Asian Part. Accl. Conf.*, p. 250, Indore, India http://accelconf.web.cern.ch/AccelConf/a07/PAPERS/TUPMA105.PDF.
43. Dong-O Jeon, C. Chu, V. Danilov, "Transverse Matching Techniques for the SNS Linac*",* *Proceedings of 2005 Particle Accelerator Conference*, Knoxville, Tennessee, http://accelconf.web.cern.ch/AccelConf/p05/PAPERS/FPAE059.PDF
44. T. Pelaia and P. Chu, "Beam Trajectory Correction for SNS," *Proceedings of the 2005 Particle Accelerator Conference*, Knoxville, TN, May 16-20, 2005, p. 1425.
45. M. Plum et al., *Proceedings of the 2006 European Particle Accelerator Conference*, Edinburgh, Scotland, June 26-30, 2006.
46. S. Thorson, "Model Independent Analysis of Beam Position Monitor Data in the Spallation Neutron Source," SNS Tech Note 0169, 2006. Also S. Cousineau, private communication, 2006.
47. M. Plum, "Commissioning of the Spallation Neutron Source Accelerator Systems," *Proceedings of the 2007 Particle Accelerator Conference*, Albuquerque, June 25-29, 2007, p. 2603.
48. D. Sagan et al., "Betatron phase and coupling measurements at the Cornell Electron/Position Storage Ring," Physical Review Special Topics-AB, **3**, 0928901 (2000).
49. M. Plum, "SNS Injection and Extraction Systems Issues and Solutions," *Proceedings of the HB2008*, Nashville, TN, Aug. 24-29, 2008.
50. R. Shaw et al., "Diamond Stripper Foil Experience at SNS and PSR," *Proceedings of EPAC 2008,* Genova, Italy, June 20-25, 2008, p. 3563.
51. M. Plum et al., "SNS Stripper Foil Failure Modes And Their Cures," *Proceedings of the 2010 International Particle Accelerator Conference*, Kyoto, Japan, May 23-28, 2010.
52. T. Pelaia and S. Cousineau, "A method for probing machine optics by constructing transverse real space beam distributions using Beam Position Monitors," Nucl. Inst. & Meth. A596, 295 (2008).
53. J.G. Wang, "3D Field Quality Studies of SNS Ring Extraction Lambertson Septum Magnet," *Proceedings of the 2009 Particle Accelerator Conference*, Vancouver, CA, May 3-8, 2009.
54. T. Hardek et al., "The Spallation Neutron Source Accumulator Ring RF System," *Proceedings of the 2007 Particle Accelerator Conference*, Albuquerque, June 25-29, 2007, p. 3795.
55. S. Cousineau, "Experimental Characterization of the Spallation Neutron Source Accumulator Ring Collimation System," *Proceedings of the 2007 Particle Accelerator Conference*, Albuquerque, June 25-29, 2007, p. 703.
56. V.V. Danilov et al., "Accumulation of High Intensity Beam and First Observations of Instabilities in the SNS Accumulator Ring," *Proceedings of the 2006 ICFA HB Workshop*, Tsukuba, Japan, May-June 2006.
57. S. Cousineau et al., "Experimental Observations and Simulations of Electron-Proton Instabilities in the Spallation Neutron Source Ring," *Proceedings of the 2007 ICFA E-Cloud Workshop*, Daegu Korea (2007).
58. M. Plum et al., "Performance of and Upgrades to the SNS Collimator Systems," *Proceedings of the 2009 Particle Accelerator Conference*, Vancouver, CA, May 3-8, 2009.

59. T. McManamy, C. Goetz, and T. Shea, "SNS Target Beam Profile Viewscreen Design And Operation," *Proceedings of the 2007 Accelerator Application Conference*, Pocatello, ID, 2006.
60. R. Cutler, et. al., "Oak Ridge National Laboratory Spallation Neutron Source Electrical Systems Availability and Improvements", *Proceedings of the 2011 Particle Accelerator Conference*, NY, NY., March 2011., http://www.c-ad.bnl.gov/pac2011/proceedings/papers/tup274.pdf
61. J. Galambos, "Spallation Neutron Source Operational Experience at 1 MW", *Proceedings of the 2010 ICFA HB Workshop*, Morshach Switzerland, 2010, http://accelconf.web.cern.ch/AccelConf/HB2010/papers/tuo2c01.pdf
62. J. Galambos, "The SNS Power Rampup", *Proceedings of the 2008 ICFA HB Workshop*, Nashville TN, 2008, http://accelconf.web.cern.ch/AccelConf/HB2008/papers/wgd03.pdf
63. A. Zhukov, et al., "SNS BLM System Evolution: Detectors, Electrons, Software", *Proceedings of the 2009 Particle Accelerator Conference*, Vancouver, BC, Canada, p. 4853-4855, http://accelconf.web.cern.ch/AccelConf/PAC2009/papers/fr5rep038.pdf
64. J. Galambos, "Progress With MW-Class Operation of the Spallation Neutron Source," *Proceedings of the 2009 Particle Accelerator Conference*, Vancouver, CA, May 3-8, 2009.
65. S-H. Kim, et al., " R&D Status for in situ Plasma Surface Cleaning of SRF Cavities at SNS", *Proceedings of 2011 Particle Accelerator Conference*, New York, NY, USA, http://www.c-ad.bnl.gov/pac2011/proceedings/papers/thocs3.pdf .
66. T.J. McManamy, et.al., "Overview of the SNS target system testing and initial beam operation experience", Journal of Nuclear Materials, Vol. 377, p. 1, Elsevier (2008)
67. T.J. McManamy, "SNS Target Systems Operating Experience at 1 MW", AccApp11, Knoxville, Tn., April, 2011,to be published.
68. S. Henderson, et. al., "Status of the SNS Beam Power Upgrade Project", *Proceedings of EPAC 2006*, Edinburgh, Scotland , p. 345-347, http://accelconf.web.cern.ch/AccelConf/e06/PAPERS/MOPCH129.PDF
69. R. K. Crawford, R. Dean, P. Ferguson, J. Galambos, F. X. Gallmeier, T. McManamy, M. Rennich, "The Second Target Station at the Spallation Neutron Source", International Conference on Neutron Scattering 2009, Journal of Physics: Conference Series, 251, 012054 (2010).